The chromitites of the Herbeira massif (Cabo Ortegal Complex, Spain) revisited

Matías García-Tudela [a],[*], Joaquín A. Proenza [b], Júlia Farré-de-Pablo [b], Núria Pujol-Solà [c], Thomas Aiglsperger [a], Montgarri Castillo-Oliver [b], Vanessa Colás [d], Ricardo Arenas [e], Antonio Garcia-Casco [c],[f]

[a] Department of Civil Engineering and Natural Resources, Luleå University of Technology, SE 97187, Luleå, Sweden
[b] Departament de Mineralogia, Petrologia i Geologia Aplicada, Facultat de Ciències de la Terra, Universitat de Barcelona, Carrer Martí i Franquès, s/n, 08028 Barcelona, Spain
[c] Departamento de Mineralogía y Petrología, Facultad de Ciencias, Universidad de Granada, Avda. Fuentenueva, s/n, 18071 Granada, Spain
[d] IUCA-Departamento de Ciencias de La Tierra, Universidad de Zaragoza, Pedro Cerbuna 12, 50009 Zaragoza, Spain
[e] Departamento de Mineralogía y Petrología and Instituto de Geociencias (UCM, CSIC), Universidad Complutense, Madrid, Spain
[f] Instituto Andaluz de Ciencias de la Tierra (CSIC-UGR), Avda. de las Palmeras 4, E-18100 Armilla, Granada, Spain

ARTICLE INFO

ABSTRACT

The ultramafic rocks of the Herbeira Massif in the Cabo Ortegal Complex (NW Iberia) host chromitite bodies. The textural and compositional study of the host rocks and the chromitites classified them into: (1) Type-I chromitites, forming massive pods of intermediate-Cr chromite (Cr# = 0.60–0.66) within dunites; and (2) Type-II chromitites forming semi-massive horizons of high-Cr chromite (Cr# = 0.75–0.82) interlayered with dunites and pyroxenites. Minor and trace elements (Ga, Ti, Ni, Zn, Co, Mn, V and Sc) contents in the unaltered chromite cores from both types show patterns very similar to fore-arc chromitites, mimicked by the host dunites and pyroxenites. Calculated parental melt compositions suggest that Type-I chromitites crystallized from a melt akin to fore-arc basalt (FAB), while Type-II chromitites originated from a boninite-like parental melt. Both melts are characteristic of a fore-arc setting affected by extension during rollback subduction and have been related to the development of a Cambrian-Ordovician arc. These chromitites are extremely enriched in platinum-group elements (PGE), with bulk-rock PGE contents between 2,460 and 3,600 ppb. Also, the host dunites and pyroxenites exhibit high PGE contents (167 and 324 ppb, respectively), which are higher than those from the primitive mantle and global ophiolitic mantle peridotites. The PGE enrichment is expressed in positively-sloped chondrite-normalized PGE patterns, characterized by an enrichment in Pd-group PGE (PPGE: Rh, Pt and Pd) over the Ir-group PGE (IPGE: Os, Ir and Ru) and abundant platinum-group minerals (PGM) dominated by Rh-Pt-Pd phases (i.e. Rh-Ir-Pt-bearing arsenides and sulfarsenides, Pt-Ir-Pd-base-metal-bearing alloys, and Pt-Pd-bearing sulfides). The PGM assemblage is associated with base-metal sulfides (mostly pentlandite and chalcopyrite) and occurs at the edges of chromite or embedded within the interstitial (serpentinized) silicate groundmass. Their origin has been linked to direct crystallization from a S-As-rich melt(s), segregated by immiscibility from evolved volatile-rich small volume melts during subduction. At c. 380 Ma, retrograde amphibolite-facies metamorphism occurred during the exhumation of the HP-HT rocks of the Capelada Unit, which affected chromitites and their host rocks but preserved the primary composition of chromite cores of the chromitites. This event contributed to local remobilization of PGE as suggested by the negative slope between Pt and Pd and high Pt/Pd ratios in the studied chromitites, and host dunites and pyroxenites. In addition, it promoted the alteration of primary PGM assemblage and the formation of secondary PGM. Nanoscale observations made by focused ion beam high-resolution transmission electron microscopy (FIB/HRTEM) analysis of a composite grain of Rh-bearing arsenide with PGE-base-metal bearing alloys suggest the mobilization and accumulation of small nanoparticles of PGE and base-metals that precipitated from metamorphic fluids forming PGE-alloys. Finally, we offer a comparison of the Cabo Ortegal chromitites with other ophiolitic chromitites involved in the Variscan orogeny, from

the Iberian Peninsula to the Polish Sudetes. The studied Cabo Ortegal chromitites are similar to the Variscan chromitites documented in the Bragança (northern Portugal) and Kraubath (Styria, Austria) ophiolitic massifs.

1. Introduction

The ultramafic rocks of the Herbeira massif of the Cabo Ortegal Complex (NW Iberia), host high-Cr chromitite (Cr# ≥ 0.6) bodies with anomalously high platinum-group elements (PGE: Os, Ir, Ru, Rh, Pt, and Pd) contents reaching up to 13,000 ppb, characterized by enrichment in Pd-group PGE (PPGE: Rh, Pt, and Pd) over Ir-group PGE (IPGE: Os, Ir, and Ru) (Moreno et al., 1999). The PGE contents in the Cabo Ortegal chromitites are clearly higher than typical values in high-Cr ophiolitic

chromitites (<1,000 ppb; Leblanc, 1991; Gervilla et al., 2005), but similar to ophiolitic chromitites containing interstitial sulfides (i.e. Type II chromitites in González-Jiménez et al., 2014b). These concentrations characterize the top of the 800 m thick so-called Herbeira Layered Complex, composed of two dunite-dominated units separated by a garnet-bearing pyroxenite-dominated unit, all above the associated Herbeira high-Al spinel mantle harzburgite (Moreno et al., 2001). These authors interpreted the Herbeira Layered Complex as a mafic–ultramafic cumulate sequence (above the Moho) representing a magmatic arc-root,
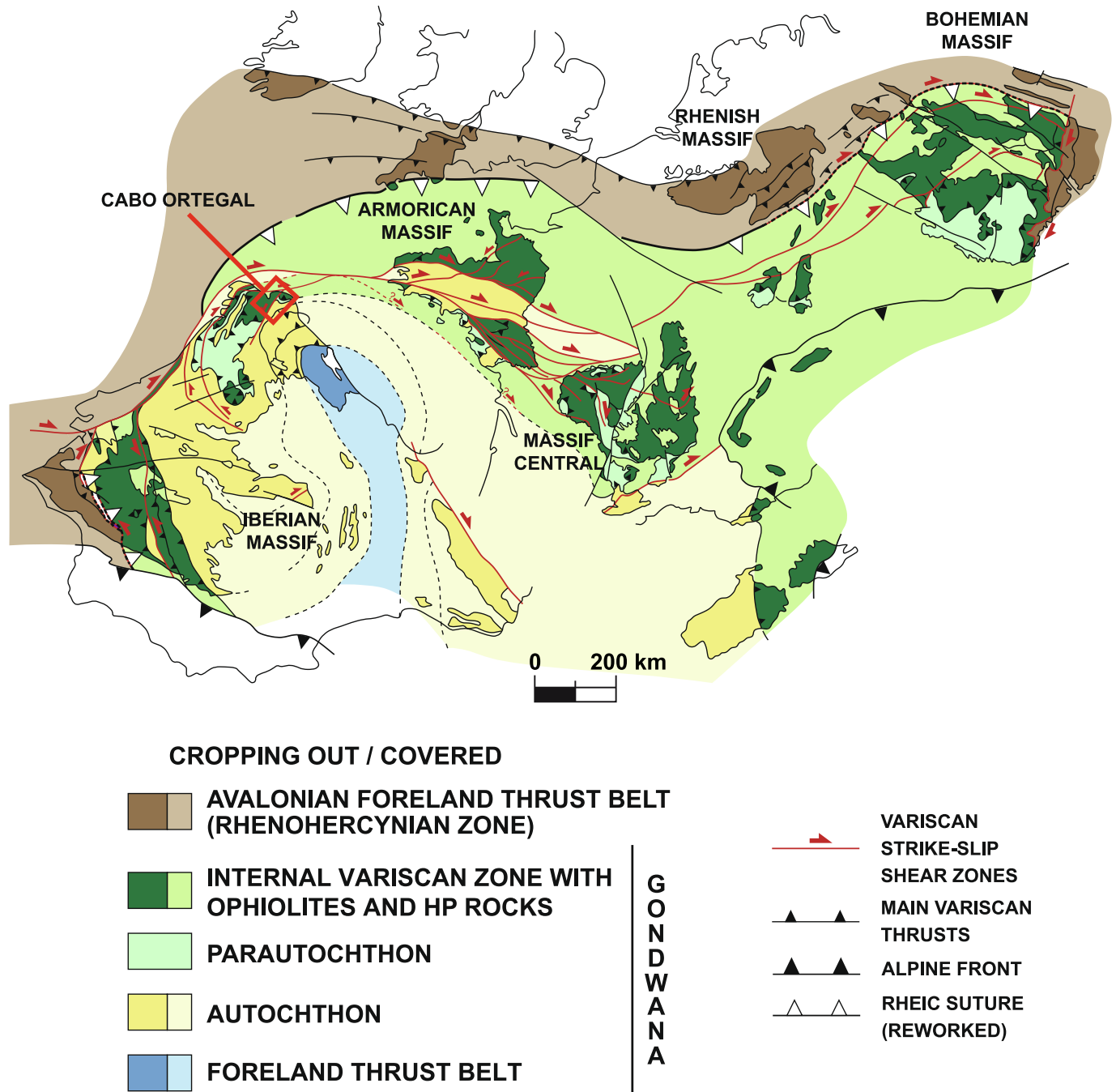

Fig. 1. Domains of the Variscan Orogen. After Díez Fernández and Arenas (2015); based in Franke (1989), Lefort (1989), Neuman and Max (1989) and Martínez Catalán (2011). The red square shows the location of the Cabo Ortegal Complex.
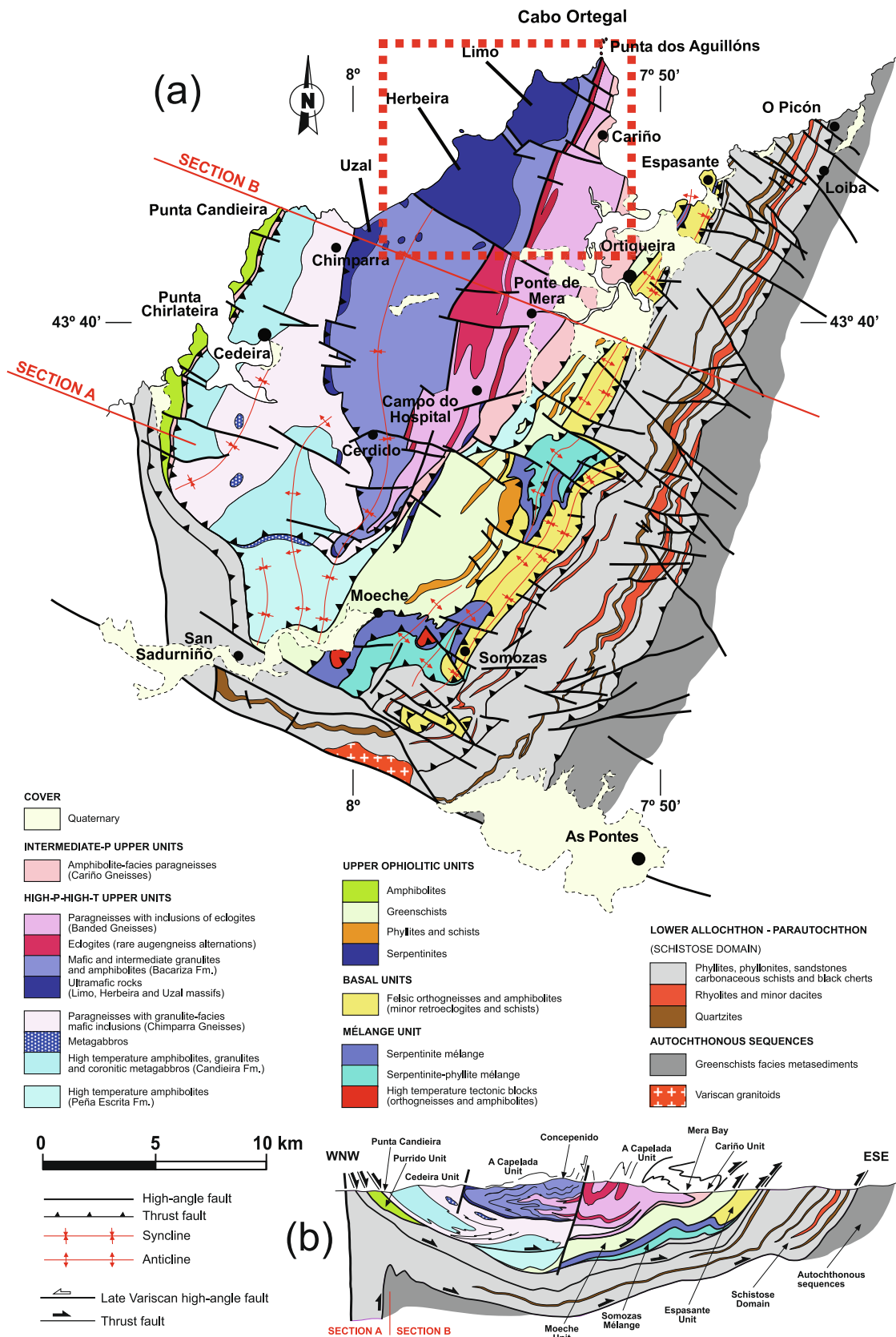
Fig. 2. A) geological map and b) composite cross section of the cabo ortegal complex. afterArenas et al. (2016); based in Vogel (1967), Marcos et al. (1984), Arenas (1988) and Arenas et al. (2014). The red square shows the location of Fig. 3.
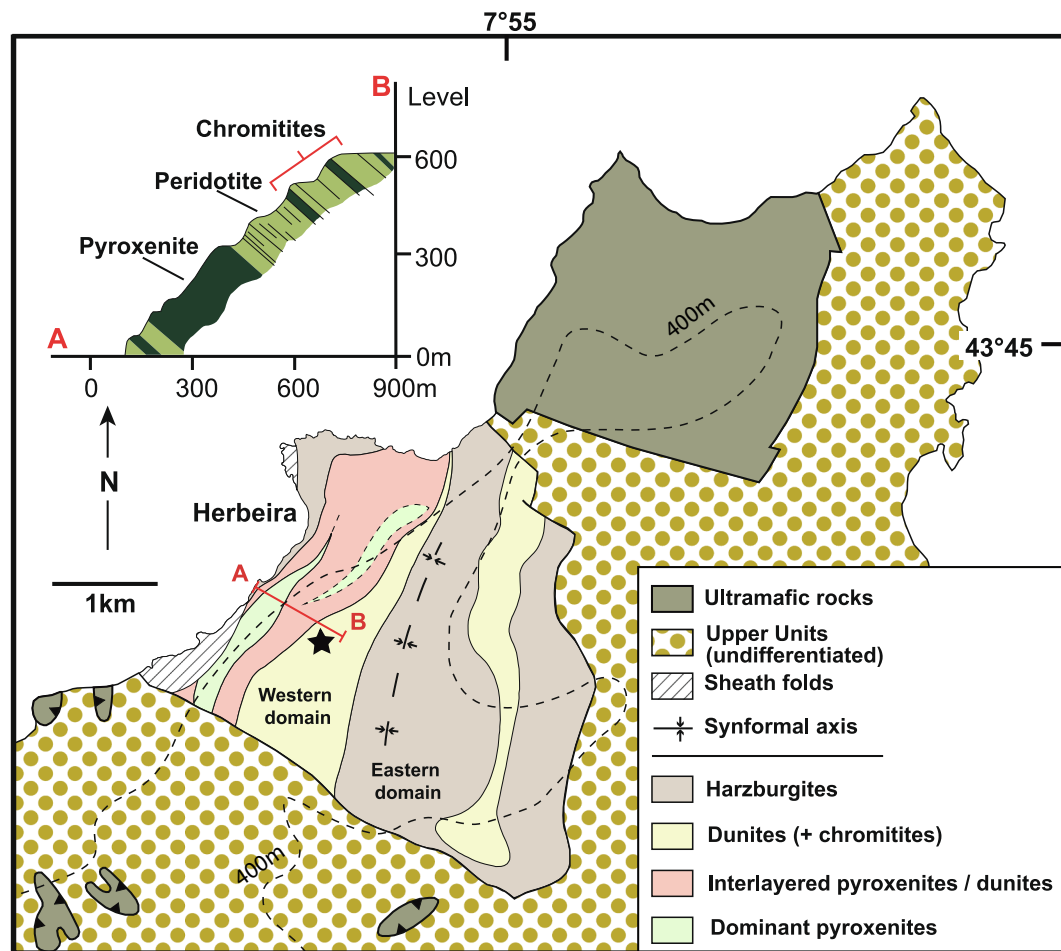
Fig. 3. Geological map of the Herbeira massif showing the main geological units and the location of the studied chromitites. The black star indicates the sampling location. Modified from Sánchez Martínez et al. (2007), Arenas et al. (2016), and Tilhac et al. (2020).

where high-Cr and PGE-rich chromitites formed during successive injections of mantle-derived Cr- and PGE-rich magmas. However, recent research reinterpreted the sequence as a part of the mantle, where the interaction between melts and a refractory harzburgite in a sub-arc mantle environment formed dunites, pyroxenites and chromitites (Tilhac et al., 2016). Therefore, the origin of these chromitites, together with their PGE enrichment, remains unclear. Despite that previous works focused on the geochemistry and petrology of the chromitites and their host rocks (mainly dunites and pyroxenites) many questions remain about the mineralogical setting of PGE on these chromitites. Previous studies on platinum-group minerals (PGM) of the Cabo Ortegal chromitites were carried out more than 20 years ago (Moreno et al., 1999), reporting only a few Os-Ir-Ru-rich PGM and great abundance of Pt-Pd-Rh-rich PGM (i.e. more than 200 grains of PGM within 20 samples), including sulfides [braggite (PdPt$_3$S$_4$)-cooperite (PtS)], alloys (Pt-Rh-base metals), complex amalgams (Pt-Pd-Au-Hg-Pb), sulfarsenides [hollingworthite (RhAsS)-platarsite (PtAsS); recently disaccredited as variety of S-rich sperrylite (McDonald and Cabri, 2023) −irarsite (IrAsS)], arsenides [sperrylite (PtAs$_2$)], bismuthides (Pd-Pt-Bi), tellurides (Pd-Te-Bi), and oxides (Pt-Pd-O). Most of these PGM were found associated with Ni-Fe-Cu sulfides sealed in chromite crystals or more frequently at the margin of the interstitial silicate matrix between those crystals. Moreno et al. (1999) interpreted that PGM located on the edges of chromite (Pt-Pd sulfides) formed by exsolution from primary PGM or PGE-rich sulfides. On the other hand, PGM (PGE-alloys, arsenides, bismuthides, and tellurides) included in the interstitial silicate matrix transformed to serpentine minerals were interpreted as related to post-magmatic processes.

In this paper, we present and discuss new petrographic, mineralogical, and geochemical data from the chromitites of the Herbeira massif, in view of a different interpretation of data suggesting a mantle origin and post-magmatic evolution of these chromitites. We specifically targeted those chromitites hosted in dunites from the upper part of the pseudostratigraphy of the Herbeira massif and we provide the first-ever minor and trace elements data for chromite forming these chromitites, as well as a detailed review about the genesis of the PGM in these chromitites anomalously enriched in PGE. We also present the first nanoscale study of PGM from these chromitites combined with observations of PGM in situ and from hydroseparation concentrates.

2. Geological setting

2.1. The Cabo Ortegal Complex

The Cabo Ortegal Complex, located in north-western Spain (Fig. 1), is part of the Iberian section of the Variscan Orogen. The Allochthonous Complexes (Cabo Ortegal, Órdenes, Malpica-Tui, Bragança, and Morais) were tectonically emplaced above the *para*-autochthonous and the autochthonous of the Central Iberian Zone during the Variscan orogeny (Martínez Catalán et al., 2007, 2021; Díez Fernández et al., 2016, 2020). These Allochthonous Complexes comprise different lithological units of metamorphic rocks (Upper and Basal Units) that record Devonian-Carboniferous subduction-collision of *peri*-Gondwanan terranes, including extinct Neoproterozoic-Cambrian-Ordovician volcanic arc-related units (Martínez Catalán et al., 2019; Novo-Fernández et al., 2022; Beranoaguirre et al., 2022 and references therein). In these
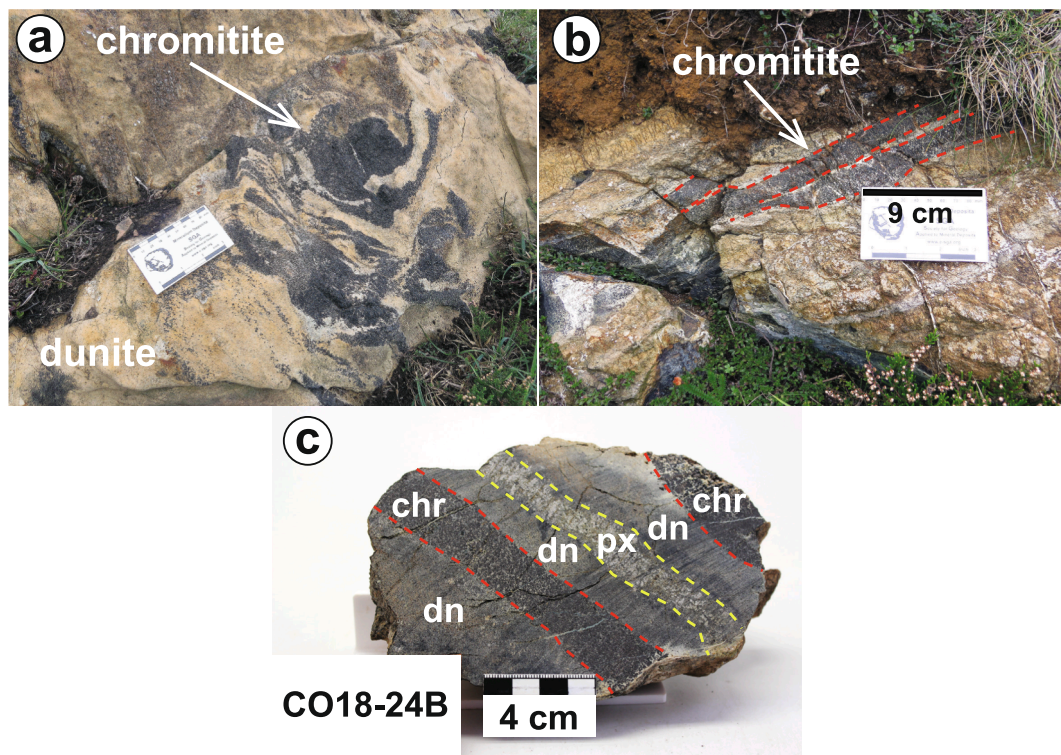
Fig. 4. Field images of the Cabo Ortegal chromitites. a) Massive podiform chromitites (Type-I chromitites). b) Semi-massive chromitites horizons (Type-II chromitites). c) Hand sample of a chromitite horizon (chr) showing the distribution between dunites (dn) and pyroxenites (px).

Allochthonous Complexes, there are also Cambrian and Devonian suprasubduction zone ophiolites in an intermediate tectonic position between the Upper and Basal Units, which were obducted during the closure of *peri*-Gondwanan oceanic basins (Arenas et al., 2016 and references therein).

The Cabo Ortegal Complex consists of a suite of units that include, from top to bottom (Arenas et al., 2016 and references therein): Upper Units, Ophiolitic Units, Basal Units, and the Somozas Mélange (Fig. 2). The Upper Units are comprised of rocks affected by intermediate-pressure (IP) and high-pressure–high-temperature (HP-HT) metamorphism (Arenas et al., 2016). The IP metamorphic rocks, represented by the Cariño Unit, occupy a dominant normal position above the HP-HT Capelada Unit, and are affected by a train of recumbent folds developed during the exhumation of the HP-HT subduction complex (Albert et al., 2013). The Cariño Unit contains a sequence of amphibolite facies turbiditic pelitic to greywackic paragneisses with a maximum depositional age of c. 510 Ma, interlayered with acidic and basic *meta*-igneous rocks (Albert et al., 2015). The HP-HT metamorphic rocks of the Upper Units occur in the Capelada (above) and Cedeira (below) units. The c. 2000 m thick Capelada Unit comprises (originally in the pre-recumbent folding pile, bottom to top, Arenas et al., 2016, or top to bottom, Puelles et al., 2012 and references therein): ultramafic rocks (including the Herberia massif, see below), high-P mafic granulites, eclogites, and eclogitic paragneisses, the latter with inclusions of metagranitic-tonalitic gneisses and eclogites. The Cedeira Unit bears migmatitic gneisses (Chimparra Gneisses), and high-P granulites, high-T amphibolites, and coronitic metagabbros (Candieira Formation) with general slightly lower metamorphic grade (Vogel, 1967; Gil Ibarguchi et al., 1999; Arenas et al., 2016; Beranoaguirre et al., 2022 and references therein). To be noted is that the base the Candieira Formation is a complex tectonic boundary (Carreiro Zone of Tectonic Movement) (Vogel, 1967) that separates the HP-HT Cedeira unit from the Purrido Ophiolite. In this shear zone, mylonitic metaultramafic rocks (garnet-bearing harzburgites and Ti-clinohumite-bearing orthopyroxenites) indicate high to ultra-high-P conditions likely developed during subduction (Gil Ibarguchi et al.,

1999). On the other hand, the protoliths of the IP and HP-HT units (latest Ediacaran, <550 Ma, to early Ordovician, >470 Ma) are considered to have developed within the framework of a long-lived Cadomian *peri*-Gonwanan continental-to-transitional magmatic arc setting that evolved through rifting to a passive margin (Arenas et al., 2016; Martínez Catalán et al., 2019; Beranoaguirre et al., 2022 and references therein).

Below the Upper Units, the suprasubduction Purrido and Moeche ophiolites occur, both part of the Upper Ophiolitic Units of Devonian age (Sánchez Martínez et al., 2007, 2011; Arenas et al., 2014). The Purrido Ophiolite is located at the western-most part of the Cabo Ortegal Complex and contains amphibolites and garnet amphibolites. The Moeche Ophiolite consists of greenschists interlayered with scarce phyllites and serpentinites. Underneath the Upper Ophiolitic Units, the Basal Units are represented by the Espasante Unit, which consists of felsic orthogneisses and alternating metabasites and scarce layers of garnet schists. Finally, the Somozas Mélange is the lowest structural unit in the Cabo Ortegal Complex (Arenas et al., 1986, 2009; Marcos et al., 2002; Novo-Fernández et al., 2016). The age of high-pressure metamorphism is ca. 400–390 Ma in the HP-HT rocks, ca. 390–377 Ma in the mélange, and ca. 377–370 Ma in the Basal Units (Novo-Fernández et al., 2022; Beranoaguirre et al., 2022 and references therein, but see Beranoaguirre et al., 2019 and references therein for younger events, and Fernández-Suárez et al., 2002; Abati et al., 2007 and references therein for older non-Variscan metamorphic events in the allochthonous complexes).

2.2. The Herbeira massif

The ultramafic rocks of the Capelada Unit of the Cabo Ortegal Complex are exposed in three massifs (North to South): Limo, Herbeira and Uzal (Fig. 2). These massifs consist mainly of harzburgites, dunites, pyroxenites, and minor wehrlites and lherzolites, and are interpreted as a section of a suprasubduction heterogeneous upper mantle wedge with involvement of a subducted terrigenous sediment component (Girardeau et al., 1989; Girardeau and Gil Ibarguchi, 1991; Peucat et al., 1990; Santos Zalduegui et al., 1996, 2002; García-Izquierdo et al.,

Table 1

Summary of PGM grains found in the Cabo Ortegal chromitites after hydroseparation.

Type-I chromitite	HS size fraction: <25 µm	N grains
Grain (single or composite)	**Mineral phases**	
Single	RhAsS (hollingworthite)	1
Single	Pt-Fe-Cu-Ni	2
Single	Pt-As	1
PGM grains (single or composite) n = 1	**HS size fraction: 25–45 µm**	
Composite	RhNiAs	1
	(Ni, Fe, Co)S	
	Ir-Fe-Ni	
	Ir-Fe-Pt-Ni-S	
	Ni-As	
	Pt-S-Fe-Ni-Cu	
	Pt-Fe-Ni-S-As	
		Total = 5
Type-II chromitite	**HS size fraction: <25 µm**	**N grains**
PGM grain (single or composite)	**Mineral**	
Single	Pt-Fe-Cu-Ni	3
Composite	Cu-Pt-Fe-Pd	1
	Ni-Fe-S	
Single	(Pt,Ir,Ru,Rh) (As,S)$_2$	3
Composite	RhNiAs	1
	Pt-Ni-Fe-Cu-Ru-Os-Ir	
Composite	RhNiAs	1
	Ir-Fe-Ni	
	Pt-Fe-Ni-Cu-Ir	
	Pt-Ir-Rh-S-As	
PGM grains (single or composite)	**HS size fraction: 25–45 µm**	
Single	Pt-Fe alloys	2
Single	(Pt,Ir,Ru,Rh)(As,S)$_2$	3
Single	PtAs$_2$	1
Single	IrAsS	1
PGM grains (single or composite)	**HS size fraction: 45–75 µm**	
Single	PtAs$_2$	1
		Total = 17

2011). The studied area is located in the Herbeira Massif (Fig. 3), which comprises an eastern and a western domain separated by the Herbeira Trans-Fault (Moreno et al., 2001). Nevertheless, Tilhac et al. (2016) suggested that the main contact between both domains is igneous rather than tectonic.

The eastern domain consists of spinel harzburgites and minor pyroxenites (<10 %), dunites, and chromitites, while the western domain is made of 1) dunites and chromitites, 2) pyroxenites interlayered with dunites and harzburgites, and local chromitites, and 3) basal spinel harzburgites, which locally contain small bodies of chromitites with a dunitic envelope (Moreno et al., 2001; Puelles et al., 2012; Tilhac et al., 2016).

Regarding the pyroxenites, four different types are identified in the upper part of the massif: type 1) clinopyroxenites with dunites, type 2) massive websterites, type 3) amphibolitized clinopyroxenites, and type 4) orthopyroxene-rich websterites (Tilhac et al., 2016). The primary magmatic stage of formation of pyroxenites took place at < 12 kbar, and a second melting stage of peridotite took place at < 20 kbar (Tilhac et al., 2016). Importantly, prograde (i.e. up-pressure) replacements of spinel by garnet are present in (some) type 2 pyroxenites, denoting conditions up to 16–18 kbar and 780–800 °C (Girardeau and Gil Ibarguchi, 1991; Santos Zalduegui et al., 2002; Tilhac et al., 2016). This has been interpreted as evidence for magmatic processes at high pressure (Girardeau and Gil Ibarguchi, 1991; Santos Zalduegui et al., 2002), perhaps triggered by delamination of the massif (arc root) and incorporation into a subduction zone (Tilhac et al., 2016; see also, Moreno et al., 2001). The peridotites mostly have secondary amphibole and a high degree of serpentinization, whereas pyroxenites have a higher degree of amphibolitization than serpentinization.

The origin of the ultramafic rocks of the Herbeira Massif is associated with the infiltration and differentiation of Si-undersaturated picritic to boninitic melts in an old subcontinental lithospheric mantle beneath an arc (Tilhac et al., 2016, 2017, 2020). In this model the interaction between these melts and the host harzburgites generated dunites and chromitites, the former replaced by pyroxenites as the melt differentiated. Subsequently, a late amphibolitization stage occurred due to the cooling of hydrated residual melts, which produced the metasomatism of pyroxenites and peridotites. Other models involve batches of mantle-derived magmas forming a stratiform pyroxenite-dunite association at the crust-mantle interface below an arc (Moreno et al., 2001), or partial melting of residual oceanic tectonites or sub-arc mantle caused by the addition of supercritical fluids/melts in a suprasubduction environment with accumulation of magma to form pyroxenites and dunites from various parental liquids (Peucat et al., 1990; Girardeau and Gil Ibarguchi, 1991; Santos Zalduegui et al., 2002). Elemental and isotopic data indicate an enriched component in the pyroxenites, introduced into the mantle source during subduction (Santos Zalduegui et al., 2002; Tilhac et al., 2016, 2017, 2020). The age of this magmatic event and of the varied associated protoliths is however controversial.

Internal Sm–Nd and Rb-Sr clinopyroxene–garnet–whole rock isochrons from garnet pyroxenites have yielded ages of 390 and 280 Ma and ca. 229 Ma (Santos Zalduegui et al., 2002; Tilhac et al., 2017, respectively). Tilhac et al. (2017) also reported Sm-Nd and Rb-Sr clinopyroxene–amphibole "isochrons" from pyroxenites in the ranges 332–298 Ma and 352–322 Ma, respectively. All ages except the ca. 390 Ma Sm-Nd garnet-clinopyroxene-whole rock age indicate isotopic disequilibrium, while the Devonian 390 Ma age of Santos Zalduegui et al. (2002) bears a clear geological meaning for it is consistent with rutile ages in a garnet–rutile clinopyroxenite and with ages of HP-HT metamorphism in the Upper Units of the Cabo Ortegal Complex (Santos Zalduegui et al., 1996, 2002; Ordóñez Casado et al., 2001; Novo-Fernández et al., 2022 and references therein). This age would indicate generalized recrystallization at ca. 800 °C and 16–18 kbar at 400–390 Ma of the garnet pyroxenites, and likely of other ultramafic rocks, during the subduction-related metamorphic event that produced HP-HT granulites and eclogitic rocks in the Capelada Unit. Amphibolitization may have taken place latter, at 380 Ma, when the HP-HT rocks of the Capelada Unit exhumed (Arenas et al., 2016 and references therein).

Sm-Nd whole-rock–clinopyroxene isochrons in pyroxenites have yielded Cambrian ages (ca. 500 Ma), interpreted as the age of the magmatic-metasomatic protoliths (Santos Zalduegui et al., 2002; Tilhac et al., 2017). It merits mention that Cambrian-early Ordovician ages characterize those of the protoliths of all other formations of the HP-HT units, including the U-Pb zircon crystallization ages of the gabbroic protoliths of the granulites, eclogites, and orthogneisses (Fernández-Suárez et al., 2007; Ordóñez Casado et al., 2001; Albert et al., 2013; Beranoaguirre et al., 2020, 2022) and the U-Pb detrital zircon 521–510 Ma maximum depositional age of the paragneisses (Albert et al., 2015). All these ages imply the presence of different levels of an entire early Paleozoic crust-mantle arc section constructed onto the extended continental margin of Gondwana or a pre-Gondwanan continental block (Albert et al., 2015; Tilhac et al., 2017). However, all these data and interpretations are opposed to ca. 390 Ma magmatic zircons from spinel harzburgite and garnet pyroxenite that indicate a Devonian (rather than Cambrian) melting event (Ordóñez Casado et al., 2001). Either these zircons indicate re-melting during the Devonian subduction-related event at high pressure (mantle wedge/subarc depths) or could be reinterpreted as metamorphic (formed during subduction?) rather than magmatic. In any case, these zircons indicate an important thermal imprint of the ultramafic rocks during Devonian times.

2.3. Chromitite bodies

The chromitite bodies of the Herbeira massif are mostly hosted in dunites of the western domain of the massif (Fig. 3). According to
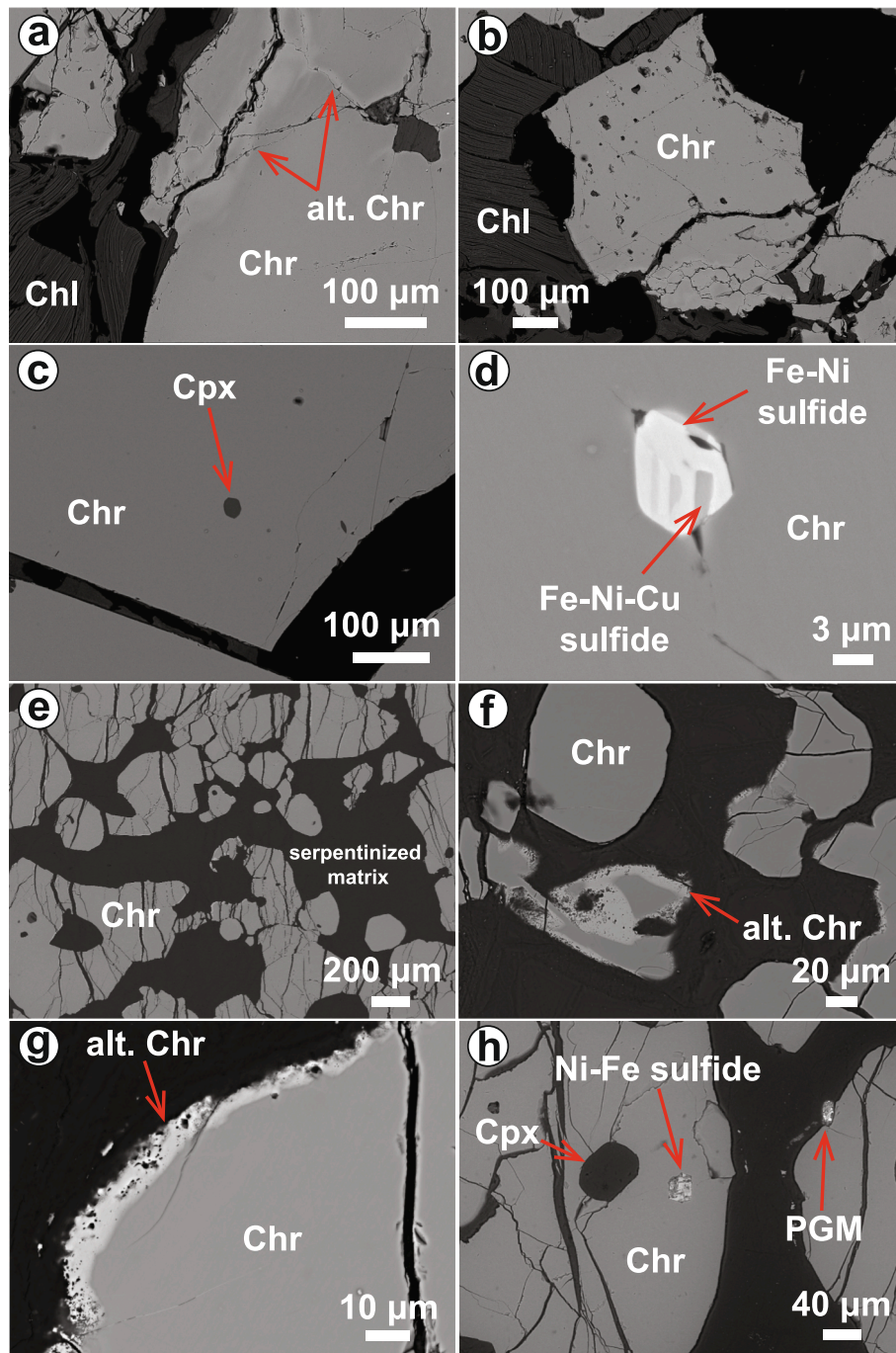
Fig. 5. Textural details of the studied chromitites (backscattered electron image). a) Type-I chromitite. Chlorite (Chl) filling fractures of chromite (Chr) grains showing alteration along fractures (bright phase). b) Type-I chromitite. Triple junctions in fractured chromite. c) Type-I chromitite. Clinopyroxene (Cpx) inclusion within chromite. d) Idiomorphic inclusion of Fe-Ni-Cu with Fe-Ni sulfide within chromite. e) Type-II chromitite. Chromite grains with interstitial altered silicates. Chromite shows pull-apart fractures. f) and g) Type-II chromitite. Alteration rims around chromite. h) Type-II chromitite. Inclusions of clinopyroxene and Ni-Fe sulfide within chromite. A PGM occur at the edge of chromite.

Moreno et al. (2001), these dunites can be grouped into two units; lower and upper dunite, separated by a garnet-bearing pyroxenite dominated unit. The chromitite bodies in the lower dunite unit are scarce and occur as a few irregular and discontinuous layers up to 5 cm thick. They are PGE depleted with values up to 108 ppb (Moreno et al., 2001). On the other hand, the upper dunite unit hosts the highest amount of chromitites, which are highly enriched in PGE with contents up to 13,000 ppb (Moreno et al., 1999). The chromite mineralization occurs as disseminated grains, irregular pods, thin layers, and bands up to 0.50 m thick (Moreno et al., 2001 and references therein).

The studied chromitites are located in the upper dunite unit of the western domain of the Herbeira massif (Fig. 3; black star). They correspond to massive bodies (>80 vol% chromite) of a few meters long with irregular thickness (up to few tens of cm) hosted in dunites (Fig. 4a) and semi-massive horizons (50–80 vol% chromite) of up to a few tens of centimeters length, and < 1 to 3 cm of thickness, mainly hosted in dunites intercalated with minor pyroxenite layers (Fig. 4b, c). In this study, the massive chromitite pods and semi-massive horizons will be referred to as Type-I and Type-II chromitites, respectively.
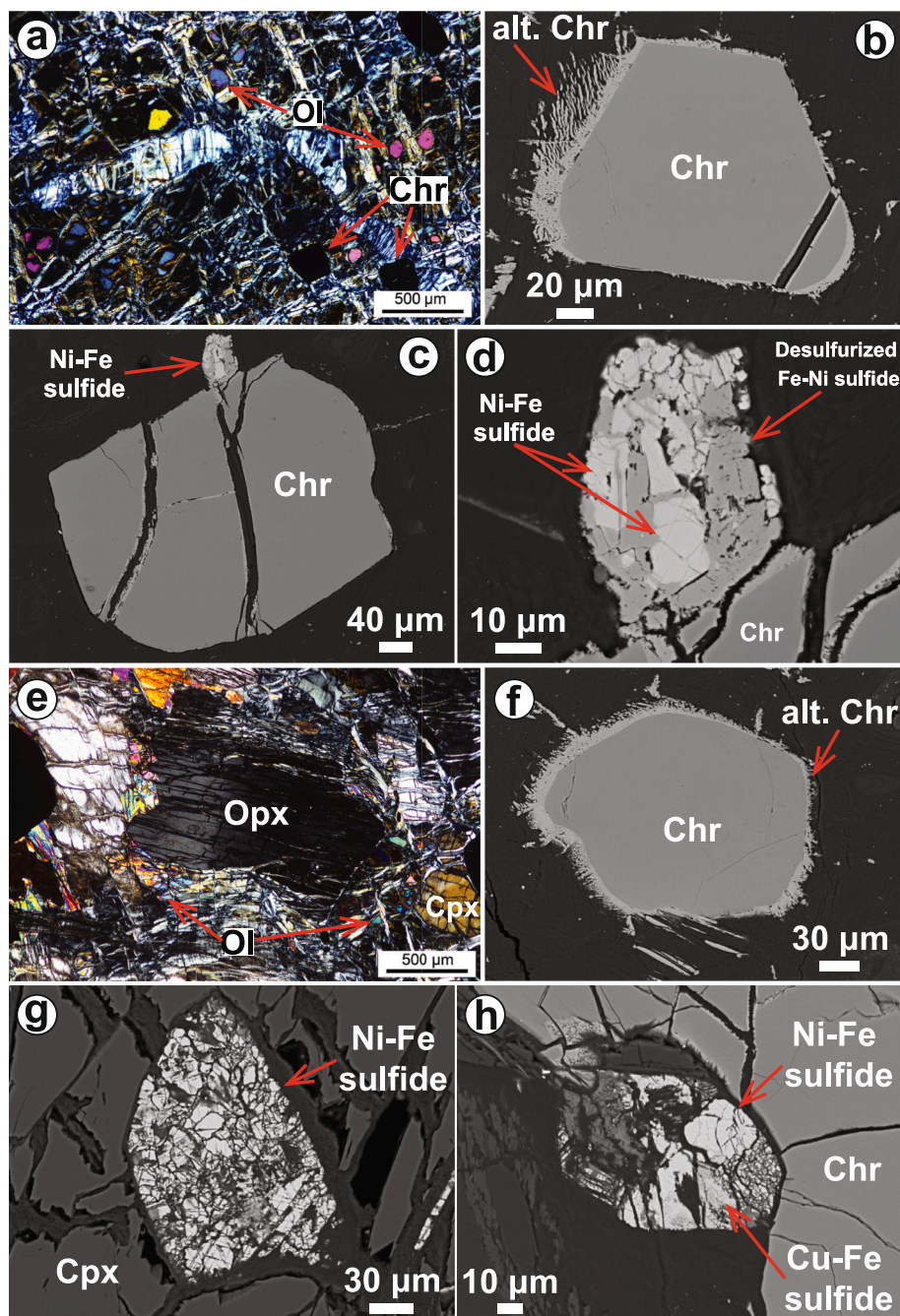
Fig. 6. Textural details of dunite and pyroxenite. a) Dunite. Mesh texture with relics of primary olivine, and accessory chromite (transmitted light). b) Dunite. Alteration rim around accessory chromite (backscattered electron image). c) and d) Partly desulfurized Ni-Fe sulfide on the edge of accessory chromite (backscattered electron images). e) Pyroxenite. Orthopyroxene (Opx) with undulant extinction (transmitted light). f) Pyroxenite. Alteration rim around accessory chromite (backscattered electron image). g) Pyroxenite. Fractured Ni-Fe sulfide inclusion within clinopyroxene (Cpx) (backscattered electron image). h) Pyroxenite. Fractured Ni-Fe sulfide on the edge of accessory chromite (backscattered electron image).

3. Studied samples and analytical techniques

The samples collected for this study represent different types of PGE-rich chromitites and their associated lithologies from the upper dunite unit of the western domain of the Herbeira Massif. Several polished thin sections (from Type-I chromitites, from the contact between Type-II chromitites and dunites, and pyroxenites, and from the contact between dunite and pyroxenite) were studied by means of optical and scanning electron microscopy (SEM). The SEM images and qualitative identification of platinum-group minerals (PGM) and base-metal sulfides (BMS) by means of energy-dispersive spectroscopy (EDS) were

obtained with a field emission scanning electron microscope (FE-SEM) JEOL JSM-7100 at the *Centres Científics i Tecnològics de la Universitat de Barcelona* (CCiTUB), Spain, and a ZEISS Sigma 300 VP at the *Laboratories for Quantitative Target Mineralogy (QanTmin)* of the Luleå University of Technology (LTU), Sweden. Operating conditions were 20–25 kV accelerating voltage.

The mineral chemistry analyses of chromite, PGM, and BMS were obtained with a JEOL JXA-8230 electron microprobe (EMP) equipped with five wavelength-dispersive spectrometers (WDS) and one EDS spectrometer at the CCiTUB. The analytical conditions are described in detail in Appendix A. Minor and trace elements in chromite from both
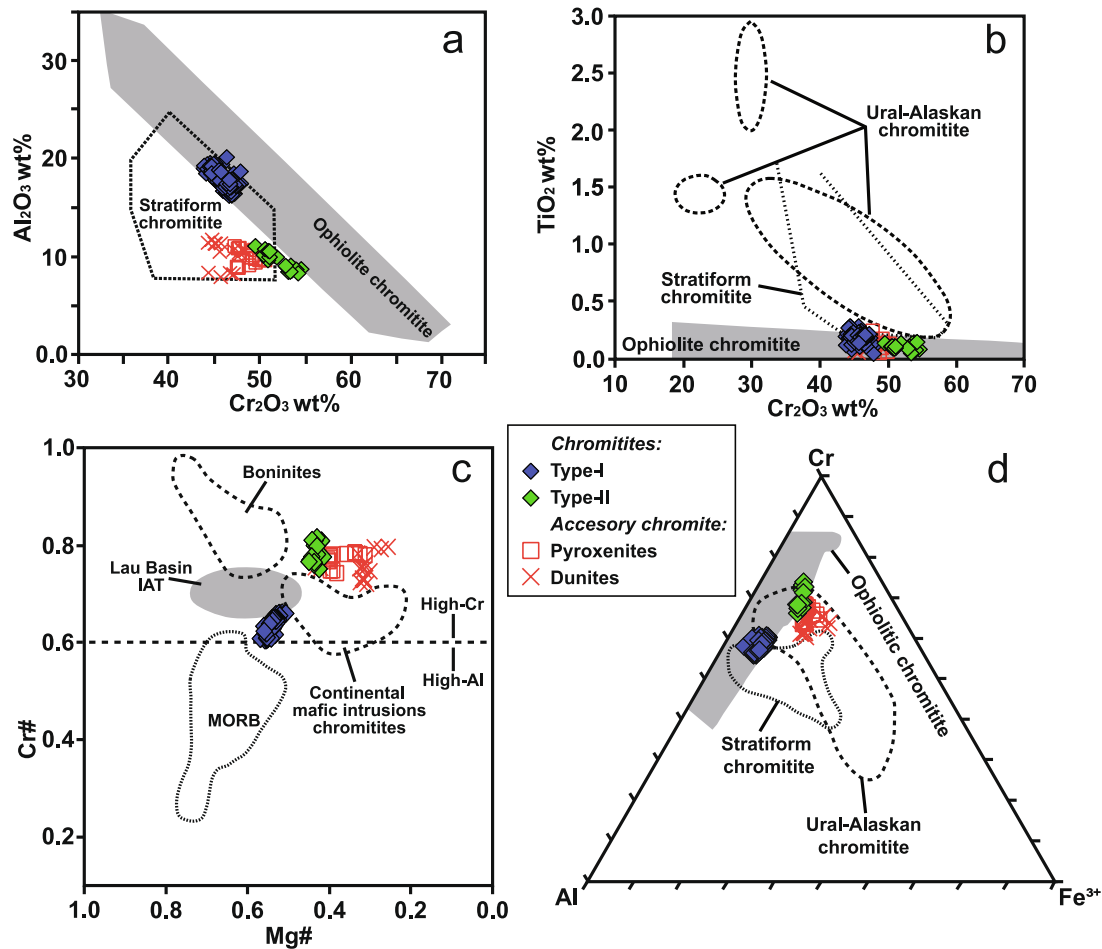
Fig. 7. Chemistry of chromite from chromitites and accessory chromite in dunites and pyroxenites of Cabo Ortegal as compared with chromite from various tectonic settings in terms of a) Al_2O_3 vs. Cr_2O_3, b) TiO_2 vs. Cr_2O_3, c) Cr# [Cr / (Cr + Al), atomic ratio] vs. Mg# [Mg / (Mg + Fe^{2+}), atomic ratio] and d) Al – Cr – Fe^{3+} compositions. Data sources for chromite of different tectonic settings are Bonavia et al. (1993), Kamenetsky et al. (2001), Garuti et al. (2005) and Proenza et al. (2007). Legend is inset in the figure.

types of chromitites, dunites, and pyroxenites, were analyzed by laser ablation inductively coupled mass spectrometry (LA-ICP-MS) at the *Laboratorio de Estudios Isotópicos* (LEI) from the *Centro de Geociencias*, UNAM (Mexico), using a Resolution M−50 Excimer laser coupled to a ThermoICap Qc ICP-MS. The analytical procedure is described in detail in Appendix A. Results of electron microprobe analyses and LA-ICP-MS are presented in Appendix B and Appendix C, respectively.

Whole-rock PGEs analyses were performed on two (Type-I and Type-II) chromitites, one dunite, and one pyroxenite samples at Genalysis Ltd (Perth, Western Australia) by nickel sulfide fire assay collection, following the method described by Chan and Finch (2001). The analytical procedure is described in detail in Appendix A and results are presented in Appendix D.

Representative samples of 1 Type-I chromitite (204 g) and 1 Type-II chromitite (187 g) were crushed, sieved, and processed using hydro-separation (HS-11) (see details in Cabri et al., 2006) at the *QanTmin* labs of LTU to obtain mineral concentrates of different size fractions (<25, 25–45, 45–70, 70–90, and 90–120 μm). The resulting concentrates were mounted first as free grains on metallic cylinders and then as polished monolayers on resin block (SimpliMet 1000) in order to identify mineral phases. PGM and BMS were only found in three HS size fractions of < 25, 25–45, and 45–70 μm (see Table 1).

A thin-foil sample was prepared and extracted from a PGM grain that was included in a polished monolayer from a Type-II chromitite sample by focused ion beam-scanning electron microscopy (FIB-SEM) in the *Laboratorio de Microscopías Avanzadas* (LMA) at the *Instituto de*

Nanociencia de Aragón (INA), University of Zaragoza, Spain. Subsequently, the thin-foil sample was studied by scanning transmission electron microscopy (STEM) and high-resolution electron microscopy (HRTEM) at the same institution. The analytical details for FIB-SEM and STEM-HRTEM analyses are described in Appendix A.

4. Results

4.1. Petrography

Type-I chromitites have massive textures (>80 vol% chromite) and are formed by coarse (>500 μm), anhedral, and fractured chromite grains with serpentine and chlorite filling the fractures and the interstitial space between chromite grains (Fig. 5a-b). Some chromite grains exhibits triple junctions between their grain boundaries (Fig. 5b). Chromite grains are generally unaltered, with alteration limited to very narrow rims and along fractures (bright phases under scanning electron microscope; Fig. 5a). Chromite contains some silicate inclusions such as clinopyroxene (Fig. 5c), chlorite, and amphibole, and sulfides (mainly pentlandite and chalcopyrite; Fig. 5d), PGM, and locally apatite.

Type-II chromitites have semi-massive textures (50–80 vol% chromite) and are formed by subhedral to anhedral chromite grains up to 450 μm that show pervasive pull-apart fractures (Fig. 5e). Some chromite grains are surrounded by thin altered brighter Fe-rich rims (Fig. 5f-g), and this alteration also occurs in fractures. In comparison with Type-I chromitites, the degree of alteration in Type-II chromitites is higher.
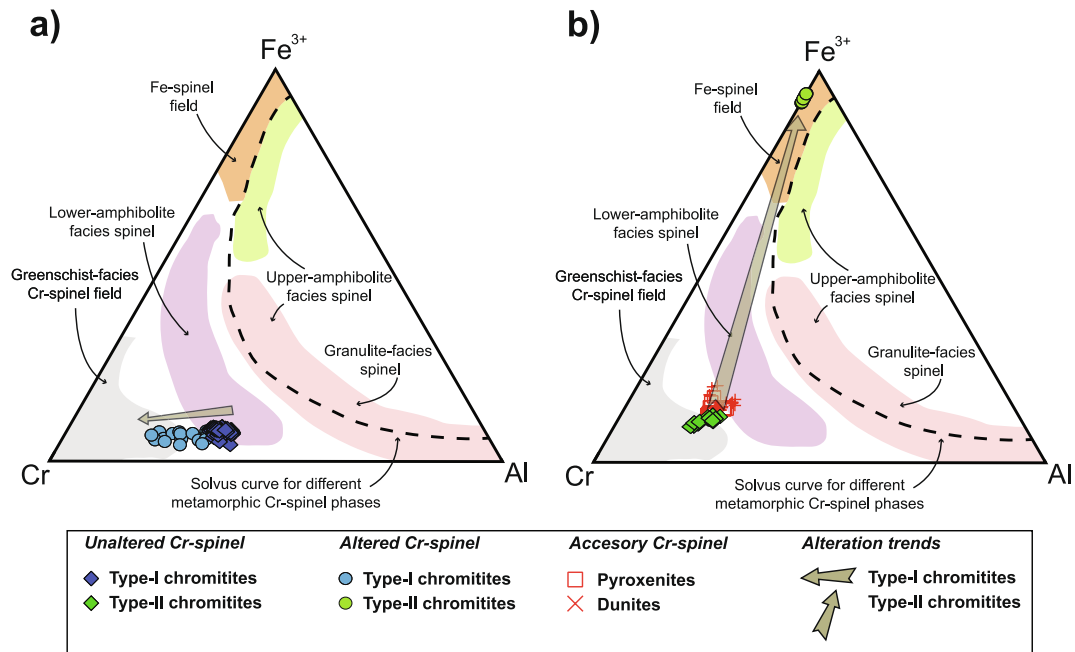
Fig. 8. Fe^{3+}-Cr-Al ternary diagram of Cabo Ortegal unaltered and altered Cr-spinel. a) Type-I chromitites. b) Type-II chromitites, dunites, and pyroxenites. Chromite compositional fields from different metamorphic facies are from Purvis et al. (1972), Evans and Frost (1975), and Freitas Suita and Strieder (1996).

Chromite grains have abundant subrounded inclusions of silicates (olivine, clinopyroxene, and amphibole) with sizes between 20 and 150 μm (Fig. 5h). Some of these silicate inclusions are affected by fractures and are serpentinized. Fe-Ni-Cu sulfides (mainly pentlandite and chalcopyrite) and PGM are also present (Fig. 5h), mostly located at the edge of chromite grains, in contact with the serpentinized interstitial matrix. The fractures are filled with serpentine group minerals and chlorite.

Dunites hosting the Type-II chromitites display mesh textures and preserve relics of primary olivine, orthopyroxene, minor clinopyroxene, and accessory chromite (Fig. 6a). Some disseminated magnetite can also be observed in the serpentinized matrix. Accessory chromite occurs as euhedral to subhedral grains, some of them larger than 100 μm, showing thin alteration rims (Fig. 6b). Some Fe-Ni-Cu sulfide inclusions (pentlandite and chalcopyrite) occur on the edge of accessory chromite and in the silicate matrix (Fig. 6c-d).

The pyroxenite layers intercalated with Type-II chromitites are coarse-grained and strongly serpentinized. Clinopyroxene is anhedral, up to 1 mm, and might locally show rims of secondary amphibole. Orthopyroxene occurs with sizes up to 1 mm and exhibits undulose extinction (Fig. 6e). Minor olivine grains in the pyroxenite have sizes of ~ 200 μm and show signs of deformation. Amphibole also occurs in the matrix as subhedral grains ~ 150 μm in size. Accessory disseminated chromite forms euhedral to anhedral grains with sizes up to 400 μm. Some chromite grains show fine alteration rims as observed in the accessory chromite in dunites (Fig. 6f). BMS are present as fractured grains enclosed in clinopyroxene (Fig. 6g) and chromite, or frequently on the edges of the latter (Fig. 6h).

4.2. Chromite composition

Unaltered chromite cores from the Cabo Ortegal chromitites have Cr_2O_3 contents ranging from 43.90 to 54.76 wt%, Al_2O_3 from 8.26 to 20.13 wt%, and TiO_2 from 0.05 to 0.29 wt% (Fig. 7a-b; Appendix B: Table B.1). Type-I chromitites exhibit Cr# [Cr/(Cr + Al) atomic ratio] between 0.60 and 0.66 and Mg# [Mg/(Mg + Fe^{2+}) atomic ratio] from 0.51 to 0.57 (Fig. 7c). On the other hand, Type-II chromitites have Cr# from 0.75 to 0.82 and Mg# from 0.41 to 0.45 (Fig. 7c). The Fe_2O_3 contents in both types of chromitites vary from 3.86 to 9.71 wt% with

Fe^{3+}# [Fe^{3+}/(Fe^{3+}+Cr + Al) atomic ratio] from 0.05 to 0.12, the highest values being from the Type-II chromitites (Fig. 7d).

Altered chromite rims and fractures in both types of chromitites have clear chemical differences (Appendix B: Table B.3). Type-I chromitites show higher Cr and Fe^{2+} but lower Al and Mg than their unaltered chromite cores. The Fe^{3+}# remains similar to that of unaltered chromite, defining an alteration trend characterized by an increase of Cr (Fig. 8a). On the other hand, alteration rims in chromite from Type-II chromitites have higher Fe^{3+}# and Fe^{2+} but lower Cr, Al, and Mg than their unaltered cores, defining an alteration trend towards compositions richer in Fe^{3+} (Fig. 8b).

Accessory chromite from dunites and pyroxenites show similar Cr_2O_3 contents ranging from 44.31 to 50.63 wt%, Al_2O_3 from 7.90 to 11.73 wt%, and TiO_2 from 0.06 to 0.25 wt% (Fig. 7, Appendix B: Table B.2). They have Cr# from 0.72 to 0.80 and Mg# from 0.26 to 0.44, which are similar to those from Type-II chromitites but have higher Fe_2O_3 contents (9.05–14.73 wt%) and Fe^{3+}# (0.12–0.20).

Minor and trace element contents of unaltered chromite core from both types of chromitites (Fig. 9; Appendix C) show that Type-I chromitite display higher Ga (43–51 ppm), Ni (732–838 ppm), Ti (970–1033 ppm), Zn (1260–1318 ppm), and V (1886–1971 ppm), but lower Sc (2–3 ppm), Co (250–254 ppm), and Mn (1641–1727 ppm) than Type-II chromitite (Ga = 20–23 ppm, Ni = 630–676 ppm, Ti = 393–436 ppm, Zn = 871–903 ppm, V = 1661–1812 ppm, Sc = 5–6 ppm, Co = 332–341 ppm, Mn = 2261–2357 ppm). The Ti, Ni, Co, Mn, and Sc are within the range for high-Cr ophiolitic chromitites. Nevertheless, the Ga contents from Type-I chromitites are within the range for high-Al ophiolitic chromitites, whereas those from Type-II chromitites are within the field of high-Cr ophiolitic chromitites (Fig. 9).

Accessory chromite in dunites (Fig. 9) show similar Sc (4–6 ppm), Ga (22–28 ppm), Co (353–501 ppm), Ti (517–613 ppm), Ni (538–859 ppm), higher Zn (983–1350 ppm), but lower Mn (2194–2798 ppm), V (1811–1957 ppm) than those from pyroxenites (Sc = 5–7 ppm, Ga = 22–31 ppm, Co = 358–460 ppm, Ti = 517–757 ppm, Ni = 585–845 ppm, Zn = 797–1149 ppm, Mn = 2389–2970 ppm, V = 1737–2280 ppm). The Ti, Ni, Sc, and Ga contents are similar to those from Type-II chromitites and consequently to chromite from high-Cr ophiolitic chromitite (Fig. 9). However, in terms of V, Co, Zn, and Mn these contents are
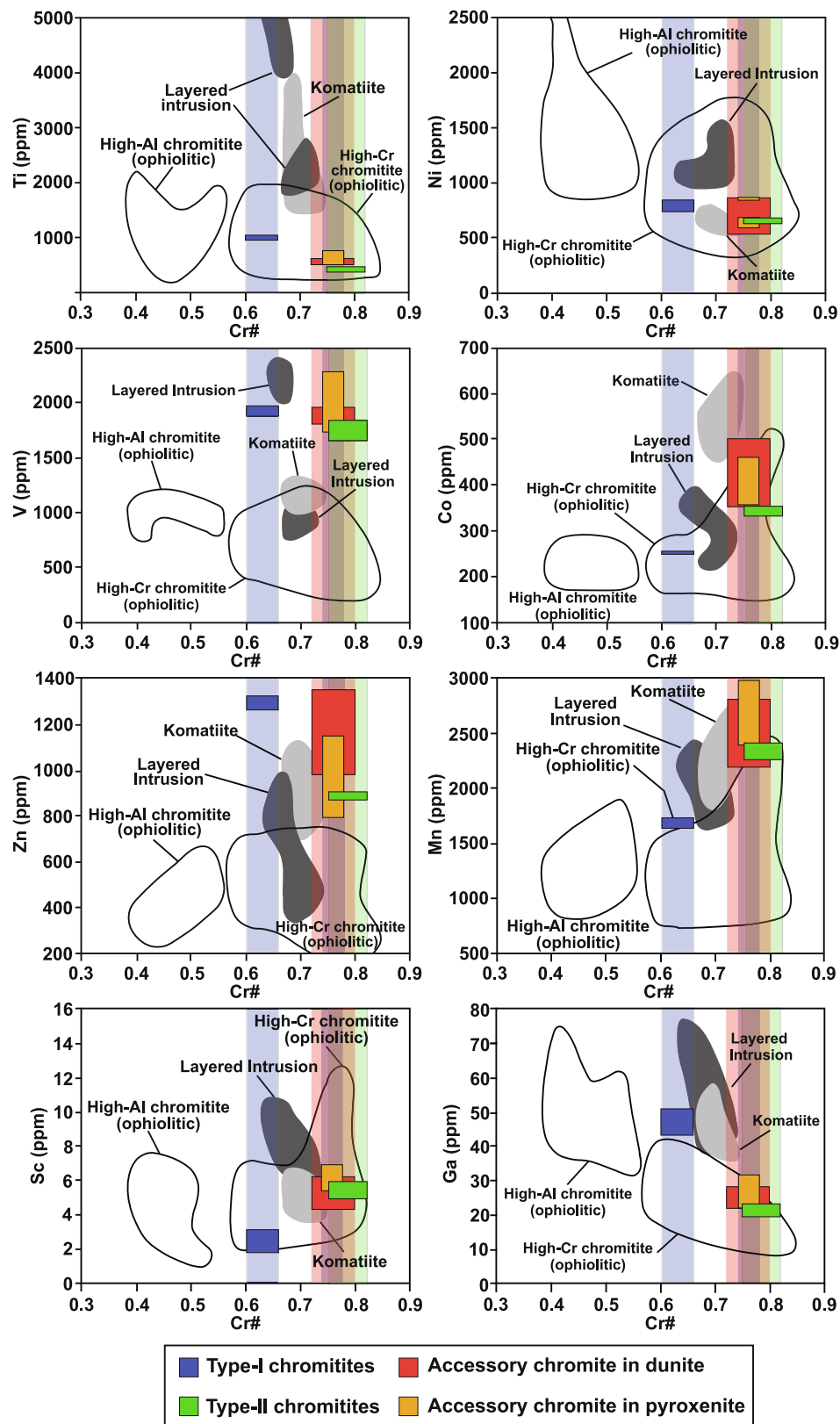
Fig. 9. Compositional variation in terms of Cr# vs Ti, Ni, V, Co, Zn, Mn, Sc and Ga in chromite from the studied chromitites, dunites and pyroxenites. Data sources taken from González-Jiménez et al., (2017a).
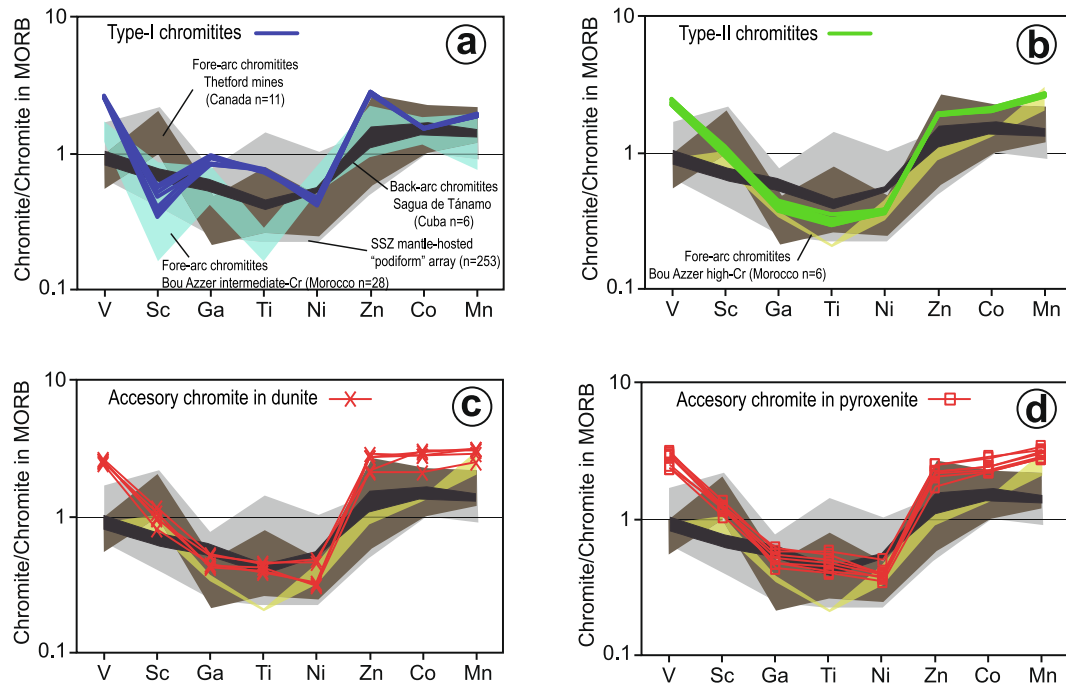
Fig. 10. Spider diagram showing the composition of minor and trace elements of chromite from the Cabo Ortegal chromitites and ultramafic rocks. Data are normalized to MORB (Pagé and Barnes, 2009) and compared with representative Thetford mines fore-arc chromitites (Pagé and Barnes, 2009), Bou Azzer intermediate- and high-Cr fore-arc chromitites (Pujol-Solà et al., 2021), Sagua de Tánamo back-arc chromitites (González-Jiménez et al., 2015a), and suprasubduction mantle-hosted podiform chromitite array (González-Jiménez et al., 2017a).

higher when compared to Type-II chromitites.

4.3. Platinum group elements (PGEs) geochemistry

Bulk-rock PGE contents of the Cabo Ortegal chromitites show that Type-I chromitites have 2,460 ppb and Type-II chromitites have 3,600 ppb (Appendix D). Chondrite-normalized (Naldrett and Duke, 1980) PGE patterns for both types of chromitites (Fig. 11) exhibit an enrichment in PPGEs (Rh, Pt, and Pd) relative to IPGEs (Os, Ir, and Ru), defining a positive slope from Ru to Pt and a negative slope between Pt and Pd.

Regarding the host ultramafic rocks, dunites contain 167 ppb total PGEs, whereas pyroxenites contain 324 ppb total PGEs. In both cases, the PGE content is lower than that from Type-I and Type-II chromitites (Appendix D), but much higher than that of the primitive mantle (i.e. 23.5 ppb; after McDonough and Sun, 1995) and global ophiolitic mantle peridotites (see Table 4 in Bhat et al., 2021). The chondrite-normalized PGE contents of the ultramafic rocks also show an enrichment in PPGEs relative to IPGEs. These rocks display a negative Ru anomaly with respect to Ir, and Rh (Fig. 11).

The Pt/Pd ratio (Appendix D) in Type-I chromitites is higher (Pt/Pd = 5.1) than Type-II chromitites (Pt/Pd = 2.1) and the host ultramafic rocks (dunite; Pt/Pd = 0.9, and pyroxenite; Pt/Pd = 2.0). The distribution of PGEs observed both for the chromitites and for the host ultramafic rocks agrees with the PGE mineralogy observed in these rocks, which consists mostly of PGM enriched in Pt and Pd (see below).

4.4. Platinum-group minerals (PGM) and base-metal sulfides (BMS)

The PGM assemblage observed in situ on thin sections consists of Rh-Ir-Pt-bearing arsenides and sulfarsenides, Pt-Ir-Pd-base-metal-bearing alloys, and Pt-Pd-bearing sulfides (Figs. 12 and 13). PGM from Type-I and Type-II chromitites are mostly located on the edges of chromite grains and in the serpentinized silicate matrix. Due to their small size (<5 μm) and complex textures (replacement/intergrowth), these PGM could only be analyzed qualitatively (see Appendix E).

4.4.1. PGM and associated BMS included on the edge of chromite grains

The PGM assemblage on the edge of chromite is either enclosed within chromite grains or in direct contact with the silicate matrix and comprises Rh-Ir-Pt bearing sulfarsenides and arsenides, Pt-Ir-Pd-base-metal bearing alloys, and Pt-Pd sulfides (Fig. 12; Appendix F).

The PGM observed within chromite are a few grains of Pt-Fe-Cu-Ni alloys with Cu-Fe and Ni-Fe sulfides (probably chalcopyrite and pentlandite, respectively), and Pt-Pd sulfides, all close to the edge of chromite (Fig. 12a, b). The Pt-Fe-Cu-Ni alloys occur as irregular shaped grains enclosed on the edges of the Ni-Fe sulfide associated with Cu-Fe sulfide, amphibole, and chlorite (Fig. 12a). In contrast, Pt-Pd sulfides consist of irregular aggregates (<10 μm) of particles of micrometric size (Fig. 12b). Some of these microparticles occur with needle-like and blocky morphologies.

The PGM observed on the edge of chromite in contact with secondary minerals (e.g., serpentine and/or chlorite; Fig. 12e) from the silicate matrix are Rh-Ir-Pt bearing sulfarsenides [probably hollingworthite (Rh-As-S)-irarsite (Ir-As-S)] with Ir-Pt-Fe, Pt-Pd-S with Pt-Pd-Fe and Ni-Fe sulfides (probably pentlandite), Pt-Fe (−Cu-Ni), and Pt-Pd-As with Ni-Fe and Cu-Fe sulfides (Fig. 12c-f).

Rh-Ir-Pt sulfarsenides occur as small polygonal grains (<7 μm) that contain platy-shaped microparticles of Ir-Fe-Ni alloys (Fig. 12c), whereas Pt-Pd sulfides included within Pt-Pd-Fe alloys are found associated with partially oxidized Ni-Fe sulfides (Fig. 12d). Also, Pt-Pd sulfides occur as single grains on the edge of chromite (Appendix F: Fig. F.1). On the other hand, single aggregates of Pt-Fe(−Cu-Ni) alloys (<5 μm) display porous textures (Fig. 12e). With respect to the Pt-Pd bearing arsenides, they occur as small irregular shaped grains (<10 μm) often found on the edges of Ni-Fe and Cu-Fe sulfides, locally partially oxidized (Fig. 12f; Appendix F: Fig. F.2).

Regarding BMS, they are completely included in chromite and usually occur as single or composite grains of Ni, Ni-Fe and Cu-Fe sulfides without PGM. Generally, they are found as euhedral (Fig. 5d and 12 h) to anhedral grains and some of them display subrounded morphologies (Fig. 12g; Appendix F: Fig. F.3-5).
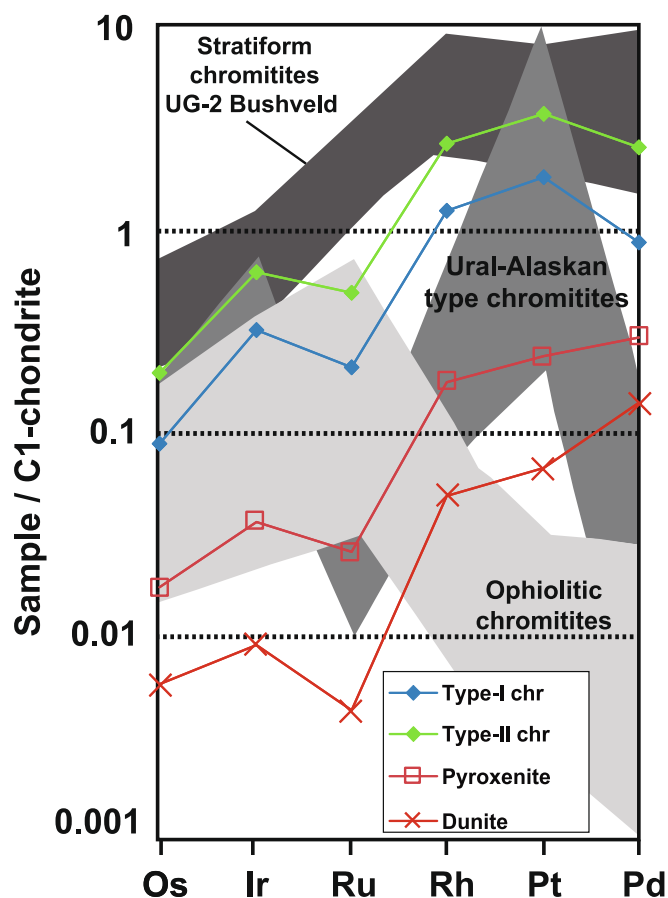
Fig. 11. C1 chondrite-normalized (Naldrett and Duke, 1980) patterns of the Cabo Ortegal chromitites, dunites, and pyroxenites, and comparison with chromitites hosted in the ophiolitic mantle (Proenza et al., 2007 and references therein). Data for Ural-Alaskan-type complexes of the Urals are from Garuti et al., (2003,2005) and those for layered UG-2 Bushveld chromitites are from Naldrett et al. (2012).

4.4.2. PGM and associated BMS in fractures and in the serpentinized silicate matrix

The PGM assemblage located in chromite fractures and in the interstitial silicate matrix correspond to Pt-Pd sulfides, Rh-Ni bearing arsenides, and Pt-Ir-Fe-Ni bearing alloys (Fig. 13). These PGM are often embedded in secondary silicates (e.g., chlorite and/or serpentine). Pt-Pd-S grains occur in the silicate matrix; they are fractured and show irregular morphologies, with less than 5 μm in size (Fig. 13a; Appendix F: Fig. F.6). Besides, Pt arsenides and Pt-Fe-Ni sulfides are found in the silicate matrix as single irregular shaped grains (Appendix F: Fig. F.7). On the other hand, Pt-Ni-Fe and Pt-Fe alloys appear as single aggregates that can reach up to 7 μm. They are mostly found in open fractures of chromite grains (Fig. 13b). Composite grains of Rh-Ni-As are irregular in shape and show complex intergrowths with Ir-Fe-Ni and Pt-Fe-Ni-Cu (−Ir-Pd) alloys (Fig. 13c-e; Appendix F: Fig. F.8). Ir-Fe-Ni alloys occurs as small micrometric to nanometric particles embedded in a Rh-Ni-As matrix (Fig. 13d), whereas Pt-Fe-Ni-Cu (−Ir-Pd) alloys appear as aggregates of micrometer to nanometer-sized particles on the edge of the composite grain of Rh-Ni-As with Ir-Fe-Ni (Fig. 13e). With respect to BMS, they occur in fractures or in the interstitial silicate matrix as irregular grains of Fe-Cu-Ni sulfides (probably pentlandite and chalcopyrite; Fig. 13f).

4.4.3. PGM and associated BMS in mineral concentrates obtained after the hydroseparation process

22 PGM grains were found in the hydroseparated concentrates

(Table 1). The composition of PGM grains was obtained quantitatively (Appendix B) and qualitatively (in small grains or mineral phases < 5 μm and/or with complex textures; Appendix E). The PGM in Type-I chromitites (n = 5) are restricted to fine size fractions (<25 and 25–45 μm). Due to their small size (<5 μm) and complex textures, only two PGM grains were analyzed quantitatively (Appendix B: Table B.4). The recovered PGM correspond to: i) a subidiomorphic grain of RhAsS (hollingworthite) (Fig. 14a, b; Appendix B: Table B.4; analysis 1–8); which shows in the polished surface a more reflective zone and a dendritic intergrowth with no compositional differences (Fig. 14b); ii) two Pt-Fe-Cu-Ni alloys, one with polygonal faces and cracks (Fig. 14c), and one with elongated shape and porous texture (Fig. 14d); iii) one allotriomorphic PtAs grain (Fig. 14e); and iv) one composite grain of RhNiAs with Ir-Fe-Ni, Ir-Fe-Pt-Ni-S, Ni-As, Pt-S-Fe-Ni-Cu, Pt-Fe-Ni-S-As and Ni-Fe-Co sulfides (Fig. 14f-i; Appendix B: Table B.4; analysis 9–10 for RhNiAs and analysis 11–12 for Ni-Fe-Co sulfide). Element mapping of this latter composite grain (Fig. 17, grain from Fig. 14f-i) shows a heterogeneous PGE distribution, where Ru, Pd, Pt and minor Cu and Os are distributed where the intergrowth of RhNiAs with Ir-Fe-Ni is located. On the other hand, minor contents of Cu can be found in the Ni-S-Fe-Rh-As-Ru-Ir phase. It is worth noting that Ru concentrates in an elongated zone within Ni-Fe-Co sulfide (Fig. 17).

PGM in the Type-II chromitites (n = 17) are mostly found in the finest size fractions (<25 and 25–45 μm), except for one PGM grain found in the 45–75 μm size fraction (Table 1). Only fourteen PGM grains from this type of chromitite were analyzed quantitively (see Appendix B; Table B.5). The recovered PGM correspond to: i) five grains of Pt-Fe (Cu-Ni) alloys with irregular shapes and porous textures (Fig. 15a-f), displaying a variable composition between isoferroplatinum, tetraferroplatinum, and tulameenite (Fig. 15d-f and 16; Appendix B: Table B.5; analysis 1–6 and 22–29); ii) one composite grain of irregular shaped Cu-Pt-Fe-Pd alloy occurring with Ni-Fe sulfide (Fig. 15g, h); iii) six subidiomorphic to idiomorphic single grains (5–10 μm) of Pt-Ir-Rh-As-S with calculated ideal formula nearly to (Pt, Ir, Ru, Rh) (As, S)$_2$ that resembles to that of S-rich sperrylite (formerly platarsite; McDonald and Cabri, 2023) (Fig. 15i-j; Appendix B: Table B.5; analysis 10–14 and Fig. 15k, Appendix B: Table B.5; analysis 7–9. Analysis of the remaining grains: 19–21, 30–37, 38 and 43–48); iv) one allotriomorphic single grain of IrAsS (irarsite) (<10 μm in size) (Appendix B: Table B.5; analysis 39–41); v) two grains of PtAs$_2$ (sperrylite) (Fig. 15l; Appendix B: Table B.5; analysis 49–53 from Fig. 15l and analysis 42) that have allotriomorphic to idiomorphic shapes with sizes up to 50 μm; and vi) two composite grains of Rh-Ni-As (compositions near zaccariniite (RhNiAs), Appendix B: Table B.5; analysis 15–17 of PGM of Fig. 15m and analysis 18 of PGM of Fig. 15n) with complex intergrowths of Ir-Pt-Fe-Ni-bearing alloys (Fig. 15m, n). Most of the intergrowths were not quantitatively analyzed due to their small size (<2 μm) and complex textures. One of these grains shows a mineral phase of Pt-Ir-Rh sulfarsenide (Fig. 15n) associated with zaccariniite. Element mapping (Fig. 18, grain from Fig. 15n) reveals the complexity of this grain with zones composed of Pt-Fe-Cu (left edge). On the other hand, Ru concentrates in the Pt-Ir-Rh sulfarsenide phase, whereas Pd concentrated in zaccariniite (Fig. 18).

4.4.4. Micro- and nanostructure of PGM

For a better understanding of these complex grains, we selected the composite grain of RhNiAs with intergrowths of Fe-Cu-Os-Ir-Pt-Ni from Fig. 15m (from Type-II chromitite) to obtain a FIB thin-foil cut across the whole grain to obtain a representative section. The TEM-EDS elemental mapping shows that the matrix is mainly composed of Rh, Ni, As, and Pd, whereas the intergrowths are composed of Fe, Cu, Os, Ir, Pt, and Ni (Fig. 19). A high-resolution TEM image (HRTEM) of one of these intergrowths reveals that is composed of different nanometric-sized polycrystalline aggregates (Fig. 20a). TEM-EDS mapping of the same intergrowth shows that these polycrystalline aggregates of nanoparticles have compositions of Pt-Ni-Fe and Fe-Cu-Ru-Os-Ir (Fig. 20b).
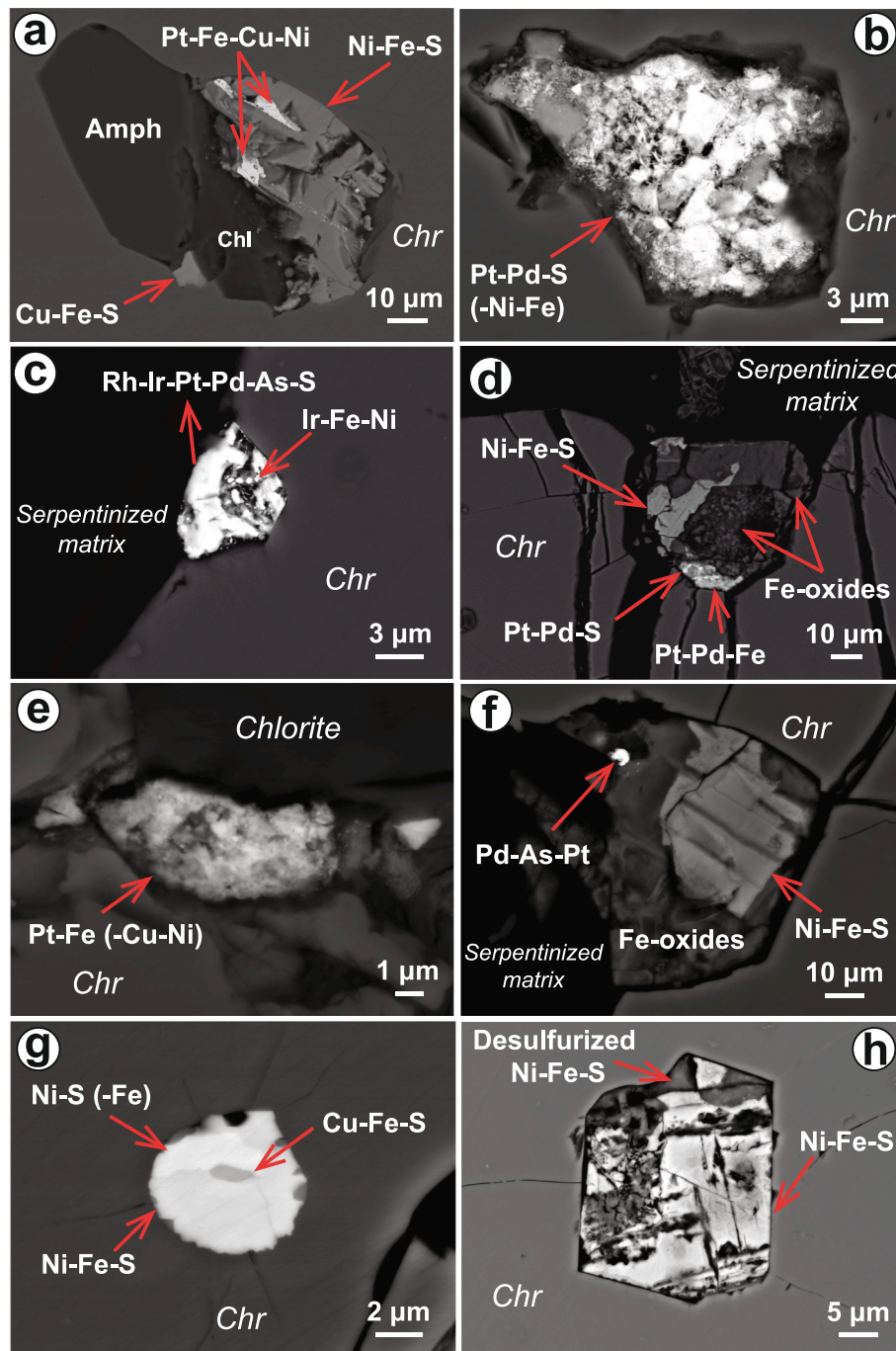
Fig. 12. Backscattered electron images of representative PGM and base-metal sulfides included on the edge of chromite from thin sections of the Cabo Ortegal chromitites. a) Pt-Fe-Cu-Ni alloys with base-metal sulfides, amphibole and chlorite in chromite. b) Pt-Pd sulfide grain included in chromite. c) Polygonal composite grain of Rh-Ir-Pt bearing sulfarsenide with Ir-Fe-Ni alloy. d) Composite grain of Pt-Pd and Ni-Fe sulfides with Pt-Pd-Fe alloys and Fe-oxides. e) Porous Pt-bearing alloy. f) Pt-Pd arsenide with Ni-Fe sulfide and Fe-oxides. g) Subrounded composite grain of Ni, Ni-Fe and Cu-Fe sulfides. h) Partially desulfurized Ni-Fe sulfide. Abbreviations: Amph: amphibole, Chr: chromite, Chl: chlorite.

5. Discussion

5.1. Effects of metamorphism and alteration on mobility of major and minor elements

In the studied chromitites, the alteration is restricted to thin rims and along fractures (Fig. 5a, f-g). The alteration in chromite from Type-I chromitites shows that rims and fractures are enriched in Cr and Fe^{2+} and depleted in Al and Mg when compared to chromite cores (Fig. 8a). On the other hand, the alteration rims in chromite from Type-II

chromitites are enriched in Fe^{3+} (Fig. 8b) and depleted in Cr, Al and Mg in comparison with unaltered chromite cores.

These textural and chemical evidence suggest different stages of alteration, similar to the alteration reported in different ophiolitic chromitites around the globe (Proenza et al., 2004; Gervilla et al., 2012; Colás et al., 2014, 2017, 2019, 2020; González-Jiménez et al., 2015a, 2015b, 2017b; Hernández-González et al., 2020). In the Type-I chromitites, Cr and Fe^{2+} increase under water-saturated reducing conditions to form thin Fe^{2+}-rich rims (Gervilla et al., 2012) and chlorite in the matrix (Fig. 5a). On the other hand, in Type-II chromitites, the presence
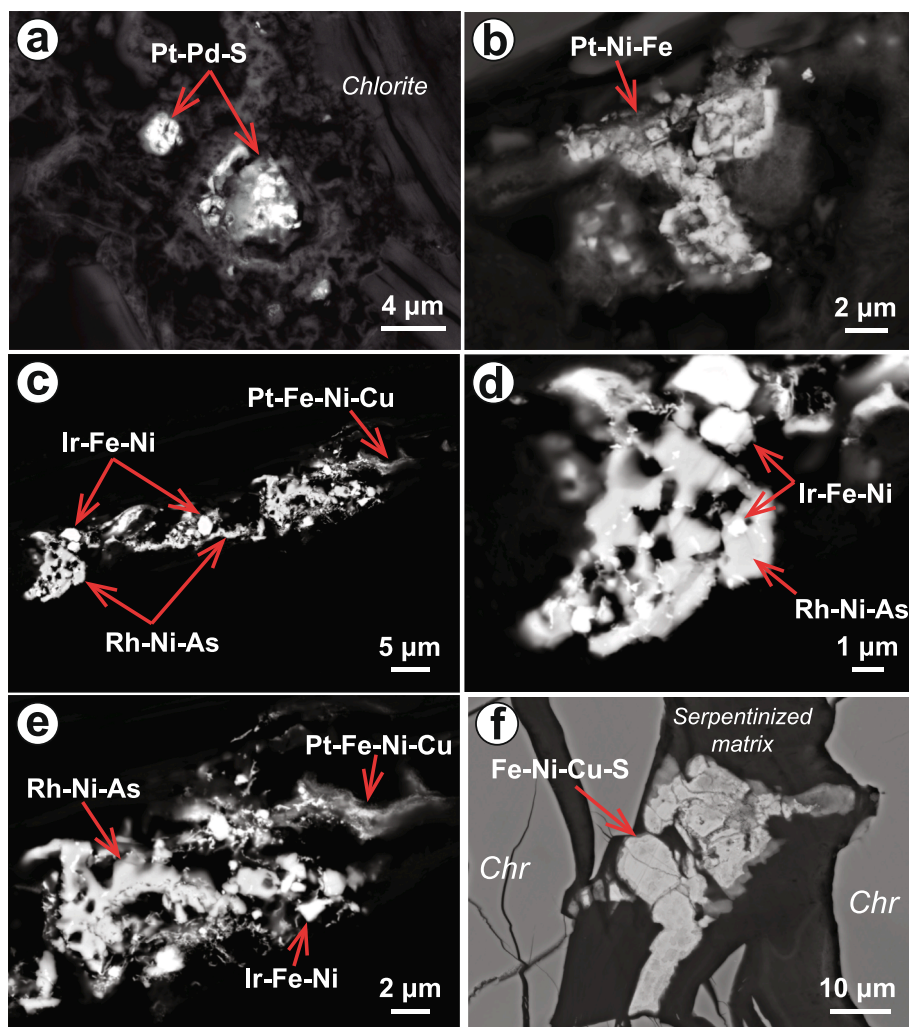
Fig. 13. Backscattered electron images of representative PGM and base-metal sulfides in fractures and in the altered silicate groundmass from thin sections of the Cabo Ortegal chromitites. a) Pt-Pd sulfide embedded in chlorite. b) Pt-Ni-Fe alloy. c) Composite grain of Rh-Ni-As with Ir-Fe-Ni and Pt-Fe-Ni-Cu alloys. e) and f) detail pictures of the grain in c) showing the textural relation between Rh-Ni-As, Ir-Fe-Ni and Pt-Fe-Ni-Cu. f) Fe-Ni-Cu sulfide in a fracture of chromite. Abbreviations: Chr: chromite.

of Fe^{3+}-rich rims around chromite (or fractures) suggest oxidizing conditions that involved the circulation of oxidizing fluids (e.g., Fig. 5f-g). As suggested by Colás et al. (2019) these processes are more effective in chromitites with low chromite/silicate ratios (i.e. semi-massive chromitites). Such alteration processes in both types of chromitites can be linked to the percolation of hydrated fluids during retrograde amphibolite facies metamorphism (8 kbar, 500 °C; Tilhac et al., 2016) that affected the chromitites, dunites, and pyroxenites of Cabo Ortegal.

The major element composition of unaltered chromite cores from Type-I and Type-II chromitites overlap with the field defined for ophiolitic chromitites (Fig. 7b, d). The minor and trace element contents in unaltered chromite cores of the studied chromitites show that Ti, Ni, Co, and Sc are within the range of primary igneous high-Cr ophiolitic chromitites, with exception of Mn, V, and Zn contents, which are higher than those typical for ophiolitic chromitites (Fig. 9). Such enrichments in Mn, V, and Zn in Type-I and Type-II chromitites could suggest subsolidus reequilibration between olivine and chromite promoting an increase in Zn, Co, Mn, Ni, including V and Fe^{3+} as seen in chromite from the podiform chromitites at Kempirsai (Kazakhstan; Hu et al., 2022). On the other hand, the Ga contents in chromite from Type-II chromitites plot within the field of high-Cr ophiolitic chromitites (Ga < 30 ppm), whereas the chromite from Type-I chromitites have higher values, similar to those from high- Al ophiolitic chromitites (Ga > 40 ppm;

Farré-de-Pablo et al., 2020) (Fig. 9). This suggests that chromite from Type-I and Type-II chromitites have Ga contents similar to high-Al and high-Cr ophiolitic chromitites, respectively.

Therefore, major and less mobile minor and trace elements contents in both types of chromitites are within the range of primary igneous chromite, suggesting that the primary chromite composition is preserved.

On the other hand, accessory chromite from dunites and pyroxenites shows similar Cr# and TiO_2 to the Type-II chromitites (Fig. 7b-c) but are more enriched in Fe_2O_3 (Fig. 8b), V, Zn, and Mn (Fig. 9). This enrichment could be linked to the same alteration processes related to subsolidus reequilibration (i.e. promoting an increase in V, Zn, and Mn) and circulation of oxidizing fluids (i.e. increase in Fe^{3+}) (Fig. 8b).

The MORB-normalized trace elements patterns of unaltered chromite cores from Type-I and Type-II chromitites from Cabo Ortegal Complex are similar to those high-Cr chromitites from the oceanic supra-subduction zone (SSZ) mantle, specifically to fore-arc chromitites (Fig. 10a-b). Moreover, the MORB-normalized trace element patterns of accessory chromite from dunites and pyroxenites are similar to that from Type-II chromitites (Fig. 10c-d). All these evidences suggest that the magmatic fingerprint of a fore-arc environment has been preserved in the studied rocks.
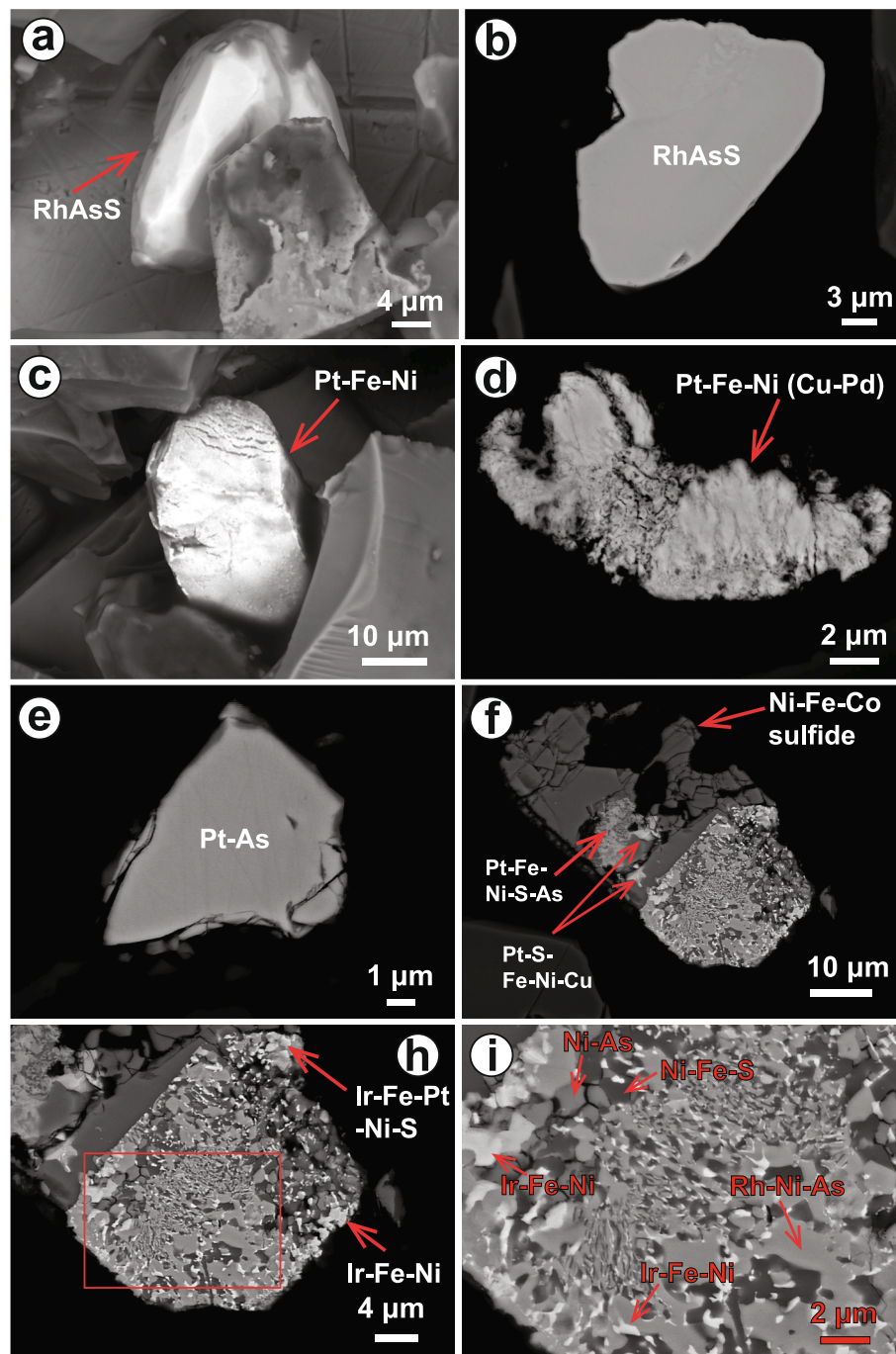
Fig. 14. Backscattered electron images of representative PGM and base-metal sulfides from hydroseparation concentrates of the studied chromitites. a) Sub-idiomorphic grain of RhAsS (hollingworthite). b) Same grain in a) but polished. c) Pt-Fe-Ni alloy. d) Porous Pt-Fe-Ni alloy grain. e) Pt-As grain. f) Composite grain of Rh-Ni-As with Ir-Fe-Ni, Ir-Fe-Pt-Ni-S, Pt-Fe-Ni-S-As, Pt-S-Fe-Ni-Cu and Ni-Fe-Co sulfide. h) Same grain in f) showing the distribution of the Ir-Fe-Pt-Ni-S and Ir-Fe-Ni phases. The red square shows a detailed view in i). i) Rh-Ni-As with intergrowths of Ir-Fe-Ni alloys. Grains of Ni-As showing triple junctions.

5.2. Parental melt compositions

In the Cr# versus Mg# diagram, the composition of chromite from Type-I chromitites falls between the fields defined for accessory Cr-spinel in mid-ocean ridge basalts (MORB) and boninites (Fig. 7c), whereas the composition of chromite from Type-II chromitites falls near the field defined for Cr-spinel in boninites. In the TiO_2 versus Al_2O_3 diagram (Fig. 21a), the composition of chromite from Type-I chromitites overlaps the fields for chromite in abyssal and suprasubduction zone (SSZ) peridotites, whereas the composition of chromite from Type-II chromitites overlaps the fields for chromite in SSZ peridotites and

island arc basalt (IAB). It should be noted that the composition of accessory chromite from dunites and pyroxenites hosting Type-II chromitites also plots within the fields defined for chromite in SSZ peridotites and IAB (Fig. 21a). The composition of this accessory chromite in terms of their TiO_2 and Al_2O_3 contents, and its proximity to the Type-II chromitites bodies suggest that they formed in the same environment.

Because the studied chromite preserves a primary chemical composition, it is possible to estimate their parental melts and, hence, the origin of the chromitites. The composition of the melts in equilibrium with chromite has been estimated using the Al_2O_3 and the TiO_2 contents of chromite from both types of chromitites and the set of equations from

Zaccarini et al. (2011) cited in Dönmez et al. (2014), which were partially derived from data by Kamenetsky et al. (2001). It is worth noting that different sets of equations to estimate the parental melts in equilibrium with chromite have been derived from the approach of Kamenetsky et al. (2001) (e.g., Rollinson, 2008; Pagé and Barnes, 2009; Zhou et al., 2014; Zhu and Zhu, 2020), showing similar results. The Zaccarini's equations use the Al_2O_3 and TiO_2 contents of chromite to calculate the Al_2O_3 and TiO_2 contents of the parental melts using the following equations for high-Cr chromite:

$$(Al_2O_3)_{melt} = 5.2253 Ln(Al_2O_3)_{chromite} - 1.1232$$

$$(TiO_2)_{melt} = 1.0897 (TiO_2)_{chromite} + 0.0892,$$

And the following equations for high-Al chromite:

$$(Al_2O_3)_{melt} = 4.1386 Ln(Al_2O_3)_{chromite} + 2.2828$$

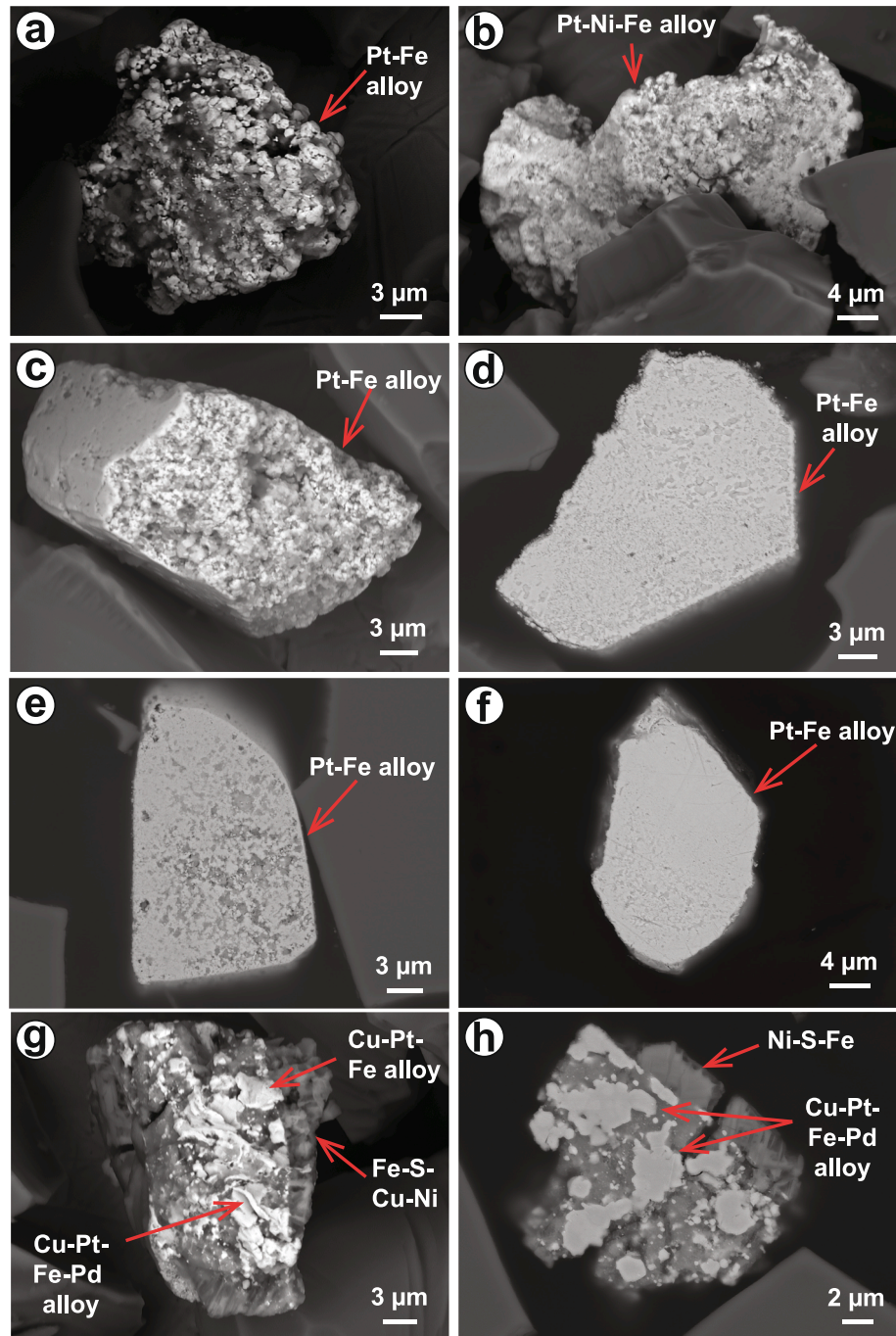$$(TiO_2)_{melt} = 0.708 Ln(TiO_2)_{chromite} + 1.6436$$

Fig. 15. Backscattered electron images of representative PGM and base-metal sulfides from hydroseparation concentrates of the studied chromitites. a), b) and c) Porous Pt-Fe-Ni alloys. d) Same grain in c) but polished. e) and f) Polished grains of Pt-Fe alloys with porous textures. g) Cu-Pt-Fe (Pd) alloy with Fe-Cu-Ni sulfide. h) Polished grain of Cu-Pt-Fe-Pd alloy with Ni-Fe sulfide. i) Subidiomorphic grain of Pt-Ir-Ru-Rh-As-S. j) Same grain of Pt-Ir-Ru-Rh-As-S from i) but polished. k) Idiomorphic grain of Pt-Ir-Ru-Rh-As-S. l) Idiomorphic grain of PtAs₂ (sperrylite). m) Composite grain of Rh-Ni-As with intergrowths of Pt-Ni-Fe and Fe-Cu-Ru-Os-Ir. n) Composite grain of Rh-Ni-As with Ir-Fe-Ni, Pt-Fe-Ni-Cu-Ir and Pt-Ir-Rh-As-S.
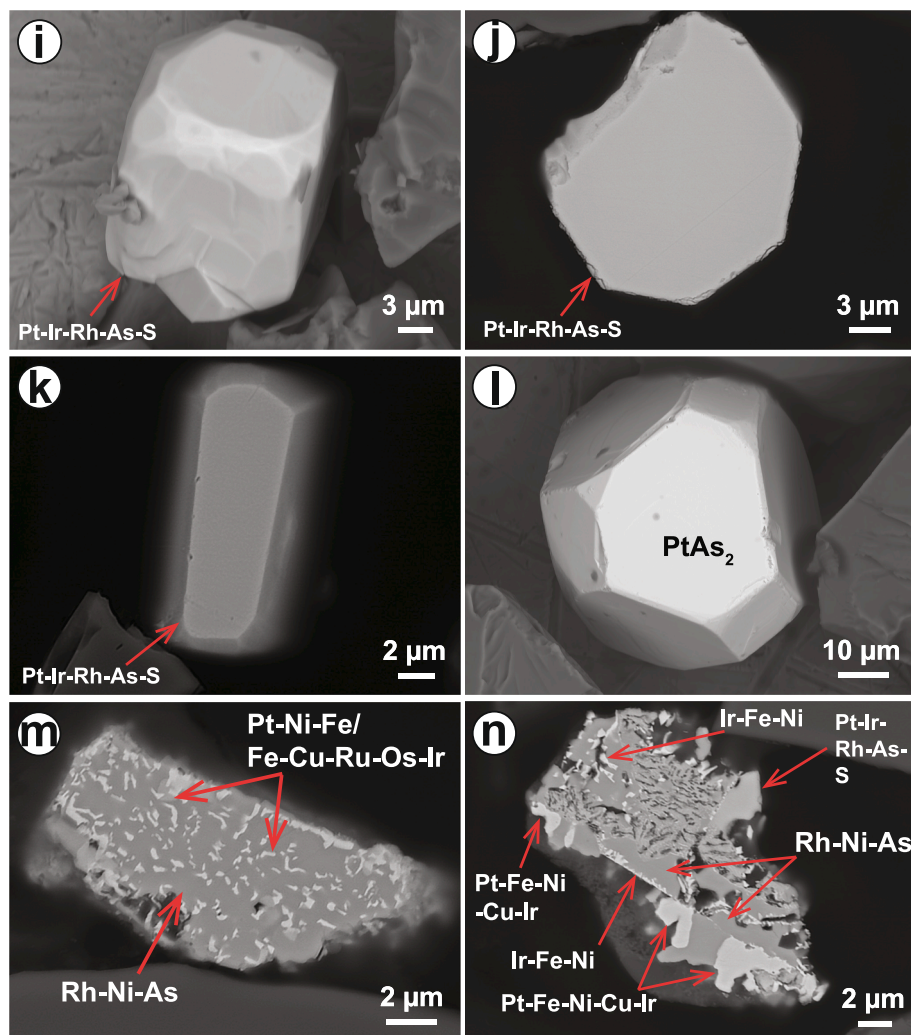
Fig. 15. (*continued*).

The FeO/MgO ratios of the parental melts were estimated using the Maurel (1984, cited by Augé, 1987) empirical expression:

$$Ln(FeO/MgO)_{chromite} = 0.47 - 1.07Al\#_{chromite} + 0.64Fe^{3+}\#_{chromite}$$
$$+ Ln(FeO/MgO)_{melt}$$

with FeO and MgO in wt.%, and $Al\# = Al/(Cr + Al + Fe^{3+})$ and $Fe^{3+}\# = Fe^{3+}/(Cr + Al + Fe^{3+})$, both in atomic proportions.

From these calculation, two different parental melts were identified for the two types of studied chromitites (Fig. 21b). The calculated parental melt for Type-I chromitites yields 13.81 to 14.71 wt% Al_2O_3 and TiO_2 varying between 0.07 to 0.76 wt%, with a FeO/MgO ratio between 1.29–1.59. Both the Al_2O_3 contents and the FeO/MgO ratio are similar to MORB melts (15–16 wt% Al_2O_3, and 1.2–1.6 FeO/MgO; Wilson, 1989; Gale et al., 2013), but not in terms of TiO_2 (Fig. 21b; typical MORB > 1 wt% TiO_2; Stern et al., 2012). The low Ti content in MORB-like melts, together with low Ti/V ratio, are characteristic of fore-arc basalts (FAB, Reagan et al., 2010; Shervais et al., 2019). Rollinson and Adetunji (2013) suggested a FAB-like parental melt composition for ophiolitic chromitites from Maqsad (Oman) with TiO_2 between 0.46–1.06 wt% and 14.52–15.82 wt% Al_2O_3 (typical FAB 15.30 wt% Al_2O_3, 0.97 wt% TiO_2, and 1.58 FeO/MgO; Shervais et al., 2019), which is similar to the estimated composition of parental melt for Type-I chromitites. On the other hand, the calculated parental melt for Type-II chromitites yields 9.91–11.43 wt% Al_2O_3, 0.15–0.25 wt% TiO_2, and FeO/MgO ratio between 1.80–2.09, corresponding to the typical

composition of boninitic melts in terms of Al_2O_3 and TiO_2 contents (Fig. 21b-d) (typical boninites 10.6–14.4 wt% Al_2O_3,0.1–0.5 wt% TiO_2, and 0.7–1.4 FeO/MgO; Hickey and Frey, 1982; 12.93 wt% Al_2O_3, 0.26 wt% TiO_2, and 0.61 FeO/MgO; Shervais et al., 2021).

Summarizing, the estimated parental melt compositions suggests that Type-I chromitites formed from FAB-like melts, whereas Type-II chromitites crystallized from boninitic melts. These melts typically occur in fore-arc region of island arcs affected by extension during subduction. We propose that these same boninitic melts reacted with peridotites to form the pyroxenites of the Herbeira massif (Tilhac et al., 2016). In this context, we suggest that the origin of the Cabo Ortegal chromitites reflects the development of a Cambrian arc (ca. 500 Ma), as proposed by Tilhac et al. (2017) for the Herbeira pyroxenites. Indeed, some authors have suggested that the terranes in north-western Iberia may represent fragments of an ensialic island arc of at least Cambrian-Ordovician age (Andonaegui et al., 2002; Santos Zalduegui et al., 2002).

5.3. Origin of the PGE enrichment in the Cabo Ortegal chromitites and associated rocks

The PPGE enrichment in the studied chromitites resembles that of the Type II chromitites (especially Type IIA) described by González-Jiménez et al., (2014a,2014b). According to these authors, this PPGE enrichment may be related to PGE collection in sulfide melt(s) eventually segregated through immiscibility from evolving, volatile-rich, small-volume melts. These melts are also capable of concentrating S,
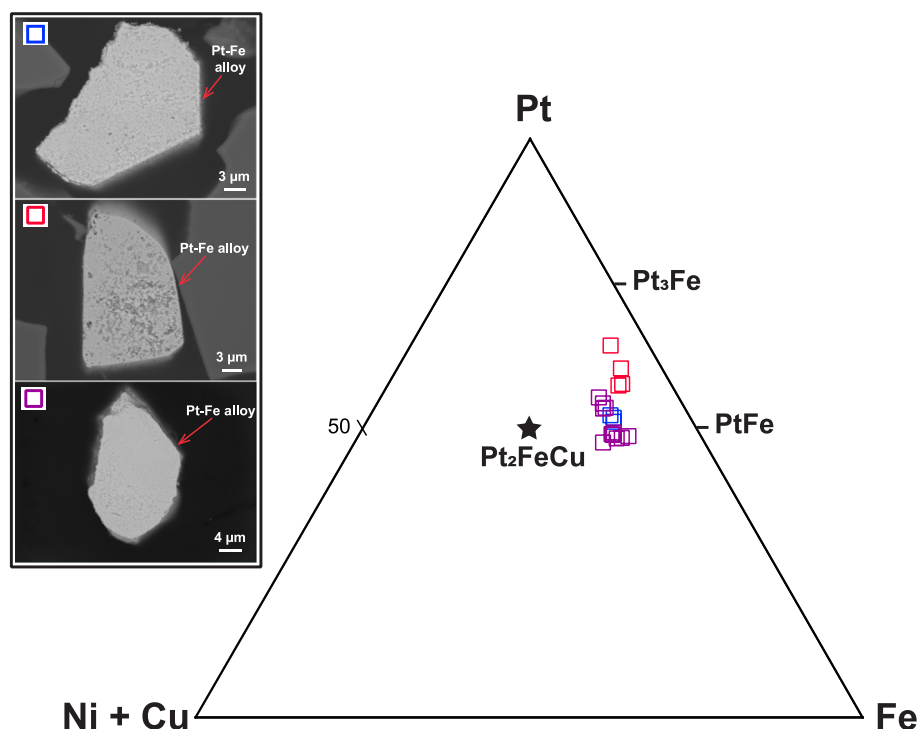
Fig. 16. Compositions of Pt dominated alloys from chromitites of Cabo Ortegal, in the Pt-Fe-Ni + Cu ternary diagram. Colored squares show the composition of the Pt-bearing alloys in the inset. Blue, red, and violet squares correspond to analyses 1–3, 4–6 and 22–29 respectively (Table B.5).

along with PPGE (González-Jiménez et al., 2011), favoring the segregation of immiscible S-As rich melt(s), thereby leading to the collection of base-metals and further incompatible PGE.

These small melt fractions, enriched in volatile components, generated after extensive melt-rock reaction and fractionation, could be responsible of crystallization of the chromitites in Cabo Ortegal, as a result of percolation and differentiation of these melts from FAB-like to boninitic affinities in a sub-arc mantle setting. This is also consistent with the fact that PGM and PGM-bearing sulfides are systematically located at the edge of chromite grains and included in the interstitial silicate matrix (Figs. 12 and 13), evidencing that segregation of sulfide melt(s) probably occurred at late stages of, and after, crystallization of chromite. Furthermore, sulfide segregation could be favored by decreasing S and volatile solubility in the magma as a result of increasing polymerization degree by differentiation processes (e.g., González-Jiménez et al., 2011 and references therein), resulting in Si-richer melts of boninitic affinity parental of the Type-II chromitites (Fig. 21), producing a higher concentration of PGE in the latter compared to Type-I chromitites. These same boninite-like melts reacted with peridotites to form the pyroxenites of the Herbeira massif (Type 2 and 4 pyroxenites; Tilhac et al., 2016). The fact that the shape of chondrite-normalized PGE patterns of the pyroxenite and dunite hosting Type-II chromitites (Fig. 11) are very similar to Type-II chromitites, showing the same PPGE enrichment reinforces this interpretation. Additionally, both Type-I and Type-II chromitites, show similar PGE-distribution patterns. This may be explained by the presence of sulfide mineralization (PGE and base-metals) in these rocks. According to O'Driscoll and González-Jiménez (2016), sulfide-mineralized rocks exhibit enrichment in PPGE over IPGE, represented by steep positive chondrite-normalized PGE patterns, irrespective of the relative PGE abundances. This reflects the immiscible segregation of sulfide melt(s) after extensive fractionation of the silicate melt. Thus, the segregation of the sulfide melt(s) would scavenge the incompatible PGE (Rh, Pt, Pd), due to the chalcophile affinity of these elements (Barnes et al., 1985; Li et al., 1996), and, to a lesser extent, with their higher mobility in volatile-rich systems (Fleet and Wu, 1995 and references therein).

5.4. Origin of the PGM assemblages

5.4.1. Magmatic PGM and BMS assemblages

The studied PGM assemblage consists mostly of Rh-Ir-Pt-bearing arsenides and sulfarsenides, Pt-Ir-Pd-base-metal-bearing alloys, and Pt-Pd sulfides.

According to our observations, PGE-bearing sulfarsenides (irarsite-hollingworthite series) and arsenides (sperrylite) are located at the edges of chromite (Fig. 12c) and some of them associated with BMS (pentlandite and chalcopyrite). In contrast, Moreno et al. (1999) observed that PGE-bearing sulfarsenides and arsenides of the Cabo Ortegal chromitites were located in the serpentinized silicate matrix, and interpreted them as secondary in origin (e.g., formed during serpentinization). But it could also be speculated that the occurrence of PGE-bearing sulfarsenides and arsenides in the studied chromitites (Fig. 12c and 15i-l) suggests direct crystallization of these PGM from the basaltic silicate melt before, or at the same time, to the segregation of the immiscible sulfide melt(s) (González-Jiménez et al., 2020 and references therein), as has been experimentally demonstrated (Helmy et al., 2013; Maier et al., 2015).

The experiments by Helmy et al. (2013) showed that Pt-As nano-associations form at high temperatures (950–1,180 °C) in both the sulfide melt and the crystallizing monosulfide solid solution (MSS). On the other hand, González-Jiménez et al., (2014a,2014b) suggested that crystallization of chromite in an open-system (dynamic) environment promote changes of T-fO_2-fS_2-a_{As} over short time spans. In this context, sudden changes of fS_2 and/or a_{As} as result of the influx of fluids/melt could destabilize PGM-alloys that crystallized earlier, promoting the formation of PGE-sulfides or PGE-sulfarsenides.

Liang et al. (2019) argued that euhedral shape and similar composition of PGE-bearing sulfarsenides and arsenides in BMS suggest a direct crystallization from the sulfide melt before crystallization of MSS and intermediate solid solution (ISS).

Additionally, the Pt-Pd sulfides (probably braggite-cooperite-vysotskyte series) observed in Type-I and Type-II chromitites (Fig. 12b, 13a; Appendix F: Figs. F.1, F.6) could suggest that they
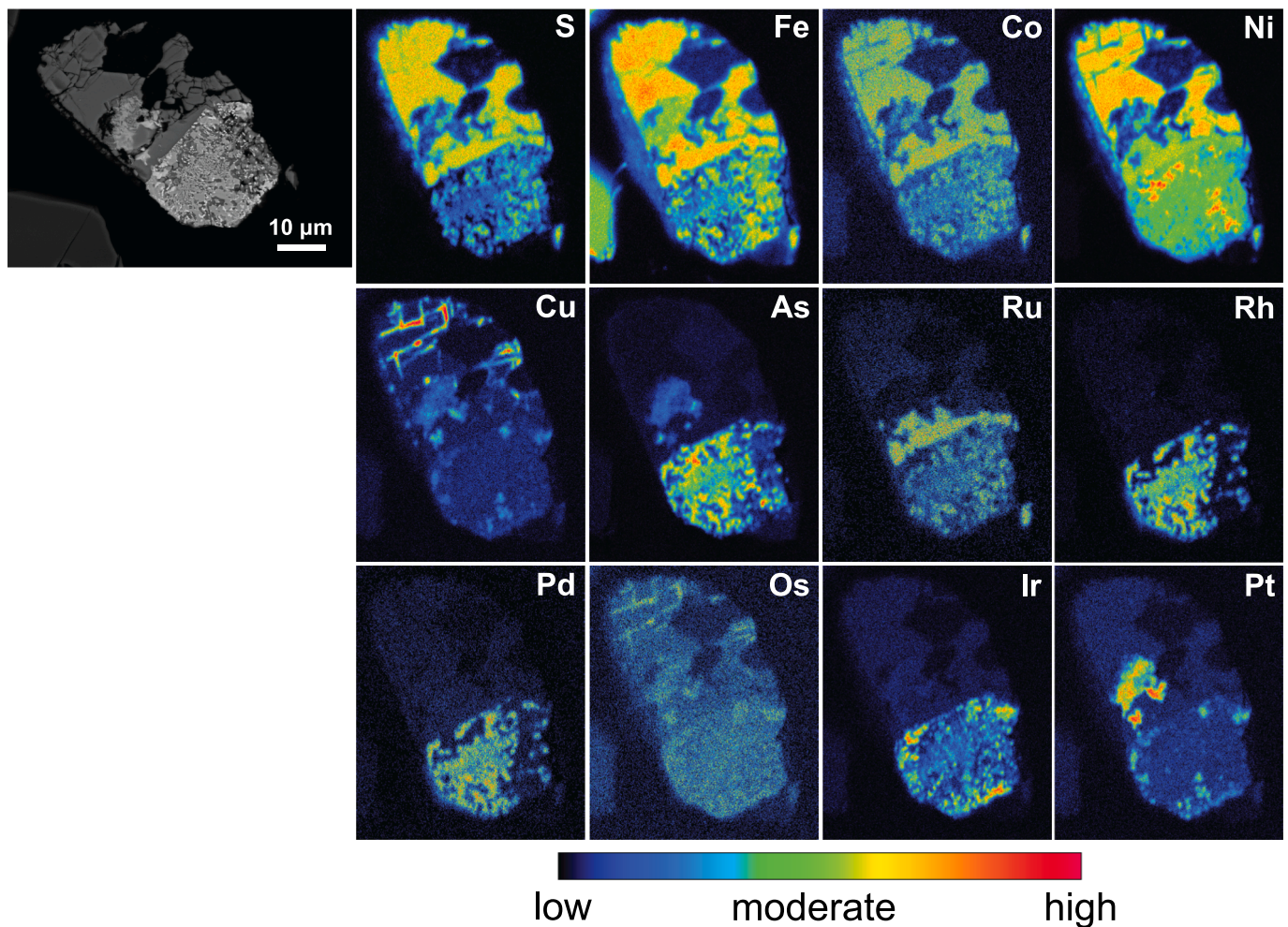
Fig. 17. Element distribution map of the free PGM of Fig. 14f from the Type-I chromitites of Cabo Ortegal.

crystallized at high temperatures directly from basaltic magmas in equilibrium with sulfide Ni-Fe-Cu melts or could represent exsolved products from BMS. Cooperite is stable at temperatures above 1,100 °C, while braggite and vysotskyte are stable below 1,100 °C and 1,000 °C, respectively (Verryn and Merkle, 2000) suggesting that some Pt-Pd sulfides in the studied chromitites could crystallized at magmatic conditions. However, discrete Pt-Pd sulfides as inclusions in Pt-Pd-Fe alloys in contact with Fe-oxides (probably as a result of desulfurization of Ni-Fe sulfides) at the edge of chromite (Fig. 12d) could suggest that the Pt-Pd sulfides were exsolved from BMS after crystallization (O'Driscoll and González-Jiménez, 2016). In this context, the Pt-Pd-Fe alloys could represent alteration products from desulfurization of Pt-Pd sulfides originally exsolved from BMS (Fig. 12d). Similar observations were made by Moreno et al. (1999), who interpreted that Pt-Pd sulfides associated with pentlandite and chalcopyrite, may have formed by exsolution from solid solution in BMS. Nevertheless, Moreno and co-authors, suggested that the origin of Pt-Pd sulfides not associated with BMS is uncertain and may represent alteration products of primary PGM. In view of all these observations, we suggest the possibility that some Pt-Pd sulfides could have crystallized under magmatic condition, as well as that some of them may represent exsolved products from BMS and/or alteration of primary PGM.

The observation of a grain with a composition close to iso-ferroplatinum (Fig. 15e and 16) may suggest crystallization from a sulfide melt. Isoferroplatinum and Pt-Pd sulfides (cooperite) can crystallize directly from a sulfide melt fraction (e.g., Genkin and Evstigneeva, 1986) at higher fS_2 and temperatures around

1,100–1,000 °C as demonstrated experimentally by Makovicky and Karup-Møller (2000) and Majzlan et al. (2002) for associations of Pt-rich alloys and Pt-Pd-Rh-Ir sulfides.

A dynamic environment promotes the immiscible segregation of sulfide melt(s), producing BMS associated with PGM, which could collect any PGE remaining in the melt (O'Driscoll and González-Jiménez, 2016). The occurrence of subrounded to polygonal-shaped composite grains of Ni-Fe (pentlandite), Cu-Fe (chalcopyrite/bornite?), and Ni sulfides (millerite/ heazlewoodite?) (Fig. 5d, 12 g; Appendix F: Figs. F.3, F.4, and F.5) could reflect the fractionation of high temperature sulfide melt and its subsequent sub-solidus reequilibration. These BMS could reflect the typical crystallization of MSS and ISS (intermediate solid solution) from sulfide melt(s) and later decomposition into pentlandite and pyrrhotite and chalcopyrite/bornite, respectively (e.g., Holwell and McDonald, 2010), or alternatively the decomposition of ISS and high temperature heazlewoodite solid solution (reacting with MSS), producing chalcopyrite and pentlandite, respectively (O'Driscoll and González-Jiménez, 2016 and references therein).

An ISS is the product of the recrystallization of a Cu-rich liquid at around 850 °C as it cools, which can recrystallize into Cu-Fe sulfides (chalcopyrite, bornite, and cubanite) while segregating a semi-metallic-rich melt (enriched in Te, Bi, As, and/or Sb) capable of forming PGM of Pt and Pd (Holwell and McDonald, 2010). Crystallization of this residual semi-metallic-rich melt forms discrete PGM around the margins of sulfide grains and could explain the occurrence of small Pt-Pd-bearing arsenides on the edges of Ni-Fe and Cu-Fe sulfides (pentlandite and chalcopyrite) (Fig. 12f; Appendix F: Fig. F.2), or the bismuthides (Pd-Pt-
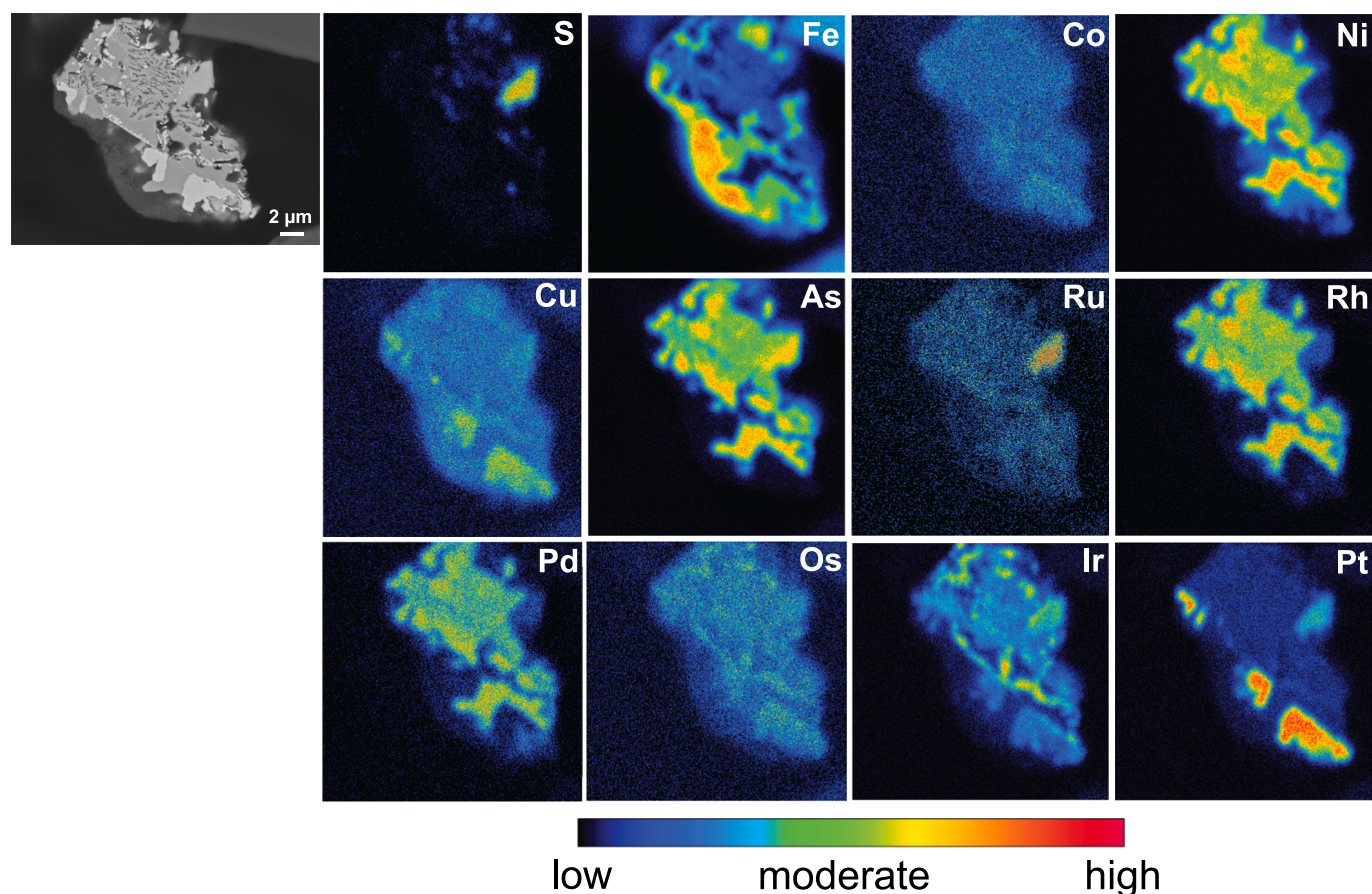
Fig. 18. Element distribution map of the free PGM of Fig. 15n from the Type-II chromitites of Cabo Ortegal.

Bi) and tellurides (Pd-Te-Bi) described by Moreno et al. (1999). Similar observations on the pyroxenites of the Herbeira massif by Tilhac et al. (2020), show that BMS (pyrrhotite, pentlandite, and chalcopyrite) with minor PGM (Pt-Pd-rich tellurides, bismuthides, and arsenides) occur in the interstitial matrix. These authors interpreted them to be exsolved products after crystallization of primary sulfides.

5.4.2. Secondary PGM and BMS assemblages

After crystallization in the magmatic stage PGM and PGM-bearing sulfides located at the edges of chromite and in the silicate matrix (Figs. 12 and 13) are more vulnerable to post-magmatic processes. As previously reported, the ultramafic rocks of the Herbeira massif have undergone retrograde amphibolite facies metamorphism (~8 kbar, 500 °C; Tilhac et al., 2016) related to the exhumation of the HP-HT rocks of the Capelada Unit, which may have triggered a local PGE redistribution, alteration of primary PGM, and formation of secondary PGM in the studied chromitites.

The observation of some Pt-Fe-Cu-(Ni) alloys with porous textures (Figs. 12e, 13b, 14d, and 15a-d, f) suggests that they were formed after the alteration of PGE-rich BMS or preexisting PGM. Strongly reducing conditions (e.g., serpentinization) promote the alteration (desulfurization) of magmatic (PGE-rich) BMS or PGM resulting in the formation of PGE- and/or base-metal- alloys (Cabri et al., 2022 and references therein). Porous grains with compositions between tetraferroplatinum and tulameenite (Fig. 15d, f and 16) suggest that they are formed by low-temperature alteration of primary PGM (O'Driscoll and González-Jiménez, 2016 and references therein). Moreover, the occurrence of discrete Pt-Fe alloys on the edge of Ni-Fe sulfides (Fig. 12a) could suggest that they are products of alteration of pentlandite (e.g., Prichard et al., 2008) or formed by the replacement of Pt-Pd sulfides during desulfurization processes with sulfide-undersaturated metamorphic

fluids (Li and Ripley, 2006). Their location at the edge of chromite crystals or interstitial silicate matrix favored interaction with metamorphic fluids, whereas porous textures (Fig. 15a-d, f) suggest the accumulation of small nanoparticles of Pt, Fe, Cu, and Ni precipitated from metamorphic fluids (Farré-de-Pablo et al., 2022).

Our HRTEM observations regarding the intergrowths of Pt-Ni-Fe and Fe-Cu-Ru-Os-Ir with Rh-Ni-As (interpreted as zaccariniite) (Fig. 15m, 19, and 20), reveal that these intergrowths are formed by aggregates of polycrystalline particles of nanometric size (i.e. nanoparticles) (Fig. 20a). In this context, minerals can exist in various nanostructures such as nanofilms, nanorods, or nanoparticles, depending on whether one, two, or three dimensions are reduced to the nanoscale, respectively. They are considered mineral nanoparticles when they coexist in larger (micrometer-scale) sizes and are termed nanominerals when they exclusively exist within the nanometric size range (González-Jiménez and Reich, 2017). Jiménez-Franco et al. (2020) noted that hydrous fluids caused the desulfurization of laurite, releasing minute particles of Ru-Os-Ir alloys < 50 nm in diameter. Jiménez-Franco and coauthors based their observations on an intergrowth of nano-sized (<5 nm) laurite with Ru-Os-Ir-(S-As) and Ru-Os-Ir alloys (5–10 nm) within a Fe-Mn oxide/hydroxide matrix. They suggested that these nanoparticles are the products of the desulfurization process of magmatic laurite, which decomposed into smaller laurite nanoparticles. These smaller particles then underwent a progressive transformation into Ru-Os-Ir-(S-As) particles and, eventually, into Ru-Os-Ir nanoalloys. The reorganization (coarsening) of the desulfurizing laurite within a matrix transforming to Fe-Mn oxide/hydroxide resulted in the formation of nanoscale intergrowths of Ru-Os-Ir-(S-As) particles and Ru-Os-Ir alloys with Fe-Mn oxide/hydroxide (Jiménez-Franco et al., 2020). According to this, it could be speculated that the observed intergrowths of Pt-Ni-Fe and Fe-Cu-Ru-Os-Ir alloys with Rh-Ni-As in the Cabo Ortegal chromitites were
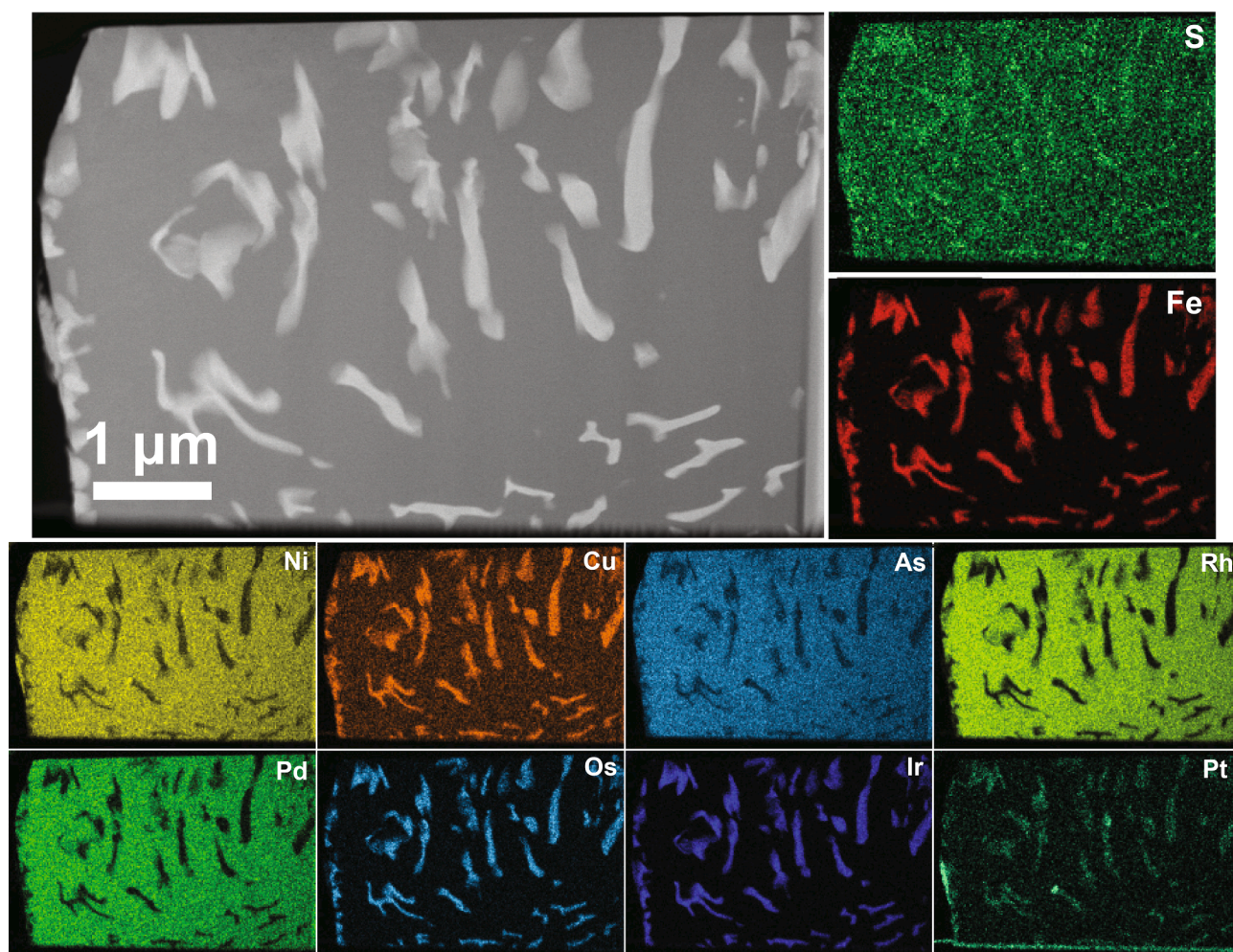
Fig. 19. Scanning transmission electron microscopy (STEM) image of the whole thin-foil obtained from the PGM of Fig. 15m and corresponding TEM-EDS elemental mapping.

formed by desulfurization of primary PGM by metamorphic fluids that released PGE-nanoparticles and base-metal alloys, thus allowing the reorganization and accumulation of these nanoparticles into complex intergrowths.

Zaccariniite is usually interpreted as a secondary mineral formed during post-magmatic processes (e.g., serpentinization; Vymazalova et al., 2012). Observations that Pt-Ir-Rh-As-S occur with zaccariniite and complex intergrowths of PGE-base metal alloys (Fig. 15n and 18) could suggest that zaccariniite and PGE-base metal alloys represent the products of desulfurization of Pt-Ir-Rh-As-S PGM. According to Farré-de-Pablo et al. (2022), the loss of S of primary PGM is compensated by the incorporation of Fe, Ni, Cu (Mn) from metamorphic fluids. In this context, desulfurization of PGM of Pt-Ir-Rh-As-S and addition of PGE and base-metals (i.e. Ni and Fe) by metamorphic fluids could have triggered the formation of zaccariniite and PGE alloys in the studied chromitites.

Summarizing, we propose that the Cabo Ortegal chromitites crystallized from volatile-rich small-volume melts that concentrate S, Pt, and Pd and favored the segregation of immiscible sulfide melt(s) after chromite crystallization, producing further concentration of PGE (especially Pt and Pd). The PGM assemblage in Type-I and Type-II chromitites suggests that the origin of the PGM is a combination of direct crystallization from silicate/sulfide melt, followed by the fractionation of sulfide melt, and subsequent sub-solidus reequilibration. Post-magmatic processes related to the percolation of hydrated metamorphic fluids responsible for retrograde metamorphism at amphibolite facies (e.g., exhumation of the HP-HT rocks of the Capelada Unit; Tilhac

et al., 2016 and references therein) would promote local remobilization of PGE, which gave place to the alteration of primary PGM and formation of secondary PGM. This is recorded by the negative slope between Pt and Pd and high Pt/Pd ratios in chromitites, dunites, and pyroxenites of the Herbeira massif (Fig. 11; Appendix D). Pd has a greater tendency to be mobilized by metamorphic fluids rather than Pt as experimentally demonstrated by Wood et al. (1992) and Evstigneeva and Tarkian (1996). This suggests that high Pt/Pd ratios and negative slope between Pt and Pd in chromitites and associated host rocks would result from remobilization of Pd by metamorphic fluids leaving residual Pt. It should also be noted that similar PGM assemblages and their textural location were described by Bridges et al. (1993) in the PGE-rich chromitites (up to 11,200 ppb) from the Bragança Massif in northern Portugal. It is thus possible that the same process that led to PGE enrichment and the formation of a PGM assemblage in the Cabo Ortegal chromitites took place in the relatively close Bragança chromitites.

5.5. Geodynamic setting and tectonic implications

Moreno et al. (2001) interpreted the ultramafic rocks of the Herbeira massif as a stratiform pyroxenite-dunite association at the crust-mantle interface below an arc, originated from batches of Cr- and PGE- rich mantle-derived magmas to explain the formation of Pt-Pd-rich chromitites. Other authors proposed that partial melting of residual tectonites or sub-arc mantle caused by the addition of supercritical fluids/melts in a suprasubduction environment with accumulation of magma formed
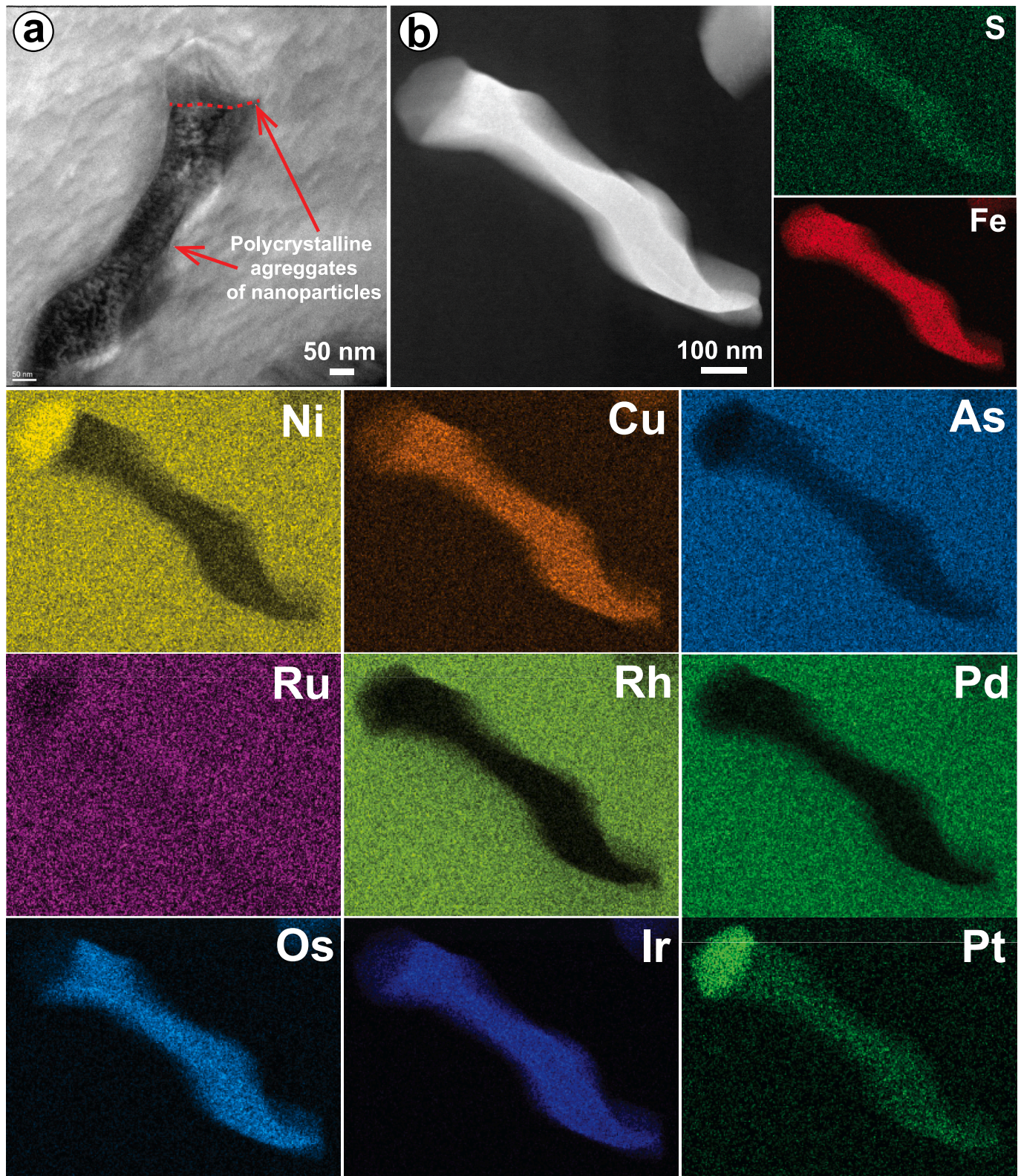
Fig. 20. A) high-magnification hrtem image of one intergrowth (see text for details), showing polycrystalline aggregates of nanoparticles. b) stem image of the same intergrowth and corresponding tem-eds elemental mapping.

pyroxenites and dunites from different parental liquids (Peucat et al., 1990; Girardeau and Gil Ibarguchi, 1991; Santos Zalduegui et al., 2002). More recently, Tilhac et al., (2016,2017,2020) suggested that the origin of the ultramafic rocks is related to the percolation and differentiation of Si-undersaturated picritic to boninitic melts in an old subcontinental lithospheric mantle beneath an arc.

Our calculated parental melt compositions suggests that Type-I chromitites crystallized from FAB-like melts, while Type-II chromitites crystallized from boninitic-like parental melts. These melts are characteristic of fore-arc regions affected by extension during subduction.
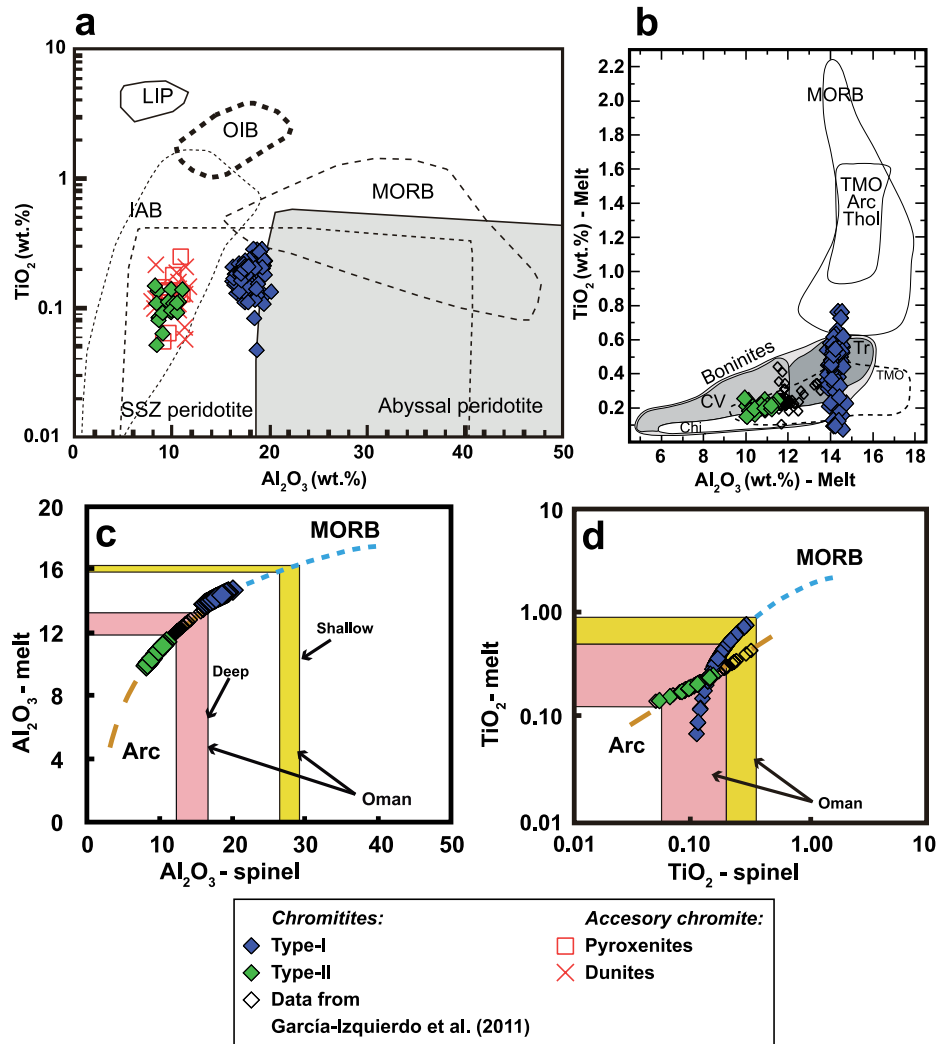
Fig. 21. A) chemical composition of chromite from chromitites, dunites, and pyroxenites of cabo ortegal complex in terms of tio₂ vs. Al₂O₃ compositions. For comparison, compositional fields of chromite from different geotectonic settings are shown. Data of compositional fields from Kamenetsky et al. (2001): LIP = large igneous province; OIB = ocean island basalt; IAB = island arc basalt; MORB = mid-ocean ridge basalt; SSZ = suprasubduction zone. b) TiO₂ and Al₂O₃ (wt. %) content of the melt calculated to be in equilibrium with chromite from the Cabo Ortegal chromitites compared to the fields for chromites from boninites and MORB sources (after Pagé and Barnes, 2009). Literature data of the Cabo Ortegal chromitites taken from García-Izquierdo et al. (2011) for comparison. c) and d) Al₂O₃ and TiO₂ contents of the melt in equilibrium with the Cabo Ortegal chromitites. Regression lines were obtained from Zaccarini et al. (2011) and are based on data from chromite-melt inclusions in MORB and arc lavas described by Kamenetsky et al. (2001) and Rollinson (2008). Literature data of the Cabo Ortegal chromitites taken from García-Izquierdo et al. (2011) for comparison. The deep and shallow fields correspond to the chromite and melt compositions of the Wadi Rajmi mantle chromitites in Oman (Rollinson, 2008) and are used for comparison.

Minor and trace elements contents in the unaltered chromite cores from both types of chromitites show patterns very similar to fore-arc chromitites (Fig. 10). In this context, we propose that the origin of these chromitites are the result of the percolation and differentiation of small-volume melts of FAB-like to boninitic melts in a sub-arc mantle environment. According to our model, the same boninitic melts reacted with peridotites to form the pyroxenites of the Herbeira massif. Thus, we suggest that the origin of the Cabo Ortegal chromitites and their PGE enrichment occurred during the developing of an arc of (at least) Cambrian-Ordovician age, as suggested by Tilhac et al. (2017) for the origin the Cabo Ortegal pyroxenites. Some authors have suggested that the terranes in north-western Iberia probably represent fragments of an ensialic island arc of Cambrian-Ordovician age (Andonaegui et al., 2002; Santos Zalduegui et al., 2002). Even though the age of this arc is controversial, a cluster of ages around 500 Ma has been reported in ultramafic rocks of Cabo Ortegal (Van Calsteren et al., 1979; Santos Zalduegui et al., 2002) and Sm-Nd whole-rock–clinopyroxene isochrons in pyroxenites have yielded Cambrian ages (ca. 500 Ma), interpreted as

the age of the magmatic-metasomatic protoliths (Santos Zalduegui et al., 2002; Tilhac et al., 2017).

5.6. Comparison with other ophiolitic chromitites involved in the European Variscan orogeny

Table 2 reports the occurrence of chromitite orebodies within ophiolitic complexes involved in the European Variscan orogeny. All these chromitites are related to suprasubduction zones, generated in fore-arc or back-arc environments. Most of these chromitite bodies show massive textures and variable sizes (from a few meters to 100′s meters long) and are hosted in dunites and harzburgites. Their Cr# is highly variable from 0.22 (Calzadilla de los Barros, Spain; Merinero et al., 2013) to 0.93 (Avren, Bulgaria; Colás et al., 2014; Colás, 2015). The following massifs host high-Cr chromitites: Bragança (Portugal; Cr# = 0.62–0.85; Bridges et al., 1995), Cabo Ortegal-Herbeira (Spain; Cr# = 0.60–0.82; this study), Kraubath and Hochgrössen (Austria; Cr# = 0.80–0.86 and 0.74–0.84, respectively; Malitch et al., 2003), and Avren

Table 2

Comparison with other ophiolitic chromitites involved in the European Variscan orogeny. Bragança (Portugal) data from Bridges (1992), Bridges et al., (1993,1995), and Mateus et al. (2016). Herbeira (Cabo Ortegal, Spain) data from Moreno et al., (1999,2001), Santos Zalduegui et al. (2002), Tilhac et al. (2017), and this study. Calzadilla de los Barros (Spain) data from Merinero et al., (2013,2014) and Arenas et al. (2018). Kraubath and Hochgrössen (Austria) data from Hiessleitner (1953), El Ageed (1979), Thalhammer et al. (1990), Malitch et al., (2001,2003), and Melcher and Meisel (2004). Ślęza (Poland) data from Birecki (1962), Kryza and Pin (2010), Delura (2012), Wojtulek et al., (2016,2019), and Awdankiewicz et al. (2021). Tisovita Iuti (Romania) data from Plissart et al. (2017). Dobromirtsi (Bulgaria) data from González-Jiménez et al., (2009, 2015a). Chernichevo (Bulgaria) data from Bonev et al. (2013), Colás et al. (2014), Colás (2015), and González-Jiménez et al. (2018). Golyamo Kamenyane (Bulgaria) data from Gervilla et al. (2012), Bonev et al. (2013), Colás et al. (2014), and Colás (2015). Avren and Yakovitsa (Bulgaria) data from Bonev et al. (2013), Colás et al. (2014), and Colás (2015).

Ophiolite	Country	Protolith age (Ma)	Orebody length	Chromitite host rock	Textures	Geodynamic setting	Cr#	$\sum$PGE(ppb) in chromitites	PGM
Bragança	Portugal	488 ± 10 495 ± 8 U-Pb (SHRIMP) Zircon grains from metagabbro and garnet-pyroxenite	–	Dunite	Disseminated Massive layers Schlieren	SSZ	0.62–0.85	24–11,200	Hollingworthite Platarsite (S-rich sperrylite) Pt-Pd-Cu alloys Pt-Fe-Cu alloys Pt-Ir alloys Atheneite (Pd, Hg, $Pt)_3As$ Froodite ($PdBi_2$) Potarite (PdHg) Sobolevskite (PdBi) Pd-Sn minerals Laurite
Herbeira (Cabo Ortegal)	Spain	~500 Sm-Nd whole-rock-clinopyroxene age from pyroxenites	Few meters	Dunite	Massive Semi-massive horizons Schlieren	SSZ (FA)	0.60–0.82	76–13,375	Pt-Pd sulfides (braggite-cooperite) Pt-Pd-Ni-S Irarsite Hollingworthite S-rich sperrylite (formerly platarsite) Sperrylite Tetraferroplatinum Pt-Fe-Ni-(Cu) alloys Zvyangintsevite (Pd_3Pb) RhNiAs (zaccariniite) Pd-Au-Hg Pd-Ni-S Pt-Rh-Ni-Cu-Fe Pt-Rh-Fe Pt-Cu Pt-Au-Cu Pt-Pd-Au Pd-Pt-As Pd-Pt-Bi Pd-Te-Bi Pd-Sb Potarite Laurite Os-Ru-Fe-Ni-S Pd-Pt oxides
Calzadilla de los Barros	Spain	Ediacaran c. 600 U-Pb (SHRIMP) Zircon grain from gabbroic rocks	6–8 m	Serpentinite	Semi-massive Massive Disseminated	SSZ	0.22–0.55	29–291	Laurite-erlichmanite
Kraubath (Speik complex)	Austria	554 ± 37 Sm-Nd Whole-rock age from pyroxenite and gabbro 550 ± 17 Re-Os isotope age from pyroxenites	–	Dunite Harzburgite	Schlieren Massive	SSZ	0.80–0.86	731–1,190	Bowieite (Rh_2S_3) Cuprorhodsite ($CuRh_2S_4$) Hollingworthite Rh_2S_3 Platarsite (S-rich sperrylite) Sperrylite Pt-Fe alloys Keithconnite ($Pd_{3-x}Te$) Mertierite II ($Pd_8(Sb, As)_3$) Potarite Stibiopalladinite (Pd_5Sb_2) Irarsite Pd_3Fe Laurite Erlichmanite

(continued on next page)

Table 2 (*continued*)

Ophiolite	Country	Protolith age (Ma)	Orebody length	Chromitite host rock	Textures	Geodynamic setting	Cr#	∑PGE(ppb) in chromitites	PGM
Hochgrössen (Speik complex)	Austria	554 ± 37 Sm-Nd Whole-rock age from pyroxenite and gabbro 550 ± 17 Re-Os isotope age from pyroxenites	–	Dunite Harzburgite	Schlieren Massive	SSZ	0.74–0.84	1,098–2,640	Mayakite (PdNiAs) PdRhAs Os-Ir alloys Os Laurite Os-Ir alloys Sperrylite S-rich sperrylite Irarsite-hollingworthite Pd-Pt-Sb Pt Erlichmanite Pt-Cu sulfarsenide Cooperite
Ślęża	Poland	400 ± 10 403 ± 6 U-Pb (SHRIMP) Zircon from metagabbroic and metavolcanic rocks	Up to 22 m	Serpentinite	Massive Laminated Nodular Disseminated Brecciated Veinlets	SSZ	0.50–0.69	42–79	–
Tisovita Iuti	Romania	409 ± 38 Sm-Nd Whole-rock isochron age from gabbroic rocks	–	Dunite	Massive Nodular Disseminated	SSZ (BAB)	0.39–0.48	–	–
Dobromirtsi (Central Rhodope massif)	Bulgaria	*	10's of m	Dunite	Massive Semi-massive Disseminated Nodular	SSZ (BAB)	0.55–0.74	60–1,537	Laurite Os-Ir alloys Irarsite-hollingworthite Os Pd-Sn-Cu Rh-Os-Sb
Chernichevo (Eastern Rhodope massif)	Bulgaria	*	Few 10's of m	Dunite Harzburgite	Massive Semi-massive	SSZ (BAB)	0.55	886–3,661	–
Golyamo Kamenyane (Eastern Rhodope massif)	Bulgaria	*	Few 100's of m	Dunite Harzburgite	Semi-massive Massive	SSZ (BAB)	0.52–0.60	–	–
Avren (Eastern Rhodope massif)	Bulgaria	*	Few 10's of m	Dunite Harzburgite	Massive Semi-massive Disseminated	SSZ (BAB)	0.84–0.93	–	–
Yakovitsa (Eastern Rhodope massif)	Bulgaria	*	Few 10's of m	Dunite Harzburgite	Massive Semi-massive Disseminated	SSZ (BAB)	0.60–0.83	–	–

*Undetermined age of the protolith.

and Yakobitsa (Bulgaria; Cr# = 0.84–0.93 and 0.60–0.83, respectively; Colás et al., 2014; Colás, 2015); whereas high-Al chromitites are found in Calzadilla de los Barros (Spain; Cr# = 0.22–0.55; Merinero et al., 2013, 2014), Ślęża (Poland; Cr# = 0.50–0.69; Wojtulek et al., 2016, 2019), Tisovita Iuti (Romania; Cr# = 0.39–0.48; Plissart et al., 2017), Dobromirtsi (Bulgaria; Cr# = 0.55–0.74; González-Jiménez et al., 2009, 2015a), and Chernichevo and Golyamo Kamenyane (Bulgaria; Cr# = 0.55 and 0.52–0.60, respectively; Colás et al., 2014; Colás, 2015; Gervilla et al., 2012).

The observed range of PGE content in Variscan ophiolitic chromitites is very large, from 24 ppb (Bragança; Bridges et al., 1993) to 13,375 ppb (Cabo Ortegal; Moreno et al., 2001). Interestingly, some of these chromitites have strongly variable PGE contents that can reach ppm levels, for example Bragança (up to 11,200 ppb; Bridges et al., 1993), Cabo Ortegal (up to 13,375 ppb; Moreno et al., 1999, 2001 and this study), Kraubath and Hochgrössen (731–1,190 ppb and 1,098–2,640 ppb, respectively; Malitch et al., 2001, 2003), Dobromirtsi (60–1,537 ppb; González-Jiménez et al., 2015a), and Chernichevo (886–3,661 ppb; González-Jiménez et al., 2018). Nevertheless, the most PGE-rich

chromitites are those from Cabo Ortegal (76–13,375 ppb; Moreno et al., 1999, 2001; this study) and Bragança (24–11,200 ppb; Bridges et al., 1993), both massifs with similar PGE contents. It should be noted that both ophiolitic chromitites are located in the Variscan Iberian massif (Bridges et al., 1993; Moreno et al., 1999, 2001 and references therein). In addition, they show a clear PPGE enrichment over IPGE (Cabo Ortegal: Moreno et al., 1999, 2001 and the present study; Bragança: Bridges et al., 1993). This is also reflected in the PGM mineralogy, both massifs show a similar PGM assemblage with abundance of Rh-Pt-Pd-rich PGM, which include sperrylite (and S-rich variety), Pt-Fe (Pd-Cu) alloys, hollingworthite, and potarite (PdHg) (Table 2). Furthermore, the Kraubath chromitites also exhibit PPGE enrichment (Malitch et al., 2001, 2003) and display similar PGM assemblages when compared with those from Cabo Ortegal and Bragança chromitites (Table 2). Notably, the Kraubath chromitites also have similar Cr# with Cabo Ortegal and Bragança chromitites.

The ages for the protoliths of the ophiolitic massifs involved in the European Variscan Orogen ranges between Proterozoic to Devonian (Table 2). However, the age of protoliths for the ophiolites of the Central

and Eastern Rhodopes (Dobromirtsi, Chernichevo, Golyamo Kamenyane, Avren, and Yakovitsa) remains undetermined. Indeed, the protoliths of these metamorphosed mafic–ultramafic rocks have been considered to be Precambrian, Paleozoic or even Mesozoic (see Colás, 2015; González-Jiménez et al., 2015a and references therein). Interestingly, the ophiolite bodies of the Iberian massif, Herbeira (Cabo Ortegal) and Bragança have similar protolith ages of ca. ~ 500 Ma (Santos Zalduegui et al., 2002; Tilhac et al., 2017) and 495–488 Ma (Mateus et al., 2016), respectively. The mafic–ultramafic rocks of Bragança are equivalent to those from the Herbeira massif of Cabo Ortegal (Santos Zalduegui et al., 2002 and references therein) and have also been linked to the development of a Cambrian-Ordovician arc (Andonaegui et al., 2002; Santos Zalduegui et al., 2002).

In terms of their geodynamic setting, host rocks, textures, PGE contents, PGM assemblage, and Cr#, the studied Cabo Ortegal chromitites are similar to other Variscan chromitites, particularly those documented in the Bragança massif in northern Portugal and those in the Kraubath massif in Austria.

6. Concluding remarks

We interpret that the studied chromitites of the Cabo Ortegal Complex formed in a sub-arc mantle environment probably in a fore-arc region. Besides, we interpret that Type-I chromitites crystallized from FAB-like melts in an early stage and Type-II chromitites from boninitic melts in the ensuing stage. The studied chromitites are enriched in PGE, showing PPGE enrichment with respect to IPGE. Observations that PGM associated with BMS are systematically located at the edges of chromite and in the silicate matrix of the chromitites suggest that the origin of the PGE enrichment is related to S-As rich melt(s) that collected base-metals and incompatible PGE. These melts were segregated by immiscibility from volatile-rich small volume melts. The PGM assemblage observed in the studied chromitites reflects the direct crystallization from silicate/sulfide melt(s), followed by fractionation of sulfide melt(s) and subsequent subsolidus reequilibration. The origin of these chromitites together with their PGE enrichment is linked to the developing of an arc of at least Cambrian-Ordovician age.

Post-magmatic processes related to the percolation of hydrated fluids during retrograde amphibolite metamorphism (~8 kbar, 500 °C) during the exhumation at c. 380 Ma of the HP-HT rocks of the Capelada Unit affected dunites, pyroxenites, and chromitites of the Herbeira massif. This led to local remobilization of PGE, promoting alteration of primary PGM and formation of secondary PGM, but preserving the magmatic composition of the chromite cores in the chromitites.

Finally, the studied Cabo Ortegal chromitites in terms of their geodynamic setting, host rocks, textures, PGE contents, PGM assemblage, and Cr# are similar to the Variscan chromitites documented in the Bragança (northern Portugal) and Kraubath (Styria, Austria) ophiolitic massifs.

Declaration of competing interest

The authors declare that they have no known competing financial interests or personal relationships that could have appeared to influence the work reported in this paper.

Data availability

Data will be made available on request.

Acknowledgments

Appendix A. Supplementary data

Supplementary data to this article can be found online at https://doi.org/10.1016/j.oregeorev.2024.106109.

References

Abati, J., Castiñeiras, P., Arenas, R., Fernández-Suárez, J., Gómez Barreiro, J., Wooden, J.L., 2007. Using SHRIMP zircon dating to unravel tectonothermal events in arc environments. The early Palaeozoic arc of NW Iberia revisited. Terra Nova 19, 432–439. https://doi.org/10.1111/j.1365-3121.2007.00768.x.

Albert, R., Arenas, R., Sánchez-Martínez, S., Gerdes, A., 2013. The eclogite facies gneisses of the Cabo Ortegal Complex (NW Iberian Massif): Tectonothermal evolution and exhumation model. J. Iber. Geol. 38, 389–406. https://doi.org/10.5209/rev_JIGE.2012.v38.n2.40465.

Albert, R., Arenas, R., Gerdes, A., Sánchez Martínez, S., Fernández-Suárez, J., Fuenlabrada, J.M., 2015. Provenance of the Variscan Upper Allochthon (Cabo Ortegal Complex, NW Iberian Massif). Gondw. Res. 28, 1434–1448. https://doi.org/10.1016/j.gr.2014.10.016.

Andonaegui, P., González del Tánago, J., Arenas, R., Abati, J., Martínez Catalán, J.R., Peinado, M., Díaz García, F., 2002. Tectonic setting of the Monte Castelo gabbro (Ordenes Complex, northwestern Iberian Massif): Evidence for an arc-related terrane in the hanging wall to the Variscan suture, in: Variscan-Appalachian Dynamics: The Building of the Late Paleozoic Basement. Geol. Soc. Am. Doi: 10.1130/0-8137-2364-7.37.

Arenas, R., Gil Ibarguchi, J.I., González Lodeiro, F., Klein, E., Martínez Catalán, J.R., Ortega Gironés, E., de Pablo Maciá, J.G., Peinado, M., 1986. Tectonostratigraphic units in the complexes with mafic and related rocks of the NW of the Iberian Massif. Hercynica 2, 87–110.

Arenas, R., Sánchez Martínez, S., Castiñeiras, P., Jeffries, T.E., Díez Fernández, R., Andonaegui, P., 2009. The basal tectonic mélange of the Cabo Ortegal Complex (NW Iberian Massif): a key unit in the suture of Pangea. J. Iber. Geol. 35, 85–125.

Arenas, R., Sánchez Martínez, S., Gerdes, A., Albert, R., Díez Fernández, R., Andonaegui, P., 2014. Re-interpreting the Devonian ophiolites involved in the Variscan suture: U-Pb and Lu–Hf zircon data of the Moeche Ophiolite (Cabo Ortegal Complex, NW Iberia). Int J Earth Sci (geol Rundsch) 103, 1385–1402. https://doi.org/10.1007/s00531-013-0880-x.

Arenas, R., Sánchez Martínez, S., Díez Fernández, R., Gerdes, A., Abati, J., Fernández-Suárez, J., Andonaegui, P., González Cuadra, P., López Carmona, A., Albert, R., Fuenlabrada, J.M., Rubio Pascual, F.J., 2016. Allochthonous terranes involved in the Variscan suture of NW Iberia: A review of their origin and tectonothermal evolution. Earth Sci. Rev. 161, 140–178. https://doi.org/10.1016/j.earscirev.2016.08.010.

Arenas, R., Fernández-Suárez, J., Montero, P., Díez Fernández, R., Andonaegui, P., Sánchez Martínez, S., Albert, R., Fuenlabrada, J.M., Matas, J., Martín Parra, L.M., Rubio Pascual, F.J., Jiménez-Díaz, A., Pereira, M.F., 2018. The Calzadilla Ophiolite (SW Iberia) and the Ediacaran fore-arc evolution of the African margin of Gondwana. Gondw. Res. 58, 71–86. https://doi.org/10.1016/j.gr.2018.01.015.

Arenas, R., 1988. Evolución petrológica y geoquímica de la Unidad Alóctona inferior del complejo metamórfico básico-ultrabásico de Cabo Ortegal (Unidad de Moeche) y del silúrico paraautóctono, Cadena Hercínica Ibérica (NW de España), Corpus geologicum Gallaeciae. Fundación "Pedro Barrie de la Maza, Conde de Fenosa," La Coruña.

Augé, T., 1987. Chromite deposits in the northern Oman ophiolite: Mineralogical constraints. Mineral. Deposita 22, 1–10. https://doi.org/10.1007/BF00204235.

Awdankiewicz, M., Kryza, R., Turniak, K., Ovtcharova, M., Schaltegger, U., 2021. The Central Sudetic Ophiolite (European Variscan Belt): precise U-Pb zircon dating and geotectonic implications. Geol. Mag. 158, 555–566. https://doi.org/10.1017/S0016756820000722.

Barnes, S.-J., Naldrett, A.J., Gorton, M.P., 1985. The origin of the fractionation of platinum-group elements in terrestrial magmas. Chem. Geol. 53, 303–323.

Beranoaguirre, A., Puelles, P., Ábalos, B., Gil Ibarguchi, J.I., García de Madinabeitia, S., 2019. Short-duration regional metamorphic event recorded in a Variscan subduction channel (Malpica–Tui eclogites, NW Iberia). Int J Earth Sci (geol Rundsch) 108, 2037–2046. https://doi.org/10.1007/s00531-019-01747-1.

Beranoaguirre, A., García de Madinabeitia, S., Sanchez Lorda, M.E., Puelles, P., Ábalos, B., Gil Ibarguchi, J.I., 2020. U-Pb, Hf isotope and REE constraints on high-pressure acid migmatites from the Cabo Ortegal Complex (NW Spain): New evidence of short-duration metamorphism in a Variscan subduction channel. Lithos 372–373, 105660. https://doi.org/10.1016/j.lithos.2020.105660.

Beranoaguirre, A., Ábalos, B., García de Madinabeitia, S., Paquette, J.-L., Pin, C., Sánchez Lorda, M.E., Santos Zalduegui, J.F., Puelles, P., Gil Ibarguchi, J.I., 2022. Geochronological record of Cadomian exterior orogen reworking in bi-modal igneous protoliths of the Cabo Ortegal Allochthon (NW Iberia): the Cambrian onset of the Palaeozoic plate-tectonic cycle. Int. Geol. Rev. 1–26 https://doi.org/10.1080/00206814.2022.2089923.

Bhat, I.M., Ahmad, T., Rao, D.V.S., Balakrishnan, S., Rao, N.V.C., 2021. PGE and isotopic characteristics of Shergol and Suru Valley Ophiolites, Western Ladakh: Implications for supra-subduction tectonics along Indus Suture Zone. Geosci. Front. 12, 101118 https://doi.org/10.1016/j.gsf.2020.11.014.

Birecki, T., 1962. Occurrence of chromites at Tąpadła (in Polish with English summary). Przegląd Geologiczny 10, 144–150.

Bonavia, F.F., Diella, V., Ferrario, A., 1993. Precambrian podiform chromitites from Kenticha Hill, southern Ethiopia. Econ. Geol. 88, 198–202. https://doi.org/10.2113/gsecongeo.88.1.198.

Bonev, N., Ovtcharova-Schaltegger, M., Moritz, R., Marchev, P., Ulianov, A., 2013. Peri-Gondwanan Ordovician crustal fragments in the high-grade basement of the Eastern Rhodope Massif, Bulgaria: evidence from U-Pb LA-ICP-MS zircon geochronology and geochemistry. Geodin. Acta 26, 207–229. https://doi.org/10.1080/09853111.2013.858942.

Bridges, J.C., 1992. Platinum-group elements in the ultrabasic rocks of the Bragança massif, northern Portugal. The Open University, Milton Keynes. Ph.D. thesis.

Bridges, J.C., Prichard, H.M., Neary, C.R., Meireles, C.A., 1993. Platinum-group element mineralization in the chromite-rich rocks of Bragança massif, northern Portugal. Applied Earth Science IMM Transactions Section B 102, B103–B113.

Bridges, J.C., Prichard, H.M., Meireles, C.A., 1995. Podiform chromitite-bearing ultrabasic rocks from the Bragança Massif, northern Portugal: fragments of island arc mantle? Geol. Mag. 132, 39–49. https://doi.org/10.1017/S0016756800011419.

Cabri, L.J., Oberthür, T., Keays, R.R., 2022. Origin and depositional history of platinum-group minerals in placers – A critical review of facts and fiction. Ore Geol. Rev. 144, 104733 https://doi.org/10.1016/j.oregeorev.2022.104733.

Cabri, L., Rudashevsky, V., Lastra, R., 2006. Hydroseparation: a new development in process mineralogy of platinum-bearing ores. Canad. Institute Min. Metallur. Petrol. Bulletin 99, 1–7.

Chan, T.K., Finch, I.J., 2001. Determination of platinum-group elements and gold by inductively coupled plasma mass spectrometry, in: Australian Platinum Conference. Presented at the Australian Platinum Conference, Perth, Western Australia, pp. 1–9.

Colás, V., 2015. Modelos de alteración de cromititas ofiolíticas durante el metamorfismo (Ph.D. thesis). Universidad de Zaragoza.

Colás, V., González-Jiménez, J.M., Griffin, W.L., Fanlo, I., Gervilla, F., O'Reilly, S.Y., Pearson, N.J., Kerestedjian, T., Proenza, J.A., 2014. Fingerprints of metamorphism in chromite: New insights from minor and trace elements. Chem. Geol. 389, 137–152. https://doi.org/10.1016/j.chemgeo.2014.10.001.

Colás, V., Padrón-Navarta, J.A., González-Jiménez, J.M., Fanlo, I., López Sánchez-Vizcaíno, V., Gervilla, F., Castroviejo, R., 2017. The role of silica in the hydrous metamorphism of chromite. Ore Geol. Rev. 90, 274–286. https://doi.org/10.1016/j.oregeorev.2017.02.025.

Colás, V., González-Jiménez, J.M., Camprubí, A., Proenza, J.A., Griffin, W.L., Fanlo, I., O'Reilly, S.Y., Gervilla, F., González-Partida, E., 2019. A reappraisal of the metamorphic history of the Tehuitzingo chromitite, Puebla state, Mexico. Int. Geol. Rev. 61, 1706–1727. https://doi.org/10.1080/00206814.2018.1542633.

Colás, V., Subías, I., González-Jiménez, J.M., Proenza, J.A., Fanlo, I., Camprubí, A., Griffin, W.L., Gervilla, F., O'Reilly, S.Y., Escayola, M.F., 2020. Metamorphic fingerprints of Fe-rich chromitites from the Eastern Pampean Ranges. Argentina. BSGM 72, A080420. https://doi.org/10.18268/BSGM2020v72n3a080420.

Delura, K., 2012. Chromitites from the Sudetic ophiolite: origin and alteration. Archivum Mineral. Monograph 4, 1–91. https://doi.org/10.31338/uw.9788323521952.

Díez Fernández, R., Arenas, R., 2015. The Late Devonian Variscan suture of the Iberian Massif: A correlation of high-pressure belts in NW and SW Iberia. Tectonophysics 654, 96–100. https://doi.org/10.1016/j.tecto.2015.05.001.

Díez Fernández, R., Arenas, R., Pereira, M.F., Sánchez Martínez, S., Albert, R., Martín Parra, L.-M., Rubio Pascual, F.J., Matas, J., 2016. Tectonic evolution of Variscan Iberia: Gondwana-Laurussia collision revisited. Earth Sci. Rev. 162, 269–292. https://doi.org/10.1016/j.earscirev.2016.08.002.

Díez Fernández, R., Arenas, R., Sánchez Martínez, S., Novo-Fernández, I., Albert, R., 2020. Single subduction zone for the generation of Devonian ophiolites and high-P metamorphic belts of the Variscan Orogen (NW Iberia). Terra Nova 32, 239–245. https://doi.org/10.1111/ter.12455.

Dönmez, C., Keskin, S., Günay, K., Çolakoğlu, A.O., Çiftçi, Y., Uysal, İ., Türkel, A., Yıldırım, N., 2014. Chromite and PGE geochemistry of the Elekdağ Ophiolite (Kastamonu, Northern Turkey): Implications for deep magmatic processes in a supra-subduction zone setting. Ore Geol. Rev. 57, 216–228. https://doi.org/10.1016/j.oregeorev.2013.09.019.

El Ageed, A.I., 1979. The Hochgrößen Ultramafic-mafic Association, its associated mineralization and petrogenetic significance (Ph.D. thesis). Universitäat Köln.

Evans, B.W., Frost, B.R., 1975. Chrome-spinel in progressive metamorphism—a preliminary analysis. Geochim. Cosmochim. Acta 39, 959–972. https://doi.org/10.1016/0016-7037(75)90041-1.

Evstigneeva, T., Tarkian, M., 1996. Synthesis of platinum-group minerals under hydrothermal conditions. Eur. J. Mineral. 549–564.

Farré-de-Pablo, J., Proenza, J.A., González-Jiménez, J.M., Aiglsperger, T., Garcia-Casco, A., Escuder-Viruete, J., Colás, V., Longo, F., 2020. Ophiolite hosted chromitite formed by supra-subduction zone peridotite –plume interaction. Geosci. Front. 11, 2083–2102. https://doi.org/10.1016/j.gsf.2020.05.005.

Farré-de-Pablo, J., Proenza, J.A., González-Jiménez, J.M., Aiglsperger, T., Torró, L., Domènech, C., Garcia-Casco, A., 2022. Low-temperature hydrothermal Pt mineralization in uvarovite-bearing ophiolitic chromitites from the Dominican Republic. Miner. Deposita 57, 955–976. https://doi.org/10.1007/s00126-021-01079-8.

Fernández-Suárez, J., Corfu, F., Arenas, R., Marcos, A., Martínez Catalán, J., Díaz García, F., Abati, J., Fernández, F.J., 2002. U-Pb evidence for a polyorogenic evolution of the HP-HT units of the NW Iberian Massif. Contrib. Miner. Petrol. 143, 236–253. https://doi.org/10.1007/s00410-001-0337-2.

Fernández-Suárez, J., Arenas, R., Abati, J., Martínez Catalán, J.R., Whitehouse, M.J., Jeffries, T.E., 2007. U-Pb chronometry of polymetamorphic high-pressure granulites: An example from the allochthonous terranes of the NW Iberian Variscan belt, in: Geological Society of America Memoirs. Geological Society of America, pp. 469–488. Doi: 10.1130/2007.1200(24).

Fleet, M.E., Wu, T.-W., 1995. Volatile transport of precious metals at 1000°C: Speciation, fractionation, and effect of base-metal sulfide. Geochim. Cosmochim. Acta 59, 487–495. https://doi.org/10.1016/0016-7037(94)00382-V.

Franke, W., 1989. Tectonostratigraphic units in the Variscan belt of central Europe, in: Dallmeyer, R.D. (Ed.), Terranes in the Circum-Atlantic Paleozoic Orogens. Geological Society of America, p. 0. Doi: 10.1130/SPE230-p67.

Freitas Suita, M.T.D., Strieder, A.J., 1996. Cr-Spinels from Brazilian Mafic-Ultramafic Complexes: Metamorphic Modifications. Int. Geol. Rev. 38, 245–267. https://doi.org/10.1080/00206819709465333.

Gale, A., Dalton, C.A., Langmuir, C.H., Su, Y., Schilling, J.-G., 2013. The mean composition of ocean ridge basalts. Geochem. Geophys. Geosyst. 14, 489–518. https://doi.org/10.1029/2012GC004334.

García-Izquierdo, B., Capote del Villar, R., Lunar, R., Monterrubio, S., Instituto Universitario de Geología, Universidad de Coruña, Seminario de Estudos Galegos, Área de Xeoloxía e Minería, 2011. Evolución geodinámica y procesos mantélicos en el Macizo de Herbeira, Complejo de Cabo Ortegal (NO de la Península Ibérica). Instituto Universitario de Geología "Isidro Parga Pondal", Área de Xeoloxía e Minería do Seminario de Estudos Galegos, A Coruña.

Garuti, G., Pushkarev, E.V., Zaccarini, F., Cabella, R., Anikina, E., 2003. Chromite composition and platinum-group mineral assemblage in the Uktus Uralian-Alaskan-type complex (Central Urals, Russia). Miner. Deposita 38, 312–326.

Garuti, G., Pushkarev, E.V., Zaccarini, F., 2005. Diversity of chromite-PGE mineralization in ultramafic complexes of the Urals. In: Törmänen, T.O., Alapieti, T.T. (Eds.), Platinum-Group-Elements-from Genesis to Beneficiation and Environmental Impact. Tenth Int. Platinum Symp, Oulu, pp. 341–344.

Genkin, A.D., Evstigneeva, T.L., 1986. Associations of platinum-group minerals of the Noril'sk copper-nickel sulfide ores. Econ. Geol. 81, 1203–1212. https://doi.org/10.2113/gsecongeo.81.5.1203.

Gervilla, F., Proenza, J.A., Frei, R., González-Jiménez, J.M., Garrido, C.J., Melgarejo, J.C., Meibom, A., Díaz-Martínez, R., Lavaut, W., 2005. Distribution of platinum-group elements and Os isotopes in chromite ores from Mayarí-Baracoa Ophiolitic Belt (eastern Cuba). Contrib. Miner. Petrol. 150, 589–607. https://doi.org/10.1007/s00410-005-0039-2.

Gervilla, F., Padrón-Navarta, J.A., Kerestedjian, T., Sergeeva, I., González-Jiménez, J.M., Fanlo, I., 2012. Formation of ferrian chromite in podiform chromitites from the Golyamo Kamenyane serpentinite, Eastern Rhodopes, SE Bulgaria: A two-stage process. Contrib. Miner. Petrol. 164, 643–657. https://doi.org/10.1007/s00410-012-0763-3.

Gil Ibarguchi, J.I., Abalos, B., Azcarraga, J., Puelles, P., 1999. Deformation, high-pressure metamorphism and exhumation of ultramafic rocks in a deep subduction/collision setting (Cabo Ortegal, NW Spain). J. Metam. Geol. 17, 747–764. https://doi.org/10.1046/j.1525-1314.1999.00227.x.

Girardeau, J., Gil Ibarguchi, J.I., 1991. Pyroxenite-Rich Peridotites of the Cabo Ortegal Complex (Northwestern Spain): Evidence for Large-Scale Upper-Mantle Heterogeneity. J. Petrol. Special_volume 135–154. https://doi.org/10.1093/petrology/Special_Volume.2.135.

Girardeau, J., Gil Ibarguchi, J.I., Ben Jamaa, N., 1989. Evidence for a Heterogeneous Upper Mantle in the Cabo Ortegal Complex, Spain. Science 245, 1231–1233. https://doi.org/10.1126/science.245.4923.1231.

González-Jiménez, J.M., Auge, T., Gervilla, F., Bailly, L., Proenza, J.A., Griffin, W.L., 2011. Mineralogy and geochemistry of platinum-rich chromitites from the mantle-crust transition zone at Ouen Island, New Caledonia Ophiolite. Can. Mineral. 49, 1549–1569. https://doi.org/10.3749/canmin.49.6.1549.

González-Jiménez, J.M., Camprubí, A., Colás, V., Griffin, W.L., Proenza, J.A., O'Reilly, S.Y., Centeno-García, E., García-Casco, A., Belousova, E., Talavera, C., Farré-de-Pablo, J., Satsukawa, T., 2017a. The recycling of chromitites in ophiolites from southwestern North America. Lithos 294–295, 53–72. https://doi.org/10.1016/j.lithos.2017.09.020.

González-Jiménez, J.M., Colás, V., Gervilla, F., Kerestedjian, T.N., Sergeeva, I., Casado-González, A., Fanlo, I., 2018. Metamorphic evolution of sulphide-rich chromitites from the Chernichevo ultramafic massif, SE Bulgaria. Ore Geol. Rev. 101, 330–348. https://doi.org/10.1016/j.oregeorev.2018.07.024.

González-Jiménez, J.M., Kerestedjian, T., Proenza Fernández, J.A., Gervilla Linares, F., 2009. Metamorphism on chromite ores from the Dobromirtsi ultramafic massif, Rhodope mountains (SE Bulgaria). Geologica Acta, 2009, vol. 7, núm. 4, p. 413-429.

González-Jiménez, J.M., Griffin, W.L., Gervilla, F., Proenza, J.A., O'Reilly, S.Y., Pearson, N.J., 2014a. Chromitites in ophiolites: How, where, when, why? Part I. A review and new ideas on the origin and significance of platinum-group minerals. Lithos 189, 127–139. https://doi.org/10.1016/j.lithos.2013.06.016.

González-Jiménez, J.M., Griffin, W.L., Proenza, J.A., Gervilla, F., O'Reilly, S.Y., Akbulut, M., Pearson, N.J., Arai, S., 2014b. Chromitites in ophiolites: how, where, when, why? Part II. The Crystallization of Chromitites. Lithos 189, 140–158. https://doi.org/10.1016/j.lithos.2013.09.008.

González-Jiménez, J.M., Locmelis, M., Belousova, E., Griffin, W.L., Gervilla, F., Kerestedjian, T.N., O'Reilly, S.Y., Pearson, N.J., Sergeeva, I., 2015a. Genesis and tectonic implications of podiform chromitites in the metamorphosed ultramafic massif of Dobromirtsi (Bulgaria). Gondw. Res. 27, 555–574. https://doi.org/10.1016/j.gr.2013.09.020.

González-Jiménez, J.M., Reich, M., Camprubí, A., Gervilla, F., Griffin, W.L., Colás, V., O'Reilly, S.Y., Proenza, J.A., Pearson, N.J., Centeno-García, E., 2015b. Thermal metamorphism of mantle chromites and the stability of noble-metal nanoparticles. Contrib. Miner. Petrol. 170, 15. https://doi.org/10.1007/s00410-015-1169-9.

González-Jiménez, J.M., Proenza, J.A., Martini, M., Camprubí, A., Griffin, W.L., O'Reilly, S.Y., Pearson, N.J., 2017b. Deposits associated with ultramafic–mafic complexes in Mexico: the Loma Baya case. Ore Geol. Rev. 81, 1053–1065. https://doi.org/10.1016/j.oregeorev.2015.05.014.

González-Jiménez, J.M., Proenza, J.A., Pastor-Oliete, M., Saunders, E., Aiglsperger, T., Pujol-Solà, N., Melgarejo, J.C., Gervilla, F., Garcia-Casco, A., 2020. Precious metals in magmatic Fe-Ni-Cu sulfides from the Potosí chromitite deposit, eastern Cuba. Ore Geol. Rev. 118, 103339 https://doi.org/10.1016/j.oregeorev.2020.103339.

González-Jiménez, J.M., Reich, M., 2017. An overview of the platinum-group element nanoparticles in mantle-hosted chromite deposits. Ore Geol. Rev. 81, 1236–1248. https://doi.org/10.1016/j.oregeorev.2016.06.022.

Helmy, H.M., Ballhaus, C., Fonseca, R.O.C., Wirth, R., Nagel, T., Tredoux, M., 2013. Noble metal nanoclusters and nanoparticles precede mineral formation in magmatic sulphide melts. Nat. Commun. 4, 2405. https://doi.org/10.1038/ncomms3405.

Hernández-González, J.S., Butjosa, L., Pujol-Solà, N., Aiglsperger, T., Weber, M., Escayola, M., Ramírez-Cárdenas, C., Blanco-Quintero, I.F., González-Jiménez, J.M., Proenza, J.A., 2020. Petrology and geochemistry of high-Al chromitites from the MedellÍn Metaharzburgitic Unit (MMU), Colombia. BSGM 72, A120620.

Hickey, R.L., Frey, F.A., 1982. Geochemical characteristics of boninite series volcanics: implications for their source. Geochim. Cosmochim. Acta 46, 2099–2115. https://doi.org/10.1016/0016-7037(82)90188-0.

Hiessleitner, G., 1953. Der magmatische Schichtbau des Kraubather chromerzführenden Peridotitmassivs. Fortschritte Mineralogie 32, 75–78.

Holwell, D.A., McDonald, I., 2010. A Review of the Behaviour of Platinum Group Elements within Natural Magmatic Sulfide Ore Systems. Platin. Met. Rev. 54, 26–36. https://doi.org/10.1595/147106709X480913.

Hu, W.-J., Zhou, M.-F., Yudovskaya, M.A., Vikentyev, I.V., Malpas, J., Zhang, P.-F., 2022. Trace Elements in Chromite as Indicators of the Origin of the Giant Podiform Chromite Deposit at Kempirsai, Kazakhstan. Econ. Geol. 117, 1629–1655. https://doi.org/10.5382/econgeo.4955.

Jiménez-Franco, A., González-Jiménez, J.M., Roqué, J., Proenza, J.A., Gervilla, F., Nieto, F., 2020. Nanoscale constraints on the in situ transformation of Ru–Os–Ir sulfides to alloys at low temperature. Ore Geol. Rev. 124, 103640 https://doi.org/10.1016/j.oregeorev.2020.103640.

Kamenetsky, V.S., Crawford, A.J., Meffre, S., 2001. Factors Controlling Chemistry of Magmatic Spinel: an Empirical Study of Associated Olivine, Cr-spinel and Melt Inclusions from Primitive Rocks. J Petrology 42, 655–671. https://doi.org/10.1093/petrology/42.4.655.

Kryza, R., Pin, C., 2010. The Central-Sudetic ophiolites (SW Poland): Petrogenetic issues, geochronology and palaeotectonic implications. Gondw. Res. 17, 292–305. https://doi.org/10.1016/j.gr.2009.11.001.

Leblanc, M., 1991. Platinum-group elements and gold in ophiolitic complexes: distribution and fractionation from mantle to oceanic floor. In: Ophiolite Genesis and Evolution of the Oceanic Lithosphere. Springer, pp. 231–260.

Lefort, J.-P., 1989. Basement Correlation Across the North Atlantic. Springer Berlin Heidelberg, Berlin, Heidelberg. Doi: 10.1007/978-3-642-73350-5.

Li, C., Barnes, S.-J., Makovicky, E., Rose-Hansen, J., Makovicky, M., 1996. Partitioning of nickel, copper, iridium, rhenium, platinum, and palladium between monosulfide solid solution and sulfide liquid: Effects of composition and temperature. Geochim. Cosmochim. Acta 60, 1231–1238. https://doi.org/10.1016/0016-7037(96)00009-9.

Li, C., Ripley, E.M., 2006. Formation of Pt–Fe alloy by desulfurization of Pt–Pd sulfide in the J-M reef of the Stillwater complex, Montana. Can. Mineral. 44, 895–903.

Liang, Q.-L., Song, X.-Y., Wirth, R., Chen, L.-M., Dai, Z.-H., 2019. Implications of nano- and micrometer-size platinum-group element minerals in base metal sulfides of the Yangliuping Ni-Cu-PGE sulfide deposit, SW China. Chem. Geol. 517, 7–21. https://doi.org/10.1016/j.chemgeo.2019.04.015.

Maier, W.D., Rasmussen, B., Fletcher, I.R., Godel, B., Barnes, S.J., Fisher, L.A., Yang, S.H., Huhma, H., Lahaye, Y., 2015. Petrogenesis of the ~2·77 Ga Monts de Cristal Complex, Gabon: Evidence for Direct Precipitation of Pt-arsenides from Basaltic Magma. J. Petrology 56, 1285–1308. https://doi.org/10.1093/petrology/egv035.

Majzlan, J., Makovicky, M., Makovicky, E., Rose-Hansen, J., 2002. The system Fe Pt S at 1100 oC. Can. Mineral. 40, 509–517. https://doi.org/10.2113/gscanmin.40.2.509.

Makovicky, E., Karup-Møller, S., 2000. Phase relations in the metal-rich portions of the phase system Pt-Ir-Fe-S at 1000°C and 1100°C. Mineral. Mag. 64, 1047–1056. https://doi.org/10.1180/002646100550047.

Malitch, K.N., Melcher, F., Mühlhans, H., 2001. Palladium and gold mineralization in podiform chromitite at Kraubath, Austria. Mineral. Petrol. 73, 247–277. https://doi.org/10.1007/s007100170002.

Malitch, K.N., Junk, S.A., Thalhammer, O.A.R., Melcher, F., Knauf, V.V., Pernicka, E., Stumpfl, E.F., 2003. Laurite and ruarsite from podiform chromitites at Kraubath and Hochgrössen, Austria: New insights from osmium isotopes. Can. Mineral. 41, 331–352. https://doi.org/10.2113/gscanmin.41.2.331.

Marcos, A., Farias, P., Galán, G., Fernández, F.J., Llana-Fúnez, S., 2002. Tectonic framework of the Cabo Ortegal Complex: A slab of lower crust exhumed in the Variscan orogen (northwestern Iberian Peninsula), in: Variscan-Appalachian Dynamics: The Building of the Late Paleozoic Basement. Geol. Soc. Am. Doi: 10.1130/0-8137-2364-7.143.

Marcos, A., Marquínez, J., Pérez-Estaún, A., Pulgar, J.A., Bastida, F., 1984. Nuevas aportaciones al conocimiento de la evolución tectonometamórfica del Complejo de Cabo Ortegal (NW de España). Cuadernos Del Laboratorio Xeolóxico De Laxe 7, 125–137.

Martínez Catalán, J.R., 2011. Are the oroclines of the Variscan belt related to late Variscan strike-slip tectonics? Terra Nova 23, 241–247. https://doi.org/10.1111/j.1365-3121.2011.01005.x.

Martínez Catalán, J.R., Arenas, R., Díaz García, F., González Cuadra, P., Gómez-Barreiro, J., Abati, J., Castiñeiras, P., Fernández-Suárez, J., Sánchez Martínez, S., Andonaegui, P., González Clavijo, E., Díez Montes, A., Rubio Pascual, F.J., Valle Aguado, B., 2007. Space and time in the tectonic evolution of the northwestern Iberian Massif: Implications for the Variscan belt, in: Geological Society of America Memoirs. Geological Society of America, pp. 403–423. Doi: 10.1130/2007.1200(21).

Martínez Catalán, J.R., Gómez Barreiro, J., Dias da Silva, Í., Chichorro, M., López-Carmona, A., Castiñeiras, P., Abati, J., Andonaegui, P., Fernández-Suárez, J., González Cuadra, P., Benítez-Pérez, J.M., 2019. Variscan Suture Zone and Suspect Terranes in the NW Iberian Massif: Allochthonous Complexes of the Galicia-Trás os Montes Zone (NW Iberia). In: Quesada, C., Oliveira, J.T. (Eds.), The Geology of Iberia: A Geodynamic Approach, Regional Geology Reviews. Springer International Publishing, Cham, pp. 99–130. https://doi.org/10.1007/978-3-030-10519-8_4.

Martínez Catalán, J.R., Schulmann, K., Ghienne, J.-F., 2021. The Mid-Variscan Allochthon: Keys from correlation, partial retrodeformation and plate-tectonic reconstruction to unlock the geometry of a non-cylindrical belt. Earth Sci. Rev. 220, 103700 https://doi.org/10.1016/j.earscirev.2021.103700.

Mateus, A., Munhá, J., Ribeiro, A., Tassinari, C.C.G., Sato, K., Pereira, E., Santos, J.F., 2016. U-Pb SHRIMP zircon dating of high-grade rocks from the Upper Allochthonous Terrane of Bragança and Morais Massifs (NE Portugal); geodynamic consequences. Tectonophysics 675, 23–49. https://doi.org/10.1016/j.tecto.2016.02.048.

Maurel, C., 1984. Étude expérimentale de l'équilibre spinelle chromifère–liquide silicaté basique. Soc Fr Minéral Cristallogr, Congrès "Les Spinelles"(Lille).

McDonald, A.M., Cabri, L.J., 2023. Discreditation of Platarsite: A S-Rich Variety of Sperrylite. Canad. J. Mineral. Petrol. 61, 1039–1044. https://doi.org/10.3749/2300021.

McDonough, W.F., Sun, S.S., 1995. The composition of the Earth. Chem. Geol. 120, 223–253. https://doi.org/10.1016/0009-2541(94)00140-4.

Melcher, F., Meisel, T., 2004. A Metamorphosed Early Cambrian Crust-Mantle Transition in the Eastern Alps, Austria. J. Petrol. 45, 1689–1723. https://doi.org/10.1093/petrology/egh030.

Merinero, R., Lunar, R., Ortega, L., Piña, R., Monterrubio, S., Gervilla, F., 2013. Hydrothermal palladium enrichment in podiform chromitites of Calzadilla de los Barros (SW Iberian Peninsula). Can. Mineral. 51, 387–404. https://doi.org/10.3749/canmin.51.3.387.

Merinero, R., Lunar, R., Ortega, L., Piña, R., Monterrubio, S., Gervilla, F., 2014. Zoned chromite records multiple metamorphic episodes in the Calzadilla de los Barros ultramafic bodies (SW Iberian peninsula). Ejm 26, 757–770. https://doi.org/10.1127/ejm/2014/0026-2406.

Moreno, T., Prichard, H.M., Lunar, R., Monterrubio, S., Fisher, P., 1999. Formation of a secondary platinum-group mineral assemblage in chromitites from the Herbeira ultramafic massif in Cabo Ortegal, NW Spain. Eur. J. Mineral. 11, 363–378.

Moreno, T., Gibbons, W., Prichard, H.M., Lunar, R., 2001. Platiniferous chromitite and the tectonic setting of ultramafic rocks in Cabo Ortegal, NW Spain. J. Geol. Soc. London 158, 601–614. https://doi.org/10.1144/jgs.158.4.601.

Naldrett, A.J., Duke, J.M., 1980. Platinum metals magmatic sulfide ores. Science 208, 1417–1424.

Naldrett, A.J., Wilson, A., Kinnaird, J., Yudovskaya, M., Chunnett, G., 2012. The origin of chromitites and related PGE mineralization in the Bushveld Complex: new mineralogical and petrological constraints. Miner. Deposita 47, 209–232.

Neuman, R.B., Max, M.D., 1989. Penobscottian-Grampian-finnmarkian orogenies as indicators of terrane linkages. Special Paper of the Geol. Soc. Am. https://doi.org/10.1130/SPE230-p31.

Novo-Fernández, I., Garcia-Casco, A., Arenas, R., Díez Fernández, R., 2016. The metahyaloclastic matrix of a unique metavolcanic block reveals subduction in the Somozas Mélange (Cabo Ortegal Complex, NW Iberia): tectonic implications for the assembly of Pangea. J. Metam. Geol. 34, 963–985. https://doi.org/10.1111/jmg.12216.

Novo-Fernández, I., Arenas, R., Díez Fernández, R., Garcia-Casco, A., 2022. A complex accretionary assembly of Pangea developed in the range c. 400–340 Ma: the four successive events of high-P/ultra-high-P metamorphism of the Variscan Orogen. Int. Geol. Rev. 1–14. https://doi.org/10.1080/00206814.2022.2127126.

O'Driscoll, B., González-Jiménez, J.M., 2016. Petrogenesis of the Platinum-Group Minerals. Rev. Mineral. Geochem. 81, 489–578. https://doi.org/10.2138/rmg.2016.81.09.

Ordóñez Casado, B., Gebauer, D., Schäfer, H.J., Gil Ibarguchi, J.I., Peucat, J.J., 2001. A single Devonian subduction event for the HP/HT metamorphism of the Cabo

Ortegal complex within the Iberian Massif. Tectonophysics 332, 359–385. https://doi.org/10.1016/S0040-1951(00)00210-9.

Pagé, P., Barnes, S.-J., 2009. Using trace elements in chromites to constrain the origin of podiform chromitites in the Thetford Mines ophiolite, Québec, Canada. Econ. Geol. 104, 997–1018.

Peucat, J.J., Bernard-Griffiths, J., Gil Ibarguchi, J.I., Dallmeyer, R.D., Menot, R.P., Cornichet, J., Leon, I.P.D., M., 1990. Geochemical and geochronological cross section of the deep Variscan crust: The Cabo Ortegal high-pressure nappe (northwestern Spain). Tectonophysics 177, 263–292. https://doi.org/10.1016/0040-1951(90)90285-G.

Plissart, G., Monnier, C., Diot, H., Mărunţiu, M., Berger, J., Triantafyllou, A., 2017. Petrology, geochemistry and Sm-Nd analyses on the Balkan-Carpathian Ophiolite (BCO – Romania, Serbia, Bulgaria): Remnants of a Devonian back-arc basin in the easternmost part of the Variscan domain. J. Geodyn. 105, 27–50. https://doi.org/10.1016/j.jog.2017.01.001.

Prichard, H.M., Neary, C.R., Fisher, P.C., O'hara, M.J., 2008. PGE-rich podiform chromitites in the Al 'Ays ophiolite complex, Saudi Arabia: an example of critical mantle melting to extract and concentrate PGE. Econ. Geol. 103, 1507–1529.

Proenza, J.A., Ortega-Gutiérrez, F., Camprubí, A., Tritlla, J., Elías-Herrera, M., Reyes-Salas, M., 2004. Paleozoic serpentinite-enclosed chromitites from Tehuitzingo (Acatlán Complex, southern Mexico): a petrological and mineralogical study. J. S. Am. Earth Sci. 16, 649–666. https://doi.org/10.1016/j.jsames.2003.12.003.

Proenza, J.A., Zaccarini, F., Lewis, J.F., Longo, F., Garuti, G., 2007. Chromian spinel composition and the platinum-group minerals of the PGE-rich Loma Peguera chromitites, Loma Caribe peridotite, Dominican Republic. Can. Mineral. 45, 631–648.

Puelles, P., Gil Ibarguchi, J.I., Beranoaguirre, A., Ábalos, B., 2012. Mantle wedge deformation recorded by high-temperature peridotite fabric superposition and hydrous retrogression (Limo massif, Cabo Ortegal, NW Spain). Int J Earth Sci (geol Rundsch) 101, 1835–1853. https://doi.org/10.1007/s00531-012-0761-8.

Pujol-Solà, N., Domínguez-Carretero, D., Proenza, J.A., Haissen, F., Ikenne, M., González-Jiménez, J.M., Colás, V., Maacha, L., Garcia-Casco, A., 2021. The chromitites of the Neoproterozoic Bou Azzer ophiolite (central Anti-Atlas, Morocco) revisited. Ore Geol. Rev. 134, 104166 https://doi.org/10.1016/j.oregeorev.2021.104166.

Purvis, A.C., Nesbitt, R.W., Hallberg, J.A., 1972. The Geology of Part of the Carr Boyd Rocks Complex and Its Associated Nickel Mineralization, Western Australia. Econ. Geol. 67, 1093–1113. https://doi.org/10.2113/gsecongeo.67.8.1093.

Reagan, M.K., Ishizuka, O., Stern, R.J., Kelley, K.A., Ohara, Y., Blichert-Toft, J., Bloomer, S.H., Cash, J., Fryer, P., Hanan, B.B., Hickey-Vargas, R., Ishii, T., Kimura, J.-I., Peate, D.W., Rowe, M.C., Woods, J., 2010. Fore-arc basalts and subduction initiation in the Izu-Bonin-Mariana system: Fore-arc basalts and subduction initiation. Geochem. Geophys. Geosyst. 11 https://doi.org/10.1029/2009GC002871.

Rollinson, H., 2008. The geochemistry of mantle chromitites from the northern part of the Oman ophiolite: inferred parental melt compositions. Contrib. Miner. Petrol. 156, 273–288.

Rollinson, H., Adetunji, J., 2013. Mantle podiform chromitites do not form beneath mid-ocean ridges: A case study from the Moho transition zone of the Oman ophiolite. Lithos 177, 314–327. https://doi.org/10.1016/j.lithos.2013.07.004.

Sánchez Martínez, S., Arenas, R., Gerdes, A., Castiñeiras, P., Potrel, A., Fernández-Suárez, J., 2011. Isotope geochemistry and revised geochronology of the Purrido Ophiolite (Cabo Ortegal Complex, NW Iberian Massif): Devonian magmatism with mixed sources and involved Mesoproterozoic basement. JGS 168, 733–750. https://doi.org/10.1144/0016-76492010-065.

Sánchez Martínez, S., Arenas, R., Andonaegui, P., Martínez Catalán, J.R., Pearce, J.A., 2007. Geochemistry of two associated ophiolites from the Cabo Ortegal Complex (Variscan belt of NW Spain), in: Geological Society of America Memoirs. Geol. Soc. Am., pp. 445–467. Doi: 10.1130/2007.1200(23).

Santos Zalduegui, J.F., Schärer, U., Gil Ibarguchi, J.I., Girardeau, J., 1996. Origin and evolution of the Paleozoic Cabo Ortegal ultramafic-mafic complex (NW Spain): U-Pb, Rb-Sr and Pb-Pb isotope data. Chem. Geol. 129, 281–304. https://doi.org/10.1016/0009-2541(95)00144-1.

Santos Zalduegui, J.F., Schärer, U., Gil Ibarguchi, J.I., Girardeau, J., 2002. Genesis of Pyroxenite-rich Peridotite at Cabo Ortegal (NW Spain): Geochemical and Pb–Sr–Nd Isotope Data. J. Petrol. 43, 17–43. https://doi.org/10.1093/petrology/43.1.17.

Shervais, J.W., Reagan, M., Haugen, E., Almeev, R.R., Pearce, J.A., Prytulak, J., Ryan, J.G., Whattam, S.A., Godard, M., Chapman, T., Li, H., Kurz, W., Nelson, W.R., Heaton, D., Kirchenbaur, M., Shimizu, K., Sakuyama, T., Li, Y., Vetter, S.K., 2019. Magmatic Response to Subduction Initiation: Part 1. Fore-arc Basalts of the Izu-Bonin Arc From IODP Expedition 352. Geochem. Geophys. Geosyst. 20, 314–338. https://doi.org/10.1029/2018GC007731.

Shervais, J.W., Reagan, M.K., Godard, M., Prytulak, J., Ryan, J.G., Pearce, J.A., Almeev, R.R., Li, H., Haugen, E., Chapman, T., Kurz, W., Nelson, W.R., Heaton, D.E., Kirchenbaur, M., Shimizu, K., Sakuyama, T., Vetter, S.K., Li, Y., Whattam, S., 2021. Magmatic Response to Subduction Initiation, Part II: Boninites and Related Rocks of the Izu-Bonin Arc From IODP Expedition 352. Geochem. Geophys. Geosyst. 22 https://doi.org/10.1029/2020GC009093 e2020GC009093.

Stern, R.J., Reagan, M., Ishizuka, O., Ohara, Y., Whattam, S., 2012. To understand subduction initiation, study forearc crust: To understand forearc crust, study ophiolites. Lithosphere 4, 469–483. https://doi.org/10.1130/L183.1.

Thalhammer, O.A.R., Prochaska, W., Mühlhans, H., 1990. Solid inclusions in chrome-spinels and platinum group element concentrations from the Hochgrössen and Kraubath ultramafic massifs (Austria): Their relationships to metamorphism and serpentinization. Contr. Mineral. Petrol. 105, 66–80. https://doi.org/10.1007/BF00320967.

Tilhac, R., Ceuleneer, G., Griffin, W.L., O'Reilly, S.Y., Pearson, N.J., Benoit, M., Henry, H., Girardeau, J., Grégoire, M., 2016. Primitive Arc Magmatism and Delamination: Petrology and Geochemistry of Pyroxenites from the Cabo Ortegal Complex. Spain. J. Petrology 57, 1921–1954. https://doi.org/10.1093/petrology/egw064.

Tilhac, R., Grégoire, M., O'Reilly, S.Y., Griffin, W.L., Henry, H., Ceuleneer, G., 2017. Sources and timing of pyroxenite formation in the sub-arc mantle: Case study of the Cabo Ortegal Complex, Spain. Earth Planet. Sci. Lett. 474, 490–502. https://doi.org/10.1016/j.epsl.2017.07.017.

Tilhac, R., Oliveira, B., Griffin, W.L., O'Reilly, S.Y., Schaefer, B.F., Alard, O., Ceuleneer, G., Afonso, J.C., Grégoire, M., 2020. Reworking of old continental lithosphere: Unradiogenic Os and decoupled Hf Nd isotopes in sub-arc mantle pyroxenites. Lithos 354–355, 105346. https://doi.org/10.1016/j.lithos.2019.105346.

Van Calsteren, P.W.C., Boelrijk, N.A.I.M., Hebeda, E.H., Priem, H.N.A., Den Tex, E., Verdurmen, E.A.T., Verschure, R.H., 1979. Isotopic dating of older elements (including the Cabo Ortegal mafic-ultramafic complex) in the Hercynian orogen of NW Spain: Manifestations of a presumed Early Paleozoic mantle-plume. Chem. Geol. 24, 35–56. https://doi.org/10.1016/0009-2541(79)90011-1.

Verryn, S.M.C., Merkle, R.K.W., 2000. Synthetic "Cooperite", "Braggite", and "Vysotskite" in the system PtS-PdS-NiS at 1100°C, 1000°C, and 900°C. Mineral. Petrol. 68, 63–73. https://doi.org/10.1007/s007100050003.

Vogel, D.E., 1967. Petrology of an eclogite- and pyrigarnite-bearing polymetamorphic rock complex at Cabo Ortegal, NW Spain. Leidse. Geol. Meded. 40, 121–213.

Vymazalova, A., Laufek, F., Drabek, M., Stanley, C.J., Baker, R.J., Bermejo, R., Garuti, G., Thalhammer, O., Proenza, J.A., Longo, F., 2012. Zaccariniite, RhNiAs, a new platinum-group mineral from Loma Peguera, Dominican Republic. Can. Mineral. 50, 1321–1329. https://doi.org/10.3749/canmin.50.5.1321.

Wilson, M. (Ed.), 1989. Igneous Petrogenesis. Springer, Netherlands, Dordrecht. https://doi.org/10.1007/978-1-4020-6788-4.

Wojtulek, P.M., Puziewicz, J., Ntaflos, T., Bukała, M., 2016. Podiform chromitites from the Variscan ophiolite serpentinites of Lower Silesia (SW Poland) - petrologic and tectonic setting implications. GQ. https://doi.org/10.7306/gq.1238.

Wojtulek, P.M., Schulz, B., Delura, K., Dajek, M., 2019. Formation of chromitites and ferrogabbros in ultramafic and mafic members of the Variscan Ślęża ophiolite (SW Poland). Ore Geol. Rev. 106, 97–112. https://doi.org/10.1016/j.oregeorev.2019.01.021.

Wood, S.A., Mountain, B.W., Pan, P., 1992. The aqueous geochemistry of platinum, palladium and gold; recent experimental constraints and a re-evaluation of theoretical predictions. Can. Mineral. 30, 955–982.

Zaccarini, F., Garuti, G., Proenza, J.A., Campos, L., Thalhammer, O.A., Aiglsperger, T., Lewis, J.F., 2011. Chromite and platinum group elements mineralization in the Santa Elena Ultramafic Nappe (Costa Rica): geodynamic implications. Geol. Acta Int. Earth Sci. J. 9, 407–423.

Zhou, M.-F., Robinson, P.T., Su, B.-X., Gao, J.-F., Li, J.-W., Yang, J.-S., Malpas, J., 2014. Compositions of chromite, associated minerals, and parental magmas of podiform chromite deposits: The role of slab contamination of asthenospheric melts in suprasubduction zone environments. Gondw. Res. 26, 262–283. https://doi.org/10.1016/j.gr.2013.12.011.

Zhu, Q., Zhu, Y., 2020. Chromitite genesis based on chrome-spinels and their inclusions in the Sartohay podiform chromitites in west Junggar of northwest China. Ore Geol. Rev. 119, 103401 https://doi.org/10.1016/j.oregeorev.2020.103401.